

## ABSTRACT

MOODY, BAXTER FINLEY. Strained Layer Superlattice Solar Cells. (Under the direction of Dr. Nadia El-Masry and Dr. Salah Bedair.)

For several years, photovoltaic researchers have searched for a material to extend solar cell absorption to wavelengths beyond the GaAs cut-off to increase efficiency of multi-junction solar cells. The best record efficiency of any solar cell is currently ~40% for a 3-Junction GaInP/GaAs/Ge cell at high solar concentration manufactured by Spectro-Lab. Higher efficiency can be realized with a 3-Junction GaInP/GaAs/1eV or 4-Junction GaInP/GaAs/1eV/Ge configuration if a high quality, lattice matched 1eV material can be found. The best material candidate for several years has been InGaAsN due to a very large bandgap reduction with small N concentrations, but quality and performance remains low despite considerable effort by many researchers to improve the material to adequate device quality. In particular, the carrier diffusion lengths are greatly reduced compared to GaAs due to poorly understood defects. For very low N compositions, below ~1%, device quality is maintained.

Here a novel solution is proposed to develop a high quality material that is both lattice matched to GaAs and has a bandgap around 1eV. By inserting a strain-layer-superlattice of  $\text{In}_{0.28}\text{Ga}_{0.72}\text{As}/\text{GaAs}_{0.25}\text{P}_{0.75}$  into the i-region of a GaAs p-i-n diode, effective bandgaps near 1eV have been demonstrated. Bandgap reduction is realized by increasing In composition in the well layer. Compressively strained InGaAs well layers are grown below the critical layer thickness to prevent formation of misfit dislocations. Strain is balanced via

subsequent growth of a tensile strained GaAsP layer, which is also below the critical layer thickness. This structure is then repeated for several periods to build up total InGaAs thickness for increased photon absorption. Thin GaAsP barriers are required for effective carrier collection which imposes a high P composition for strain balance. Cells with thick barriers exhibited low currents, indicating that carrier tunneling is critical for proper device performance. Solar cells demonstrated in this research effort are at least equal in performance to initial InGaAsN based cells and show potential for efficient operation.

# **Strained Layer Superlattice Solar Cells**

by

**BAXTER FINLEY MOODY**

A dissertation submitted to the Graduate Faculty of  
North Carolina State University  
in partial fulfillment of the  
requirements for the Degree of  
Doctor of Philosophy

**MATERIALS SCIENCE AND ENGINEERING**

Raleigh, NC

2006

**APPROVED BY:**

---

---

---

Chair of Advisory Committee

---

Co-chair of Advisory Committee

## **BIOGRAPHY**

Baxter Moody was born in the small town of Boone, located in the mountains of North Carolina. Several years later he decided to pursue higher education at North Carolina State University which resulted in a Bachelor of Science degree in Mechanical Engineering. During this undergraduate experience, a temporary departure from academia was taken to gain experience in the semiconductor industry. This led to a Master of Materials Science and Engineering degree and ultimately to the pursuit of a Doctorate of Philosophy in Materials Science.

## **ACKNOWLEDGEMENTS**

Many thanks to the members of our research group both past and present: Mike Aumer, Steven LeBoeuf, Gregg McIntosh, John Roberts, Mason Reed, Meredith Reed, Chris Parker, Phil Barletta, Acar Berkman, Erdem Arkun, and Oliver Luen. I am also obliged to several others within the university community for technical discussions, borrowing equipment, and camaraderie: Andy (The Face) Oberhoffer, Brian Laughlin, Scott Dillon, Rob Trussell, Dr. Jon-Paul Maria and his research group, and Edna Deas for always having the correct administrative solution. The love and support of my family through this endeavor and all aspects of life is invaluable. I would like to thank my committee members Dr. Abdel Fahmy and Dr. Jerry Cuomo. Finally, a special thanks to Dr. Nadia El-Masry and Dr. Salah Bedair for many discussions, mentoring, and financial support.

# CONTENTS

<b>LIST OF TABLES.....</b>	<b>vi</b>
<b>LIST OF FIGURES.....</b>	<b>vii</b>
<b>1 INTRODUCTION .....</b>	<b>1</b>
1.1 World Energy Overview .....	1
1.2 Current and Future Role of Photovoltaic Technology.....	4
<b>2 PHOTOVOLTAIC BASICS .....</b>	<b>8</b>
2.1 Solar Irradiance.....	8
2.2 Semiconductor Materials Properties.....	10
2.2.1 Crystal Structure.....	10
2.2.2 Energy Bands in Semiconductors.....	13
2.2.3 Electrons and Holes.....	17
2.2.4 Junctions.....	22
2.3 Device Principles.....	23
2.3.1 Photocurrent, Dark Current, and Photovoltage.....	23
2.3.2 Fill Factor and Efficiency.....	26
2.3.3 Cell Design Considerations.....	29
<b>3 MULTI-JUNCTION SOLAR CELLS .....</b>	<b>32</b>
3.1 Lattice Matching.....	33
3.2 Materials for Multijunction Photovoltaics.....	36
3.2.1 Candidate PV Semiconductors for High Efficiency.....	36
3.2.2 Survey of Developed PV Materials Systems.....	39
3.2.3 Pursuit of a 1eV Lattice Matched PV Junction.....	42
<b>4 PROPOSED NOVEL THIRD JUNCTION .....</b>	<b>45</b>
4.1 Strained Layer Superlattices.....	45
4.2 Survey of InGaAs/GaAsP Structures for Photovoltaics.....	48
4.3 Analysis of InGaAs/GaAsP SLS for PV Applications.....	48
4.3.1 Bandgap Dependence on Strain, Temperature, and Composition.....	49
4.3.2 Critical Layer Thickness for InGaAs and GaAsP.....	54
4.3.3 Quantum Size Effect.....	57
4.3.4 p-i-n Device.....	62
<b>5 OMVPE GROWTH.....</b>	<b>70</b>
5.1 Organometallic Precursors.....	71
5.2 OMVPE Growth Equipment.....	72
5.2.1 Precursor Sources and Delivery.....	73
5.2.2 Reactor.....	77
5.2.3 Exhaust System and Scrubber.....	82
5.2.4 Equipment Cleanliness and Film Purity.....	85
5.3 Growth Conditions and Procedures.....	88
5.3.1 GaAs Substrates.....	89
5.3.2 Reactor Loading and Routine Maintenance.....	90

5.3.3	Film Growth Details.....	91
<b>6</b>	<b>CHARACTERIZATION .....</b>	<b>97</b>
6.1	Optical Microscopy .....	97
6.2	X-Ray Diffraction.....	101
6.3	Photoluminescence .....	106
6.4	Hall Effect.....	108
6.5	Current-Voltage and Spectral Response.....	109
6.6	Transmission Electron Microscopy.....	111
<b>7</b>	<b>DEVICE PROCESSING .....</b>	<b>113</b>
7.1	Photolithography.....	114
7.2	Metallization and Liftoff.....	116
7.3	Etching.....	117
7.4	Annealing.....	118
<b>8</b>	<b>GAASN .....</b>	<b>119</b>
<b>9</b>	<b>STRAINED LAYER SUPERLATTICE SOLAR CELLS .....</b>	<b>125</b>
9.1	Development of the InGaAs/GaAsP SLS.....	125
9.2	Device Performance.....	133
9.2.1	Light and Dark Current .....	135
9.2.2	Spectral Response.....	139
9.2.3	Carrier Transport .....	141
<b>10</b>	<b>CONCLUSION .....</b>	<b>149</b>
	<b>REFERENCES .....</b>	<b>151</b>
	<b>APPENDIX .....</b>	<b>165</b>
	<b>APPENDIX A.....</b>	<b>166</b>
	<b>APPENDIX B.....</b>	<b>168</b>

## LIST OF TABLES

<b>Table 1.1</b> Available Primary Energy Sources .....	2
<b>Table 2.1</b> Selected Semiconductor Parameters .....	21
<b>Table 4.1</b> Parameters for Electric Field Calculation .....	65
<b>Table 5.1</b> List of Precursors .....	92
<b>Table 5.2</b> Bulk Film Growth Parameters .....	93
<b>Table 5.3</b> Quantum Well Growth Parameters .....	94
<b>Table 9.1</b> Performance Parameters for Test Cells Under AM1.5D Illumination .....	138
<b>Table 9.2</b> Calculated Thermionic Emission & Tunneling Lifetimes(Samples B&D[ps])..	146
<b>Table 10.1</b> Comparison of Early InGaAsN Solar Cell Compared to InGaAs/GaAsP Cell	150

## LIST OF FIGURES

<b>Figure 1.1</b> Record Cell Efficiencies.....	6
<b>Figure 2.1</b> Standard AM0 and AM1.5 Direct Spectra .....	10
<b>Figure 2.2</b> Face Centered Cubic Unit Cell.....	11
Figure 2.3 Zinc Blende Structure.....	12
<b>Figure 2.4</b> Energy Band Formation as Atoms are Brought Together to Form Solids .....	14
<b>Figure 2.5</b> Energy Band Structure of Si and GaAs (After Chelikowski <sup>38</sup> and Cerdá <sup>39</sup> ) Arrows Indicate Indirect Transition in Si and Direct Transition in GaAs.....	16
<b>Figure 2.6</b> Simplified Diagram of Valence and Conduction Bands, Bandgap, and Electron and Hole Behavior at Absolute Zero and Finite Temperatures .....	18
<b>Figure 2.7</b> Photogeneration of Carriers.....	19
<b>Figure 2.8</b> Acceptor dopants enhance conduction in p-type semiconductors via creating holes in the valence band. Donor dopants enhance conduction in n-type semiconductors via promoting electrons to the conduction band.....	20
<b>Figure 2.9</b> p-n Junction Formation and Resulting Band Structure .....	23
<b>Figure 2.10</b> Diode Characteristic I-V Curve.....	24
<b>Figure 2.11</b> Maximum Power Rectangle or Fill Factor .....	26
<b>Figure 2.12</b> Equivalent Circuit & Parasitic Resistances .....	27
<b>Figure 2.13</b> Limiting Efficiency for Single Junction Solar Cell. Verified Record Efficiency for GaAs and Si Indicated in Red .....	29
<b>Figure 2.14</b> Typical Solar Cell Design .....	31
<b>Figure 3.1</b> Lattice Mismatch Strain Relaxation via Formation of Dislocations .....	34
<b>Figure 3.2</b> Critical Layer Thickness as Predicted by Matthews-Blakeslee and People-Bean .....	35
<b>Figure 3.3</b> AM1.5D 2-J Cell Thermodynamic Limiting Efficiency Contours (Maximum at 1.56eV and 0.93 eV).....	37
<b>Figure 3.4</b> Bandgap vs. Lattice Constant for Some Photovoltaic Semiconductors .....	38
<b>Figure 3.5</b> AM1.5D 3J Top and Bottom Cell Efficiency Contours with GaAs Middle Cell	40

<b>Figure 3.6</b> AM1.5D Efficiency Contours for 4J Top/GaAs/3rd/Ge Cell.....	41
<b>Figure 4.1</b> Strained Layer Superlattice with Resulting Band Diagram .....	47
<b>Figure 4.2</b> Band Structure of GaAs under (A) Biaxial Compressive Strain, (B) Zero Strain, and (C) Biaxial Tensile Strain (CB=conduction band, HH=heavy hole band, LH=light hole band, SO=split-off band)(After Asai <sup>130</sup> and Bir <sup>129</sup> ).....	50
<b>Figure 4.3</b> Compressive Strain Induced Light(Blue) and Heavy(Red) Hole Band Shift Compared with Unstrained InGaAs Bandgap Dependence(Green) on In Fraction (300K). Combined Effective Bandgap Shift is also Plotted in Black.....	52
<b>Figure 4.4</b> Tensile Strain Induced Light(Light Blue) and Heavy(Red) Hole Band Shift Compared with Unstrained GaAsP Bandgap Dependence(X-Green, $\Gamma$ -Dark Blue) on P Fraction (300K). Combined Effective Bandgap is Plotted in Black.....	53
<b>Figure 4.5</b> Critical Layer Thickness Indium Fraction Dependence for InGaAs Strained to GaAs (After Matthews-Blakeslee).....	55
<b>Figure 4.6</b> Critical Layer Thickness Phosphorous Fraction Dependence for GaAsP Strained to GaAs (After Matthews-Blakeslee) .....	56
<b>Figure 4.7</b> Band Structure of an $\text{In}_{0.15}\text{Ga}_{0.85}\text{As}/\text{GaAs}_{0.7}\text{P}_{0.3}$ SLS Demonstrating Quantum Size Effect (Well and Barriers Layers are 100Å).....	58
<b>Figure 4.8</b> Graphical Solution of the Schrödinger Equation to Find Quantized Energy States in the InGaAs Quantum Well (Each zero represents a discrete energy level formed in the well in the valence band (Blue) and conduction band (Red)).....	60
<b>Figure 4.9</b> Combined Effective $\text{In}_{0.3}\text{Ga}_{0.7}\text{As}$ Bandgap (Green) for a Range of Well Widths, Unstrained (Blue) and Strained (Red) Bandgaps are Shown without Quantum Size Effect for Comparison (Barriers are $\text{GaAs}_{0.2}\text{P}_{0.8}$ ) .....	61
<b>Figure 4.10</b> Quantum Size Effect for InGaAs Well Thickness (Effects of Strain, Composition, and Temperature also Included in the Calculation) .....	62
<b>Figure 4.11</b> Electric Field Across a GaAs p-n Junction ( $N_A = 2 \times 10^{18}$ , $N_D = 1.1 \times 10^{17}$ , $x_p =$ $7.62\text{nm}$ , $x_n = 139\text{nm}$ , $E_0 = 1.9 \times 10^5 \text{ V/cm}$ ).....	63
<b>Figure 4.12</b> Electric Field Extended Across i-Layer in a p-i-n Configuration (Dashed lines indicate the field behavior with increasing p-type doping in the i-layer) ( $N_A = 2 \times 10^{18}$ , $N_D = 1.1 \times 10^{17}$ , $x_i = 300\text{nm}$ $E_0 = 4.3 \times 10^4 \text{ V/cm}$ ) .....	66
<b>Figure 4.13</b> Band Bending and Carrier Escape in the Presence of Built-In Electric Field Across i-layer( open circles = holes, solid circles = electrons) .....	68
<b>Figure 5.1</b> Basic Components of an OMVPE Growth System ( <i>MFC = Mass Flow Controller, PC = Pressure Controller</i> ) .....	73

<b>Figure 5.2</b> Run/Vent Manifold Schematic .....	75
<b>Figure 5.3</b> Optical Micrographs(1000X) of Small Surface Features on GaAs from a Gas Phase Reaction (left) and a Smooth Surface for GaAs Grown after a Divider Plate was Added to the Growth Chamber to Seperate Gas Flows(right).....	78
<b>Figure 5.4</b> Reactor Schematic .....	79
<b>Figure 5.5</b> Photograph of Reactor .....	81
<b>Figure 5.6</b> Optical Micrograph (1000X) of a GaAs Surface Grown at 70 Torr (Metallic Droplets are Presumed to be Unreacted Gallium) .....	83
<b>Figure 5.7</b> Substrate Susceptor Coverage .....	84
<b>Figure 6.1</b> Optical Micrograph (500X) Rough Surface of n-GaAs Caused by Low Growth Temperature (Arrow indicates a water stain from improper sample drying) .....	98
<b>Figure 6.2</b> Optical Micrographs (400X) of Cross Hatching in (1) Compressively Strained $\text{In}_{0.1}\text{Ga}_{0.9}\text{As}$ and (2) Tensile Strained $\text{GaAs}_{0.8}\text{P}_{0.2}$ , Plus the (3) Featureless Surface of a Strain Balanced $\text{In}_{0.1}\text{Ga}_{0.9}\text{As}/\text{GaAs}_{0.8}\text{P}_{0.2}$ SLS .....	99
<b>Figure 6.3</b> Cross-Section Optical Micrographs (1000X) of AB-Etch Delineated Interface and Edge Crown.....	100
<b>Figure 6.4</b> Optical Micrograph (400X) of Etch pits for InGaAs/GaAs Double Heterostructure and InGaAs/GaAs Strained Layer Superlattice .....	101
<b>Figure 6.5</b> $\theta$ -2 $\theta$ XRD Scan of a Thick GaAsP Film .....	103
<b>Figure 6.6</b> HRXRD Rocking Curve of a $\text{GaAs}_{0.985}\text{N}_{0.015}$ Film on GaAs .....	104
<b>Figure 6.7</b> HRXRD Scan of a Slightly Lattice Mismatched SLS with Pendellosung Fringes .....	106
<b>Figure 6.8</b> 77K PL Scans of Thick Films of $\text{GaAs}_{0.6}\text{P}_{0.4}$ , GaAs, and $\text{In}_{0.3}\text{Ga}_{0.7}\text{As}$ .....	107
<b>Figure 6.9</b> Current-Voltage and Spectral Response Test Apparatus .....	111
<b>Figure 7.1</b> Contact Metallization Schemes .....	117
<b>Figure 8.1</b> Effect of Carrier Gas on N Incorporation at 600°C.....	120
<b>Figure 8.2</b> Growth Temperature Dependence of N Incorporation in GaAsN .....	121
<b>Figure 8.3</b> X-Ray Diffraction Data for Various N Compositions in GaAsN .....	122
<b>Figure 8.4</b> PL Data for Various N Compositions in GaAsN .....	123

<b>Figure 9.1</b> XRD for Strained GaAs/GaAsP and InGaAs/GaAs and Strain Balanced InGaAs/GaAsP SLS's.....	126
<b>Figure 9.2</b> Optical Micrographs of Surfaces Corresponding to Each Sample in Figure 9.1 .....	127
<b>Figure 9.3</b> TEM of InGaAs/GaAsP SLS .....	128
<b>Figure 9.4</b> XRD for an $\text{In}_{0.14}\text{Ga}_{0.86}\text{As}/\text{GaAs}_{0.25}\text{P}_{0.75}$ SLS with 83Å Wells and 28Å Barriers .....	130
<b>Figure 9.5</b> XRD for an $\text{In}_{0.28}\text{Ga}_{0.72}\text{As}/\text{GaAs}_{0.1}\text{P}_{0.9}$ SLS with 38Å Wells and 23Å Barriers	131
<b>Figure 9.6</b> PL for Various Compositions and Well Widths (Experimental data points are color coordinated with the corresponding calculated curves) .....	133
<b>Figure 9.7</b> Typical Final Test Structure (SLS thickness ranged from 0.3µm to 0.8µm) ....	134
<b>Figure 9.8</b> AM1.5D 1-Sun Light Current of Selected Test Cells A, B, C and D Compard to GaAs Control Cell (A: $\text{In}_{0.28}\text{Ga}_{0.72}\text{As}/\text{GaAs}_{0.25}\text{P}_{0.75}$ , 30 periods, 0.2µm, B: $\text{In}_{0.28}\text{Ga}_{0.72}\text{As}/\text{GaAs}_{0.1}\text{P}_{0.75}$ , 50 periods, 0.35µm, C: $\text{In}_{0.28}\text{Ga}_{0.72}\text{As}/\text{GaAs}_{0.1}\text{P}_{0.9}$ , 50 periods, 0.3µm, D: $\text{In}_{0.28}\text{Ga}_{0.72}\text{As}/\text{GaAs}_{0.1}\text{P}_{0.9}$ , 50 periods, 0.3µm) .....	136
<b>Figure 9.9</b> Dark Current for Test Cells in Figure 9.8 .....	137
Figure 9.10 I-V of Doped SLS Devices (Dashed lines indicated reduced $I_{SC}$ and $V_{OC}$ typical of doped structures. The corresponding undoped sample is plotted as a solid curve with matching color.).....	139
<b>Figure 9.11</b> Spectral Response of Samples A(Green) and B(Red) Compared to the Reference Cell(Black).....	140
<b>Figure 9.12</b> Spectral Response of Highest Light-Current Cell and Reference GaAs Cell .	141
<b>Figure 9.13</b> Partial Band Diagram for $\text{In}_{0.28}\text{Ga}_{0.72}\text{As}/\text{GaAs}_{0.25}\text{P}_{0.75}$ SLS with 38Å Wells and 23Å Barriers.....	143

## 1 INTRODUCTION

Energy demands of humans continue to increase as the population of Earth increases and more countries become industrialized. Simultaneously, the primary energy source, fossil fuel, is being depleted at a rate much higher than it is generated. A paradigm shift is inevitable for the energy model of the entire planet. Beyond this fact, there is a great deal of disagreement about the future of energy use and production for planet Earth. A thorough treatment of this topic is far beyond the scope of this work, but it merits a brief summary as it is the ultimate motivation for this research.

### 1.1 WORLD ENERGY OVERVIEW

Three main questions arise when analyzing modern energy supply and consumption. How long will fossil fuels meet our needs? How much energy will the planet ultimately need? What are viable alternative energy sources? Many clever individuals have attempted to answer these questions,<sup>1,2,3,4</sup> but the task is daunting. Aubrecht has assembled an overview of the topic<sup>5</sup> which includes some 5400 references covering scientific works, government reports, environmental impact, politics, economics, conservation, and culture.

Estimates for the longevity of fossil fuels range from only a few years to thousands of years, but most predict a few hundred years. A major problem is estimating how much additional fuel will be found in addition to known reserves. Other concerns include conserving fossil fuels for a myriad of useful, non-energy related products and protecting the environment from the harmful effects of combustion.

When estimating future demand, one quickly realizes that the maximum population Earth can support must be finite since the Earth is also finite. Population estimates range

from 84 billion<sup>6</sup> to 2 billion<sup>7</sup> for fully sustainable energy. Energy demand per capita continues to increase which is a trend that can not continue indefinitely.

Accurately predicting future dominate energy sources is impossible, but we can identify several possibilities. Available energy sources are classified as either non-renewable or renewable as in Table 1.1. Non-renewable resources can not be regenerated on a human time-scale while renewable resources are continually refreshed and available for a very long time.

**Table 1.1** Available Primary Energy Sources

Non-Renewable	Renewable
Fossil Fuels (Oil, Coal, Natural Gas)	Hydropower
Nuclear Fission (Uranium)	Biomass (Plants, Urban Waste)
Nuclear Fusion (Deuterium-Tritium)	Wind
Geothermal	Solar

Nuclear fission produces vast amounts of energy from splitting Uranium-235, but the amount of this fissionable isotope is limited. Nuclear fusion, combining the nuclei of light elements, is the process that drives the Sun and holds enormous potential for energy production. However, commercialization is many years in the future due to problems with sustaining and confining the reaction. If the technological problems can be surmounted, there is enough deuterium, an isotope of hydrogen, in the oceans to supply energy for millions of years so fusion is sometimes classified as renewable. Unfortunately, nuclear reactions produce large amounts of radioactive waste and there is not currently a solution for safely disposing of this waste. So called “cold fusion” is mired in a confused tangle of non-

scientific and scientific debates to the point that it is not clear if it even exists. Therefore it will not be discussed here other than to point out that it may not produce exceedingly harmful waste like fission and hot-fusion. Geothermal energy can be renewable if the rate of extraction is low, suitable for a small local area. However, current large scale plants extract heat energy faster than it is supplied to the system.

Hydropower is by far the most utilized renewable energy source worldwide, primarily in the form of hydroelectric dams. Problems with this method include massive habitat and wildlife destruction in the flooded areas, safety for downstream residents, and reservoirs filling with silt. Burning plant matter such as trees is renewable if new plants are planted in place of those harvested. The new plants will also remove environmentally harmful CO<sub>2</sub> produced from combustion, making this method environmentally safe. However, there is simply not enough feedstock available to support even a significant fraction of world demand. Energy from wind comes primarily from windmills and is suitable only for areas with generally constant wind speed since lack of wind equals zero power and gusts are destructive. All of these sources can be classified as solar energy. For example, fossil fuels are solar energy in the form of organic matter, stored over millions of years. For the current discussion, solar energy refers to more direct use of solar energy such as direct thermal heating, solar electric, and photovoltaics. Solar energy is appealing because it is clean and essentially inexhaustible, but suffers from dilute incident energy requiring collection over large areas or concentration via lenses or mirrors. Nighttime storage is required for full time availability and the current produced is DC rather than grid-based AC. Overcoming these technological difficulties appears relatively easy when compared to the limitations of other sources, especially for long time scales.

Each of these energy sources will play an increasingly significant role in the inevitable demise of the fossil fuel paradigm. The primary end product of each is electricity which is suitable for stationary and grid-based power schemes. The current outlook for transportation energy requirements is grim by comparison. Automobiles and planes in particular benefit from the high energy density in petroleum fuels which provide relatively low weight, high power, and long operating distances. Current technology does not have a solution that will satisfactorily replace gasoline, diesel, and jet fuel. Industrialized nations may face a radical change in the way people and materials are moved around the globe. Each of the energy sources discussed need to be developed significantly to be viable for large scale use. This work focuses on one small part of this total energy picture with huge potential, semiconductor photovoltaics(PV).

## 1.2 CURRENT AND FUTURE ROLE OF PHOTOVOLTAIC TECHNOLOGY

Electricity generated from solar cells currently contributes only about 1% of world energy demand.<sup>1</sup> However, the amount of radiant energy from the Sun that reaches Earth's surface in one year is many times greater than the combined energy contained in all the coal, oil, gas, and uranium reserves ever known to man.<sup>8</sup> Cost and efficiency are the two main factors that have prevented widespread photovoltaic utilization.

The cost of solar cells in 1960 was about \$1 million/kW<sup>9</sup>, which dropped to \$10,000/kW<sup>9</sup> in 1985 and is currently around \$4000/kW.<sup>10</sup> This equates to about 30 cents/kWh while the average American currently pays around 7 cents/kWh<sup>11</sup> for grid delivered electricity. Clearly, the cost of photovoltaics must be closer to competing energy sources before it is generally viable. This should happen as solar cell production costs are lowered

and as fossil fuel depletion drives up average energy costs. Further cost reduction can be realized by concentrating solar radiation with lenses or mirrors that are inexpensive to manufacture relative to solar cells.

Increasing efficiency without greatly increasing cost is also critical for the development of this technology. Gains in efficiency come from concentrating solar radiation, but only to a small degree. As of 2003, Silicon (Si) photovoltaics constitute 97% of the world PV market,<sup>12</sup> largely due to the availability of high quality, large area, relatively inexpensive silicon substrates. Silicon is, however, a poor choice of material for maximizing efficiency because of fundamental limits imposed by the absorption mechanism, which will be described later. By contrast, III-V semiconductors such as Gallium Arsenide (GaAs) and related alloys are much more efficient in converting the Sun's radiation into electricity. Efficiency is further increased by using III-V's in a multijunction configuration where more than one material absorbs incident light. Silicon solar cells exhibit a rather low tolerance of solar concentration while multijunction cells can operate at concentrations several hundred times above normal. Figure 1.1 shows how different solar cell technologies have developed over 3 decades with respect to efficiency. Greater efficiency corresponds to higher energy output per illuminated area, so less satellite, land or building surface is required. The record efficiency, 24.7%, for silicon based solar cells was attained in 1998 by Green<sup>13</sup>, et. al. at the University of New South Wales and confirmed by Sandia National Laboratory in 1999. This design is complex and relatively expensive, so commercially available silicon cells typically range from 5% to 12%.<sup>14</sup> Silicon solar cell technology may already be near the real-world efficiency limit. Conversely, III-V photovoltaics have a high potential for efficiency increases. Spectrolab and the National

Renewable Energy Laboratory (NREL) each have produced multijunction solar cells approaching 39% efficiency.<sup>15</sup> Efficiency is estimated to be increased further if each junction is ideally optimized.<sup>16</sup> Developing new materials systems to optimize the junctions is the focus of this research effort.

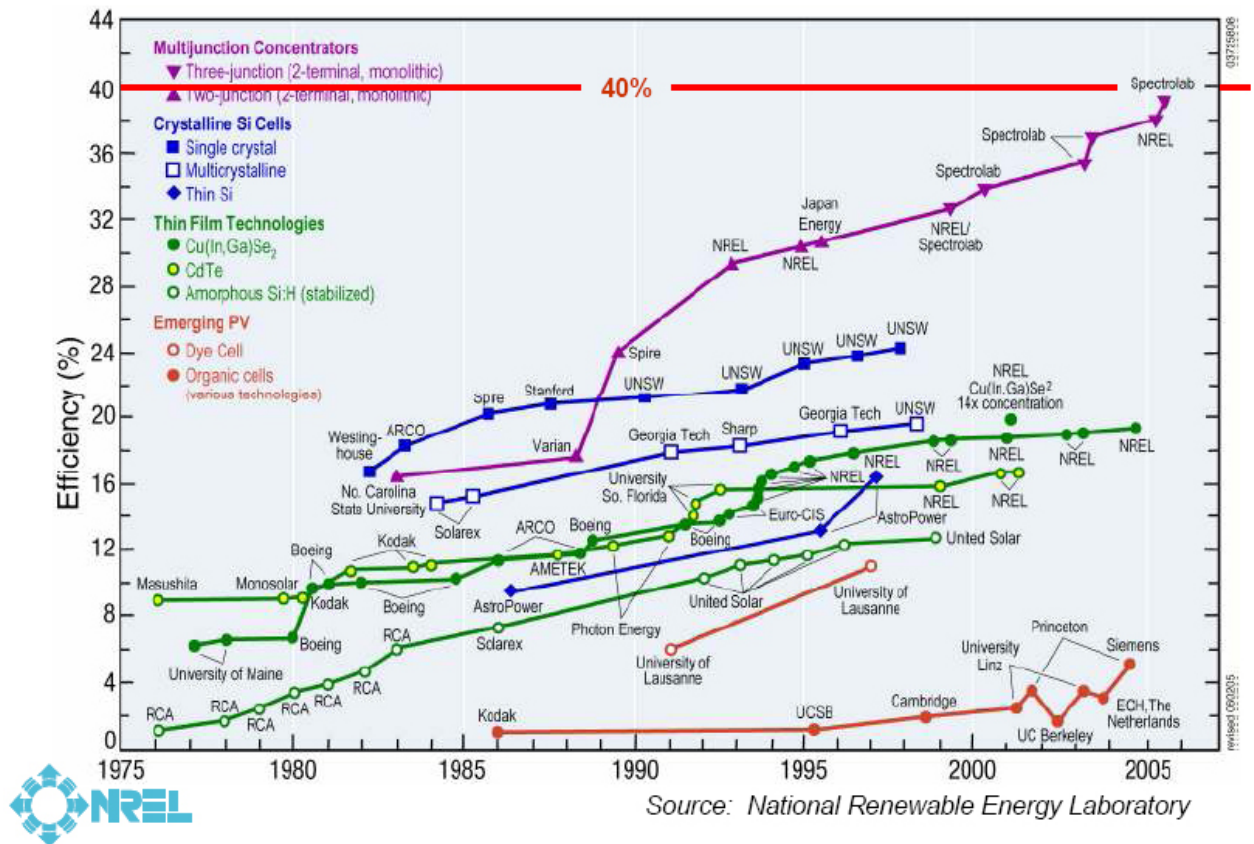


Figure 1.1 Record Cell Efficiencies

Revisiting the issue of cost in light of multijunction concentrator photovoltaics (CPV) reveals some exciting information. Silicon based arrays are usually installed in a fixed orientation because the equipment required to track the Sun across the sky is cost prohibitive. When compared to the silicon industry best 25% efficient flat plate solar arrays, multijunction, solar tracking, CPV's are projected to be equal in \$/kWh at 40% efficiency. For tracking concentrator systems, efficiencies above 40% approach the typical cost per

kilowatt-hour of grid delivered electricity.<sup>17</sup> PV technology may make a significant penetration into the market very soon and begin to fulfill the long awaited dream of clean affordable energy. Several models have been developed for the sustainability of high-efficiency PV installations, both large and small, and the outlook is favorable especially for larger installations.<sup>18</sup>

The focus of the research presented here is to develop a novel junction that can be incorporated into existing multijunction structures to improve efficiency. The following chapters define the requirements of this junction and introduce a materials system to meet the requirements. Basic physics of solar cells is presented in chapter 2. Chapters 3 and 4 outline the modern state of solar cell technology, specifies limitations to efficiency, and describes a novel solution for potential efficiency improvement. Chapters 5, 6, and 7 detail how the solar cell material is produced, characterized and processed into a complete device. Experimental results and discussion of the research are found in chapters 8 and 9. Finally, several conclusions are presented in chapter 10.

## 2 PHOTOVOLTAIC BASICS

Semiconductor photovoltaics provide a means to convert sunlight directly into electrical energy. This process does not produce any byproducts that are harmful to humans or the environment. The fundamental physics of solar cells is well understood and has been thoroughly analyzed by scientists and engineers.<sup>19,20,3</sup> This basic understanding is the starting point for making improvements in the technology.

### 2.1 SOLAR IRRADIANCE

Any meaningful discussion of photovoltaics requires a knowledge of the available resource, solar radiation. Light consists of elementary particles, or photons, which exhibit both wave and particle behavior; a phenomenon called wave-particle duality. A given photon has a specific energy,  $E_{ph}$ , and wavelength,  $\lambda$ , related by

$$E_{ph} = \frac{hc}{\lambda} \quad [ 2.1 ]$$

where  $c$  is the speed of light in a vacuum and  $h$  is Planck's constant. Photons may be characterized by either energy or wavelength depending on which is convenient for the topic at hand, but energy units are typical for PV discussions.

At the surface of the sun, the power density is  $6.30 \times 10^{10} \text{ W/m}^2$ . Once this radiation reaches just outside the atmosphere of Earth, approximately  $1.5 \times 10^8 \text{ km}$  away, the power density is  $1353 \text{ W/m}^2$ , defined as the Solar Constant. Of course this value fluctuates with solar activity, such as flares, and with small changes in the distance from the Sun during orbit, but it serves as a convenient measure for calculations and experimental comparisons. This spectrum is referenced as Air Mass Zero or AM0, where the Air Mass factor is defined

as the secant of the angle from the zenith to the Sun. The Earth's atmosphere further attenuates the intensity and additional Air Mass units are used to account for this as well as variations in latitude. AM1 represents the intensity at high noon at the equator and AM2 represents higher latitudes and/or early and late times of the day. Scientists and the photovoltaic industry require a common standard for calibration and comparison of solar cells. AM0 is used for space applications<sup>21</sup> but the best standard for terrestrial applications is frequently debated and changed as additional data is collected for both the incident spectrum and solar devices. Currently, AM 1.5 at 1000 W/m<sup>2</sup> is the generally accepted standard<sup>22</sup>. This value is too high in reality, but provides a convenient round number for comparison. Real AM 1.5 values are closer to 963 W/m<sup>2</sup> global (37° tilt including diffuse reflection from the ground) and 768 W/m<sup>2</sup> direct (does not incorporate ground reflection). The American Society for Testing Materials (ASTM) has recently released a new more flexible standard<sup>23</sup> for testing terrestrial solar cells that incorporates valuable considerations of modern test equipment such as solar simulators, lenses, and filters. This standard may help researchers and production facilities to communicate data and results more effectively. AM0 and AM 1.5 Direct irradiance is shown in Figure 2.1. Note that the AM0 spectrum is almost identical to black body radiation at 6000K. Indeed, the surface temperature of the Sun is roughly 6000K. Large dips in the terrestrial spectrum are caused by strong absorption of some wavelengths by water vapor, carbon dioxide, oxygen molecules, aerosols, and dust in the atmosphere.

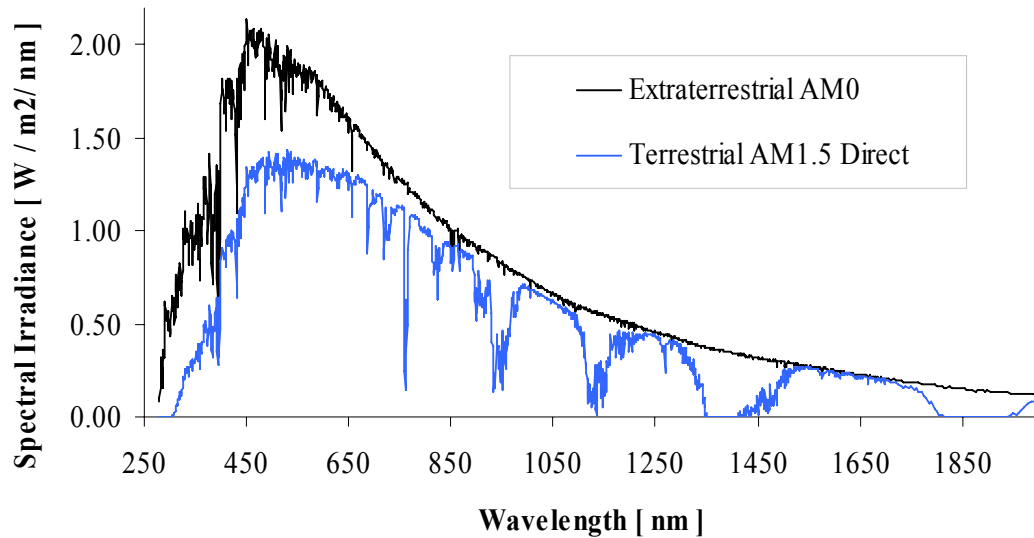


**Figure 2.1** Standard AM0 and AM1.5 Direct Spectra

## 2.2 SEMICONDUCTOR MATERIALS PROPERTIES

Most photovoltaics are constructed of semiconductor materials such as Silicon or GaAs. Large area single crystals are produced routinely by a variety of methods.

Semiconductor material properties<sup>24,25</sup> and device physics<sup>26,20,19,27</sup> are well understood and thoroughly described in the literature. Only critical principles relating to solar cells are described here.

### 2.2.1 Crystal Structure

Some solar cells are amorphous or polycrystalline, but the best, most predictable performance comes from single crystals. Atoms within the crystal are arranged in a lattice of repeating patterns in three dimensions. The lattice can be described by defining the atom positions in a repeating unit cell. Unit cells are defined by three vectors for the axes and

three interaxial angles. Seven different types of unit cells can be defined as crystal systems to represent all lattices. Bravais demonstrated that all lattice networks can be created from only 14 standard unit cells derived from variations of the seven crystal systems.<sup>28</sup> Miller indices are a notation system used to identify directions and planes in the lattice.<sup>29</sup> Properties can vary significantly along different crystal directions so specific orientations are chosen based on the application. Detailed discussions of crystallography can be found in the literature.<sup>30,31,32</sup> For this work, the cubic crystal system and, in particular, the face centered cubic (FCC) Bravais unit cell shown in Figure 2.2, is of interest. The unit cell is a cube, so all sides are equal in length and all angles between the axes are orthogonal. Atoms are located at each corner and in the center of each cube face. Atomic spacing along an edge is constant for a given material and is called the lattice parameter or lattice spacing.

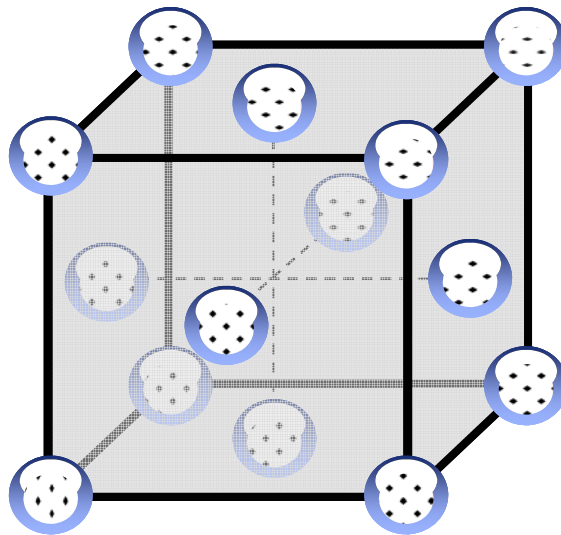


**Figure 2.2** Face Centered Cubic Unit Cell

There are voids, or interstitial sites, between the atoms in a crystal. The FCC unit cell has two types of interstitial sites, octahedral and tetrahedral. Octahedral sites have six nearest equidistant neighboring atoms. Tetrahedral sites have four nearest neighbors. Common solar cell materials like Si and GaAs consist of two interpenetrating FCC sublattices shifted by  $\frac{1}{4}$  of a lattice parameter in each direction. As a result, half the tetrahedral sites in a unit cell are occupied by atoms in the second sublattice. When all atoms are of the same type as in Si, the structure is called Diamond Cubic, analogous to the arrangement of carbon atoms in diamond. For binary materials, half the tetrahedral sites are occupied by anions and the regular FCC positions are occupied by cations or vice versa as shown in Figure 2.3. This structure is called Zinc Blende after the mineral with the same structure.

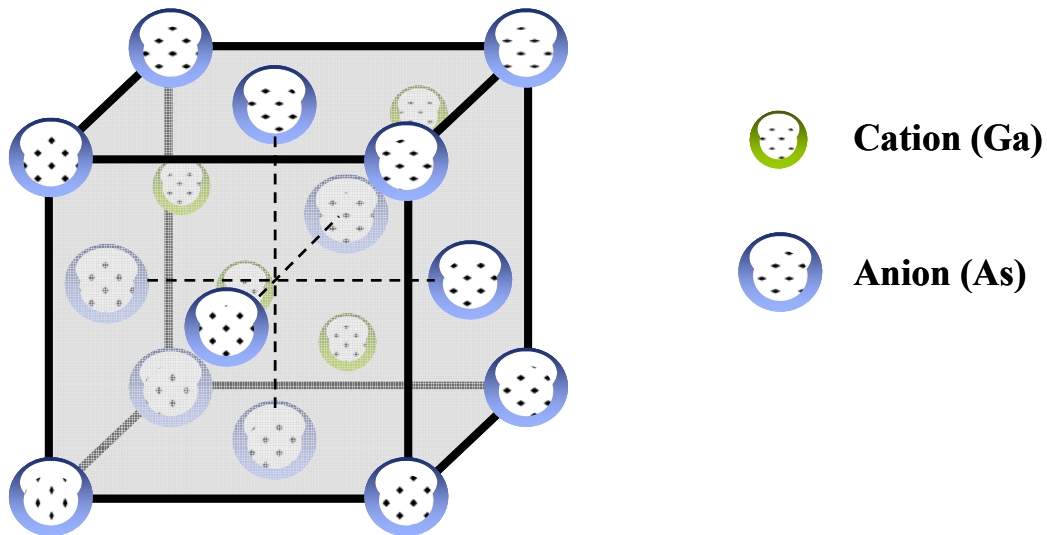
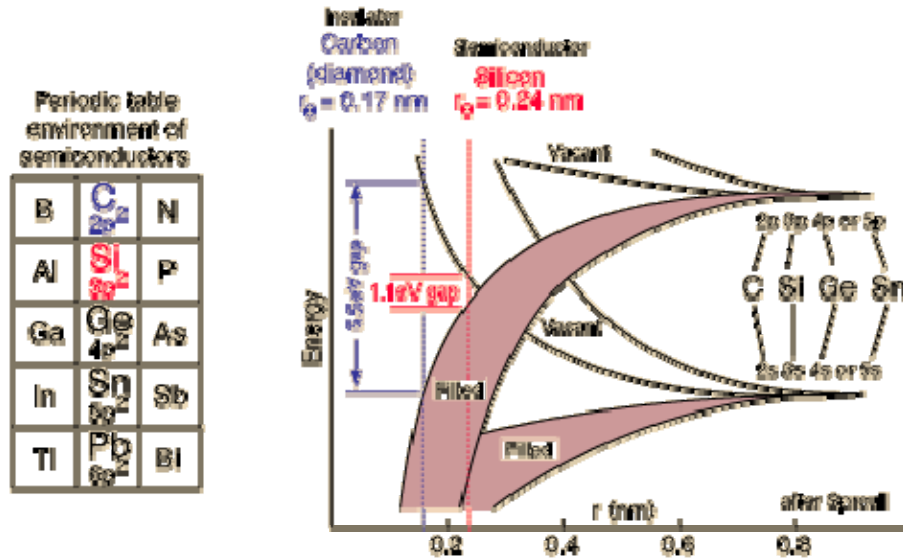


Figure 2.3 Zinc Blende Structure

## 2.2.2 Energy Bands in Semiconductors

Quantum mechanics is required to describe the electronic structure of semiconductor materials that is responsible for the photovoltaic effect. Every object in the universe has a wave function,  $\Psi$ , which contains all observable properties of the object but can not be physically observed itself. As atoms come together to form a solid, attractive and repulsive forces balance to establish the equilibrium interatomic spacing for that material. If two atoms are separated by a distance large enough to prevent wave function interaction then both atoms can have identical electronic structures. As the atoms move closer together, the wave functions overlap. In individual atoms, the Pauli Exclusion Principle<sup>33</sup> dictates that no two electrons of the same spin can occupy the same energy level. Also, electrons are limited to occupy only certain discrete energy levels. Likewise for solid materials, the Pauli Exclusion Principle states that in a closed system, no two electrons can have the same quantum state which requires the discrete energy levels of the atoms to split. The split energy levels belong to the collection of atoms rather than to an individual atom. In solids, many atoms bond together, the wave function extends across the entire system, and the energy bands split so finely that essentially continuous bands are formed as shown in Figure 2.4. Two bands of interest are the valence band (VB) and the conduction band (CB).



**Figure 2.4** Energy Band Formation as Atoms are Brought Together to Form Solids

AT 0K, the valence band is completely filled with the valence electrons and the conduction band is the lowest unfilled energy band. Materials are classified by the nature of these two bands. Conductors have overlapping conduction and valence bands, semiconductors have separated but relatively close bands, and insulators have a large separation between the VB and CB. This separation of the bands is called the energy band gap,  $E_g$ , and is measured in electron-volts, eV. No allowed energy states exist in this gap for electrons to occupy. The equilibrium atomic spacing,  $r_0$ , and the band gap for diamond(insulator) and silicon(semiconductor) is indicated in Figure 2.4.

A detailed investigation of the band structure of specific materials involves solving the Schrödinger equation.<sup>34</sup>

$$\left[ -\frac{\hbar}{2m} \nabla^2 + V(r) \right] \phi_k(r) = E_k \phi_k(r) \quad [ 2.2 ]$$

This is similar to finding the energy levels in individual atoms with the added complication of the periodic potential of the lattice. Lattice periodicity implies that electron distribution is

also periodic. The Bloch Theorem<sup>35</sup> states that if potential energy is periodic with an infinite lattice, then solutions of the Schrödinger equation take the following form.<sup>36,37</sup>

$$\phi_k(\vec{r}) = e^{jk \cdot r} U_n(\vec{k}, \vec{r}) = \text{BlochWaveFunction} \quad [ 2.3 ]$$

Modulation of the periodic lattice is represented by the function  $U_n(\vec{k}, \vec{r})$ . Plotting the allowed energy states versus the propagation constant,  $\vec{k}$ , gives a useful representation of the band structure. A complete E-k plot is a complex three dimensional surface and varies based on the difference in periodicity along various crystal directions. For convenience, E-k relationships are plotted in two dimensions for the crystal directions of interest. Crystal directions are indicated by regions between  $\Gamma$ , L, X, and W as shown in Figure 2.3 for Si and GaAs.

Parabolic bands of the following form are often used as approximate models near the conduction band minimum and valence band maximum.

$$E(k) = \frac{\hbar^2 |k|^2}{2m_o^*} \quad [ 2.4 ]$$

Effective mass,  $m_o^*$ , is similar to the mass of a free electron,  $m_o$ , but accounts for the electron or hole interaction with the periodic potential of the lattice. Values for effective mass are normally given as a fraction of  $m_o$  which can be greater than or less than 1. Since the parabolic curvature is usually different for the valance and conduction bands in a given material, the effective mass must also be different. Hole effective mass,  $m_h^*$ , is typically larger than electron effective mass,  $m_e^*$ , which is consistent with the curvature difference apparent in Figure 2.5. Multiple concurrent band maxima in the valence band with different curvatures indicate the existence of light and heavy holes with effective mass,  $m_{lh}^*$  and  $m_{hh}^*$

respectively. Effective mass is a very useful parameter for band related mathematical modeling.

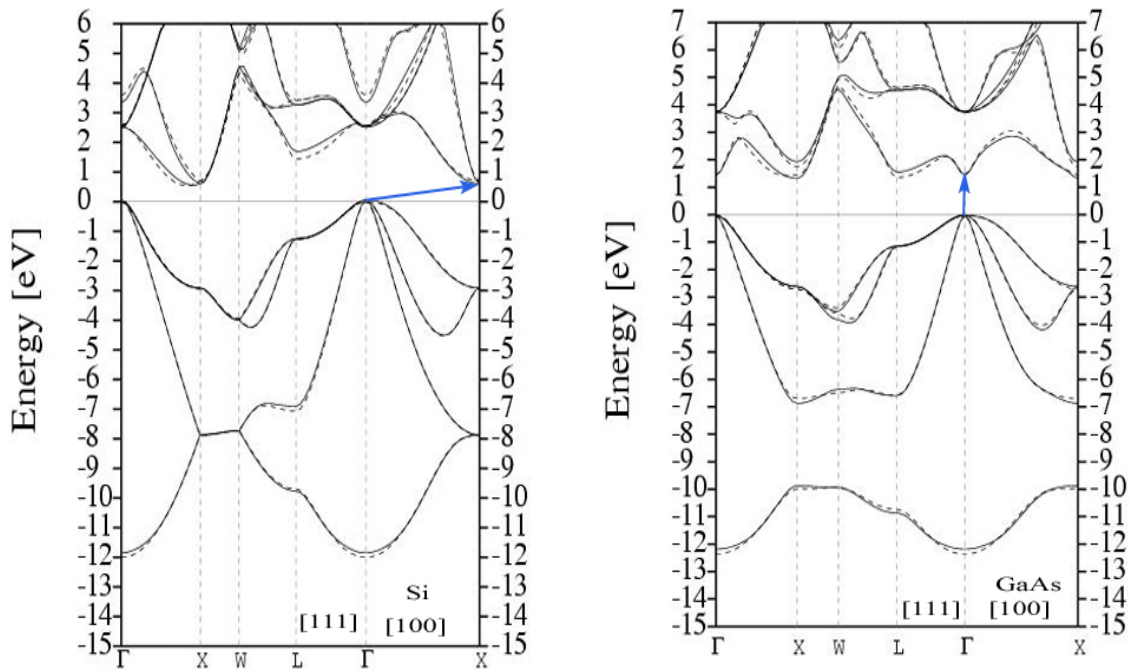


**Figure 2.5** Energy Band Structure of Si and GaAs (After Chelikowski<sup>38</sup> and Cerdá<sup>39</sup>)  
Arrows Indicate Indirect Transition in Si and Direct Transition in GaAs

The band structure reveals the fundamental reason that Si has low optical photon absorption and is an inferior material for solar cells. Consider an electron jumping from the top of the valence band to the bottom of the conduction band, indicated by the blue arrows. For GaAs, the transition is aligned in k-space so no change in the  $\vec{k}$  value, or momentum, is required. For Si, there must be a change in momentum which usually involves interaction with the lattice or a defect. Electrons give up some of their energy as heat during this interaction, thus partially limiting the usefulness of Si as a solar cell or other optoelectronic device. A much more important limitation of indirect transition, relating to photon

absorption, will be discussed in the next section. Semiconductors are classified as either direct like GaAs or indirect like Si.

An important parameter that comes from band structure analysis is the Fermi level,  $E_F$ . At absolute zero, electrons have no kinetic energy and fill the available energy states lowest to highest until all available electrons are bound. The Fermi level is the top of this collection of electron energy levels and is symmetrically located between the filled and unfilled states, so all states below are filled and all state above are empty. Among other things, the Fermi level is a natural reference point for predicting the distribution of electrons over allowed energy levels given by the Fermi-Dirac distribution function.<sup>40,41</sup>

$$f(E) = \frac{1}{1 + e^{\frac{(E-E_F)}{kT}}} \quad [ 2.5 ]$$

As temperature increases, there is some probability that states below  $E_F$  are empty and an equal probability that states above  $E_F$  are filled. The Fermi level lies in the bandgap of semiconductors so it is important to understand that the Fermi-Dirac function is the probability that an electron will occupy an available state. No available states exist in the bandgap so there is zero probability of finding an electron there.

### 2.2.3 Electrons and Holes

Electrical and thermal conduction is zero for a pure or intrinsic semiconductor at absolute zero temperature because all electrons are bound to the atoms. As temperature increases, the lattice begins to vibrate and imparts enough kinetic energy to some of the electrons to break free as illustrated with an greatly simplified band diagram in Figure 2.6. These free electrons have been promoted to the conduction band and are available for both thermal and electrical conduction. Voids, or holes, left behind by free electrons can be

treated as positively charge particles that can also conduct charge. In reality, electrons move in the valence band just as they do in the conduction band. However, it is convenient keep track of the relatively small number of holes that have the same dynamic as electrons except the charge is opposite so holes move the opposite direction of electrons in the presence of an electric field. Electrons move in the opposite direction of an applied field and holes move in the field direction.

- **Electron**

- **Hole**

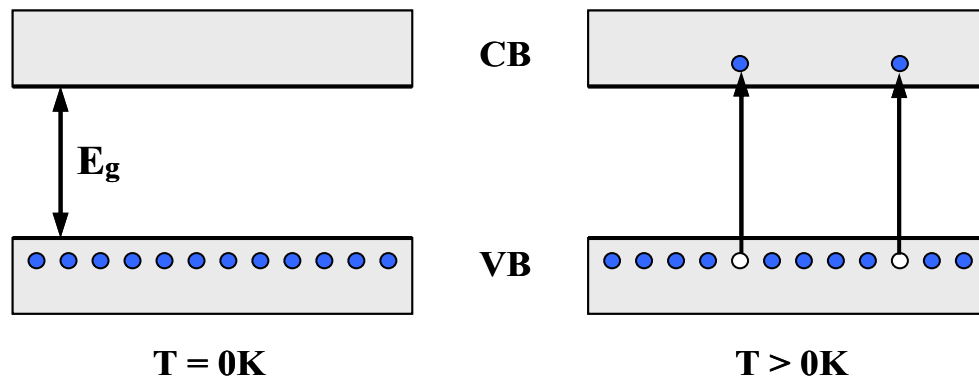


**Figure 2.6** Simplified Diagram of Valence and Conduction Bands, Bandgap, and Electron and Hole Behavior at Absolute Zero and Finite Temperatures

Thermal excitation of carriers across the bandgap is inadequate for the conduction necessary in most devices at reasonable temperatures. Two other methods of free carrier generation are crucial for many devices, including solar cells. When a semiconductor is exposed to light, photons with energy greater than  $E_g$  will be absorbed by electrons in the valence band, imparting enough energy to promote them to the conduction band, shown in Figure 2.7. This is one of the fundamental processes that enables solar cell technology. Two features of this process are responsible for most of the overall poor efficiency of current solar cells. Photons with energy less than the bandgap pass through the

semiconductor unabsorbed and therefore do not contribute to carrier generation. Only photons with energy approximately equal to or slightly higher than the bandgap promote electrons from the top of the valence band to the bottom of the conduction band. Higher energy photons create electron-hole pairs deep in the respective bands as shown. These electrons and holes quickly move back to the band edge by giving up the extra energy as heat to the lattice. This energy lost as heat, combined with unabsorbed lower energy photons, limits solar cell efficiency more than any other parameters. For indirect material, the probability of a low-momentum photon promoting an electron to the CB is relatively low. This is the fundamental limitation of Si, or other indirect semiconductors, as a PV material.

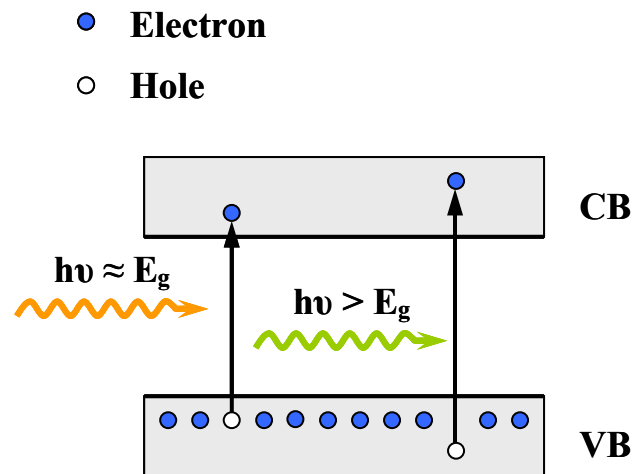


**Figure 2.7** Photogeneration of Carriers

The second method of increasing free carriers is to introduce impurity atoms with a different number of valence electrons than the host semiconductor. This process called doping, illustrated in Figure 2.8, can drastically increase conductivity. Certain impurity atoms, or dopants, create available energy states within the bandgap. Dopants with fewer

valence electrons than the host atoms, or acceptors, form energy levels just above the valence band and are able to accept electrons from the valence band. Semiconductors doped in this manner are dubbed p-type because of the positively charged holes created in the valence band. Donor dopants having additional valence electrons compared to the host atoms form energy levels just below and donate extra electrons to the conduction band, creating an n-type semiconductor. Pure undoped, or intrinsic, semiconductor material has an equal number of electrons in the conduction band and holes in the valence band. Doped, or extrinsic, material has a much higher concentration of one type of carrier versus the other. This difference in p-type and n-type plays a critical role in many devices, including solar cells. The Fermi level shifts from mid-gap to an energy between the dopant level and the band edge at absolute zero temperature. Since the dopant energy levels are close to the band edges, only a small increase in temperature is required to activate transitions. At room temperature, essentially all these carriers will be ionized.

● **Electron**

○ **Hole**

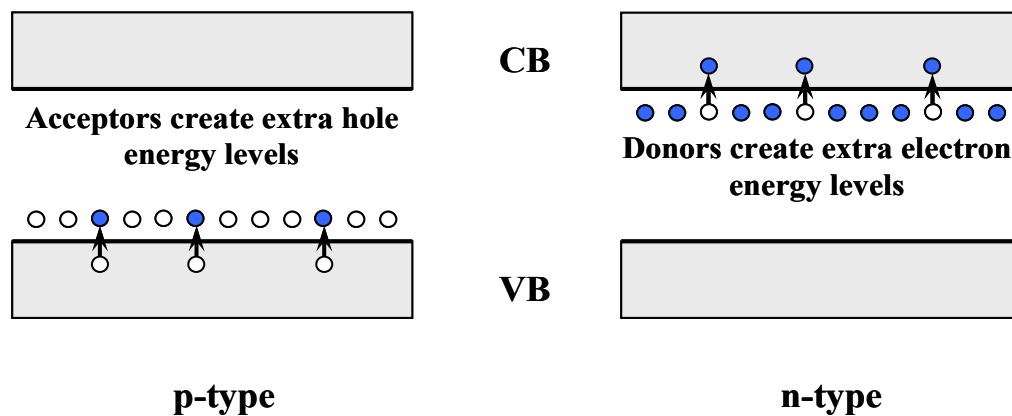


**Figure 2.8** Acceptor dopants enhance conduction in p-type semiconductors via creating holes in the valence band. Donor dopants enhance conduction in n-type semiconductors via promoting electrons to the conduction band.

A parameter of particular importance to solar cells is the carrier recombination lifetime. Electron-hole pairs created by absorption of photons remain in the excited state for a finite amount of time, usually on the order of nanoseconds. This is directly related to the diffusion length, or how far an electron or hole can travel through the material before being annihilated by recombination. For solar cells, the carriers need to remain in the excited state long enough to be collected and add to the output current. Poor material quality can drastically reduce recombination lifetimes and will be addressed later in terms of specific materials systems.

Several of the parameters discussed above are listed in Table 2.1 for GaAs and other photovoltaic binary alloys related to this work. Si is included for comparison. Properties of multinary alloys are frequently found by an appropriate approximation scheme using the binary values as endpoints.

**Table 2.1** Selected Semiconductor Parameters

	Si	AlAs	GaP	GaAs	InAs	c-GaN
Bandgap (eV)	1.1242 <sup>42</sup>	2.168 <sup>43</sup>	2.261 <sup>44</sup>	1.430 <sup>43</sup>	0.361	3.216 <sup>45</sup>
Transition	Indirect	Indirect	Indirect	Direct	Direct	Direct
Lattice	DC*	ZB <sup>†</sup>	ZB	ZB	ZB	ZB
Lattice Constant(Å)	5.431 <sup>46</sup>	5.661 <sup>43</sup>	5.451 <sup>47</sup>	5.6533 <sup>43</sup>	6.0584 <sup>48</sup>	4.52 <sup>49</sup>
Electron Effective Mass, $\Gamma$	0.188 <sup>50</sup>	0.059 <sup>51</sup>	0.135 <sup>52</sup>	0.064 <sup>53</sup>	0.025 <sup>54</sup>	0.15 <sup>55</sup>
Hole Effective Mass, $\Gamma$						
Heavy Holes	0.439	0.75 <sup>43</sup>	0.67 <sup>56</sup>	0.55 <sup>43</sup>	0.36	1.19
Light Holes	0.159	0.16 <sup>43</sup>	0.17 <sup>56</sup>	0.083 <sup>43</sup>	0.026	0.20

(values from Adachi<sup>57</sup> unless otherwise noted)

\*DC = Diamond Cubic

†ZB = Zinc Blende

#### 2.2.4 Junctions

Photogeneration of carriers is the key phenomenon for solar cells, but a driving force to move the carriers is required to create the photovoltaic effect. Otherwise, carrier lifetime dictates that the carriers will simply recombine. This force comes from the interaction of p-type and n-type material at a junction. As mentioned previously, the Fermi level lies close to the band edge for doped semiconductors as shown in Figure 2.9. The valence and conduction bands are represented by the energy levels at the top of the valence band,  $E_v$ , and the bottom of the conduction band,  $E_c$ , respectively. Forming a junction produces several effects. A high concentration of holes in p-type material and electrons in n-type material establishes a concentration gradient across the junction. Free electrons in the n-region diffuse along this gradient to combine with holes in the p-region to form negative ions at the acceptor impurity site. Positive ions are left behind in the n-region at donor impurity sites. These fixed charges at the impurity sites establish an electric field, repelling carriers with the same charge. This field builds up in the growing space charge region, opposing further diffusion. Once the field balances the diffusion driving force, the resulting space charge volume is called a depletion region due to the depletion of free carriers. Notice, from the band diagram, that the bands shift and, in fact, bend in the depletion region such that the Fermi level is constant across the junction. The distance of the Fermi, donor, and acceptor levels from the band edges is exaggerated in the diagram for demonstration purposes. This pn-junction or diode is the most basic semiconductor device and is used for a wide array of applications.

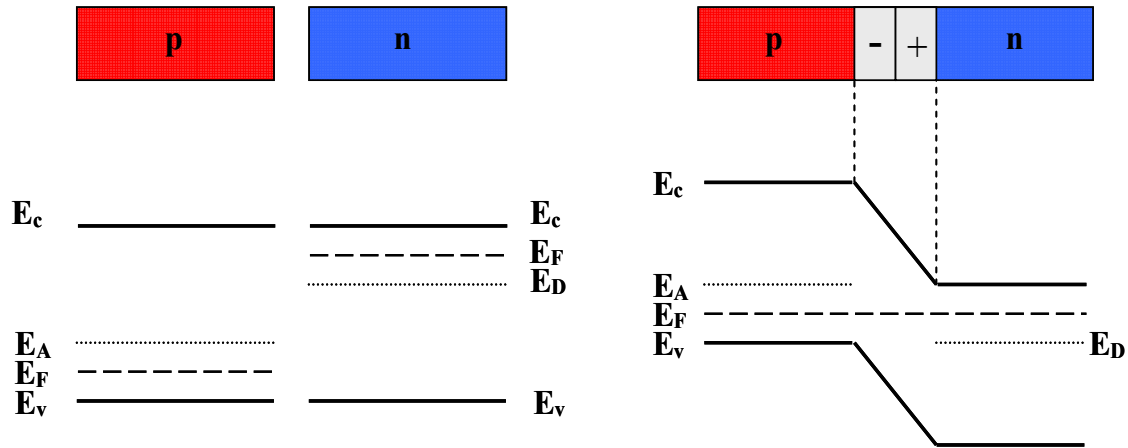


**Figure 2.9** p-n Junction Formation and Resulting Band Structure

For solar cells, excess carriers are generated from incoming photons. The built-in field of the junction separates the carriers by sweeping holes and electrons in opposite directions. Photovoltage is produced for an open circuit,  $V_{OC}$ , and photocurrent is produced for a short circuit,  $I_{SC}$ . Along with photogeneration of carriers, this phenomenon is critical for the photovoltaic effect.

## 2.3 DEVICE PRINCIPLES

For an electrical circuit, a solar cell is similar to a battery in that it delivers DC power to a load. Of course batteries produce a constant voltage from an electrochemical potential difference. Solar cells require illumination to produce the potential difference.

### 2.3.1 Photocurrent, Dark Current, and Photovoltage

Short circuit photocurrent density depends on the incident spectrum and the absorption characteristics of the solar cell. Absorption characteristics can be represented by

quantum efficiency,  $QE(E)$ , the probability that a photon with energy,  $E$ , will produce one electron for conduction. Defining  $F(E)$  as the incident flux where  $q$  is the electronic charge, the short circuit current density is given by:

$$J_{sc} = q \int F(E)QE(E)dE \quad [ 2.6 ]$$

Quantum efficiency is a useful tool for characterizing solar cells under different conditions because it depends on the absorption characteristics and transport properties of the semiconductor, but not on the incident spectrum.

Current-voltage (I-V) or current density-voltage (J-V) characteristics of the pn-junction described in section 2.2.4 are useful for describing dark and illuminated behavior and several key parameters for solar cells. Diodes pass very little current under reverse bias because the bands shift to increase the potential barrier at the junction. A forward bias reduces the barrier allowing large currents once the applied voltage overcomes the barrier. This rectifying behavior is a consequence of the asymmetric junction required for charge separation and can be seen in the J-V plot, Figure 2.10.

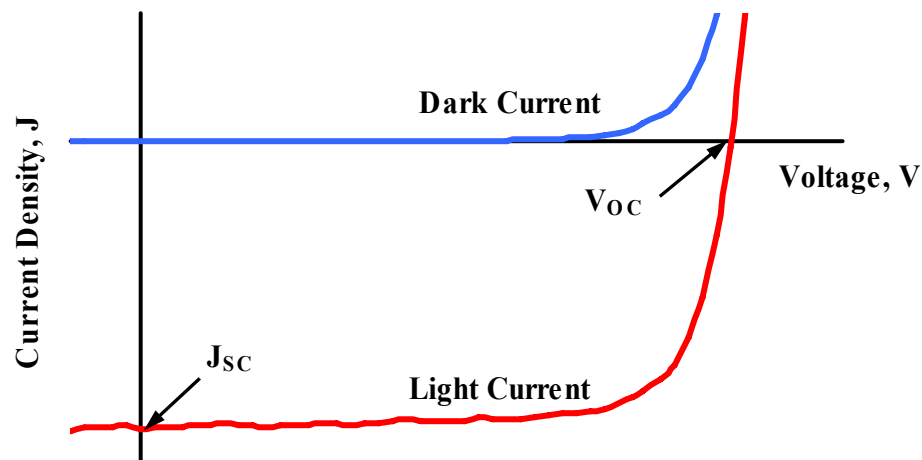


**Figure 2.10** Diode Characteristic I-V Curve

Dark current and light current represent the current passed under bias for a diode in the dark and an illuminated diode, respectively. The light current curve passes through the third quadrant where power is produced. For a solar cell connected to a load, a potential difference is established between the terminals resulting in a current opposing and reducing the photocurrent. While this current is not necessarily equal to the dark current, it is a good approximation for many solar cells and the dark current density can be easily calculated for an ideal diode by the Shockley diode equation.<sup>58</sup>

$$J_{Dark}(V) = J_0 \left( e^{qV/kT} - 1 \right) \quad [ 2.7 ]$$

$J_0$  is a constant,  $k$  is Boltzmann's constant, and  $T$  is temperature in Kelvin. Net current density for an ideal diode is a sum of the photocurrent,  $J_{SC}$ , and the dark current,  $J_{Dark}$ , where  $J_{SC}$  is designated as positive.

$$J(V) = J_{SC} - J_0 \left( e^{qV/kT} - 1 \right) \quad [ 2.8 ]$$

Many factors in real solar cells may limit the net current, so an ideality factor,  $n$ , is used to modify the equation above to reflect actual performance.

$$J(V) = J_{SC} - J_0 \left( e^{qV/nkT} - 1 \right) \quad [ 2.9 ]$$

When the dark current equals the photocurrent, the net current is zero. This is analogous to an open circuit where voltage is at a maximum,  $V_{OC}$ . Solving the equation above for this condition yields:

$$V_{OC} = \frac{kT}{q} \ln \left( \frac{J_{SC}}{J_0} + 1 \right) \quad [ 2.10 ]$$

Notice in Figure 2.10, the current-voltage product is negative from 0V to  $V_{OC}$ . This is the range where solar cells are operated and produce power. For  $V > V_{OC}$ , power is consumed and photons are emitted which is characteristic of another important optoelectronic device, the light emitting diode (LED). Photodetectors operate in the regime where  $V < 0$ .

### 2.3.2 Fill Factor and Efficiency

Maximum power output for a solar cell occurs at some point along the J-V curve where the current-voltage product is maximized. A power rectangle can be drawn by connecting this point to the axes as shown in Figure 2.11. Comparing this area to the light current curve yields the fill factor, FF.

$$FF = \frac{V_m J_m}{V_{OC} J_{SC}} \quad [ 2.11 ]$$

Ideally, the FF will cover as much area as possible under the J-V curve.

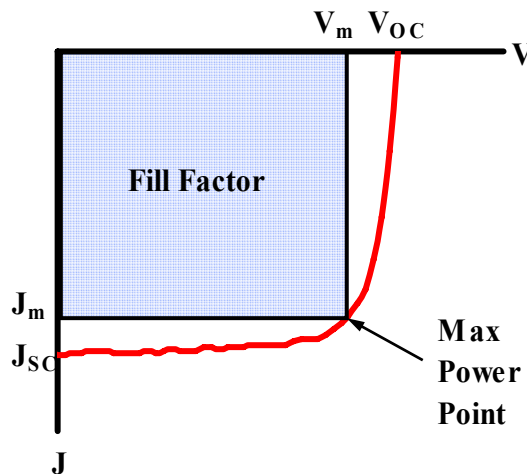


**Figure 2.11** Maximum Power Rectangle or Fill Factor

For real cells, power is lost via the series resistance and leakage currents along defects or the sides of the device. The fill factor reveals these performance limiting parameters. In an equivalent circuit, these can be represented as two parasitic resistances. Series resistance,  $R_S$ , is a concern for the metal contacts and should be as low as possible, especially when concentrators are used to give a high current density. Resistance for any parallel or shunt leakage currents,  $R_{Sh}$ , should be as high as possible. Figure 2.12 demonstrates the effect on J-V curves of a decreased  $R_{Sh}$  and an increased  $R_S$ . In both cases, the maximum power point is shifted such that FF is reduced.

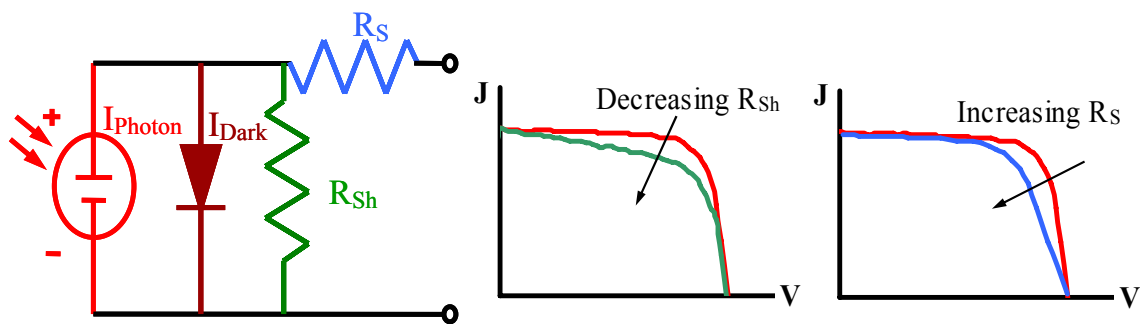


**Figure 2.12** Equivalent Circuit & Parasitic Resistances

Most modern photovoltaic research and development, including this work, focuses on increasing output power via some scheme that increases efficiency. Efficiency is a ratio of the power density at  $V_m$  and  $J_m$  to the incident power,  $P_i$ . The fill factor allows efficiency to be calculated in terms of  $V_{OC}$  and  $J_{SC}$ . Clearly, any reduction in fill factor, as in Figure 2.12, is detrimental to efficiency.

$$\eta = \frac{V_m J_m}{P_i} = \frac{V_{OC} J_{SC} FF}{P_i} \quad [ 2.12 ]$$

For a fixed incident spectrum, the relations presented in this chapter can be solved to predict the maximum possible efficiency based on bandgap alone. The detailed-balance approach proposed by Shockley<sup>59</sup> provides a more rigorous and general prediction of maximum thermodynamic efficiency. A general numerical computer model, consistent with detailed-balance assumptions, has been developed to accurately predict the maximum efficiency dependence on bandgap for given spectra. Radiative recombination is the only loss mechanism included in the model as other loss mechanisms depend on specific device parameters. A model for a particular device would include the effects of series resistance, material quality, device structure, etc. Therefore, the detailed-balance efficiency should be perceived as a starting point from which the efficiency degradation from each loss mechanism can be subtracted. Any reported value above this limit is unrealistic and should be cautiously scrutinized. Results for the AM 1.5 Direct spectrum are shown in Figure 2.13 along with the independently confirmed record efficiency for both GaAs<sup>60</sup> and Si.<sup>13</sup> These record values for real world devices already approach the thermodynamic limit. When considering additional loss mechanisms, alternative PV solutions are required for further significant efficiency gains.

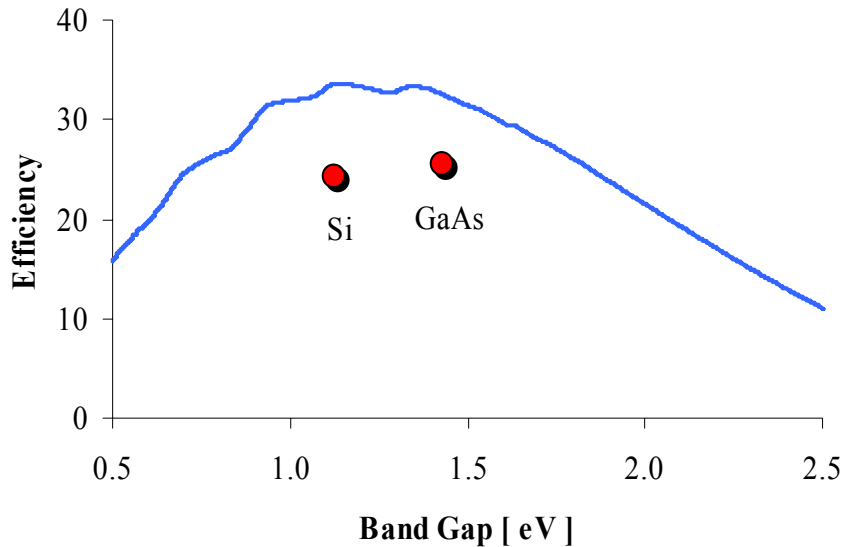


**Figure 2.13** Limiting Efficiency for Single Junction Solar Cell. Verified Record Efficiency for GaAs and Si Indicated in Red

### 2.3.3 Cell Design Considerations

Optimizing a solar cell design is an exercise in compromise as many of the requirements are conflicting. For the top metallic contact, the coverage should be minimized to avoid blocking incident photons which indicates contacting only the sides of the layer. In contrast, the diffusion lengths of carriers are too short to be collected by side contacts. As a consequence, thin metallic fingers are spread across the surface and connected via a bus bar as in Figure 2.14 or some similar approach. The fingers must be spaced within the carrier diffusion length and should be thin to avoid shading, but not so thin that series resistance is increased.

Thin contact fingers require the top layer of the junction, usually n-type, to be heavily doped to assist conduction, but not so high that the diffusion length is greatly reduced. Heavy doping favors a strong concentration gradient across the junction which yields a large built-in voltage for efficient carrier separation. Since heavy doping is already

indicated for the n-layer, the p-layer can be lightly doped to improve carrier collection without sacrificing  $V_{OC}$ . Clearly, the depletion region must extend further into the lightly doped region to reach equilibrium.

High quality semiconductor surfaces are fairly reflective such that more than 30% of the incident power can be lost before any interaction with the junction is possible.

Therefore, essentially every modern solar cell has an anti-reflective(AR) coating with an index of refraction between the index of the semiconductor and air. AR coatings are optimized to channel the preferred photons into the semiconductor.

Junctions should be near the surface. Otherwise, carriers generated in material above the junction will be lost to recombination before they can be collected. Simultaneously, the total junction thickness should be greater than the absorption length. We have assumed to this point that any thickness will absorb all electrons with energy greater than  $E_g$ , but this is incorrect. For a photon to be absorbed, it must have an opportunity to interact with an electron in the correct energy and momentum state for excitation across  $E_g$ . This may not occur in a thin material resulting in the photon passing through un-absorbed. The absorption coefficient,  $\alpha$ , is used to describe this phenomenon. Indirect semiconductors require much greater thickness to absorb all incoming photons since the carriers are not aligned in momentum space. For example, Si requires nearly  $100\mu\text{m}$  to absorb a comparable fraction of photons as  $1\mu\text{m}$  of GaAs.<sup>3</sup> Junction depth and thickness must be balanced for best performance.

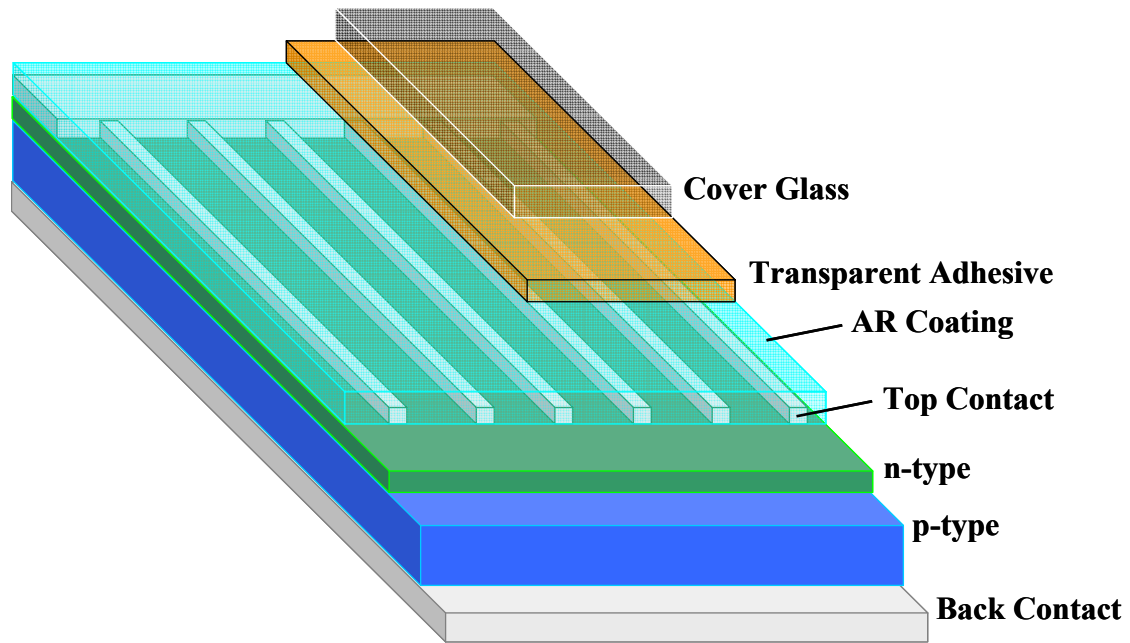


**Figure 2.14** Typical Solar Cell Design

The solar cell structure in Figure 2.14 is the result of striking a compromise between the many competing requirements for optimum performance. Notice that the thin n-type layer places the pn-junction near the surface. In addition to the features already mentioned, a top covering of glass is attached to the cell with a transparent adhesive. Glass provides excellent protection for the elements and can be cleaned easily if necessary.

### 3 MULTI-JUNCTION SOLAR CELLS

Since a single photovoltaic junction has a rather low limit of efficiency, an obvious solution is to use multiple junctions to absorb different parts of the spectrum. Each individual junction can then be illuminated with photons of energy close to the bandgap. Efficiency increases in each junction and can be combined into a greater overall efficiency by electrically connecting them in series or parallel. The concept was proposed as early as 1955,<sup>61</sup> but technology at the time was inadequate to develop useful devices. Several schemes have since been developed and each has certain benefits and detriments.

Dichroic mirrors selectively reflect light based on wavelength and can be used to split the spectrum onto different junctions.<sup>62</sup> Efficiency gains have been realized by this method,<sup>63</sup> but there are several factors that make this approach cumbersome. Processing, packaging, mechanical support, electrical connections, power conditioning devices, and labor are increased by a factor equal to the number of junctions making production costs a serious concern. Also, the dichroic mirrors are responsible for a small amount of loss and must be specialized for each junction. Typically, junctions used in this manner are connected in parallel which allows individual control of each and overall current is increased. Increased current can be useful, but also suffers from series resistance losses.

A more clever solution is to stack the junctions, using the top junction as a filter to collect high energy photons and transmit lower energy photons to the next junction. In the literature, this scheme may be referred to as a cascade, tandem, or multijunction solar cell. Mechanical stacking of junctions has also been developed<sup>64,65,66</sup> and has similar benefits and detriments as dichroic spectrum splitting in that each junction is produced individually and

electrically contacted in parallel. Mechanical stacking can result in bulky end products and high production costs.

More promising than these two methods are monolithic stacked cells where the junctions are directly connected in optical and electrical series. First realized by Bedair, et. al<sup>67,68</sup> in a 2-junction device, this approach has been successfully developed by many for several materials systems. (See Figure 1.1) Initially, connecting junctions in series was problematic because stacking two pn-junctions results in reversed third junction between the two middle layers. However, this issue has essentially been solved via tunnel junction technology.<sup>69,70</sup> Tunnel junctions are heavily doped p+/n+ regions that essentially form an ohmic contact between solar cell junctions. Perhaps the most fundamental limiting factor with this design is the requirement that each junction produce the same current. However, current matching can be achieved and this design is an elegant stack of junctions that double as optical high-pass wavelength filters. Electrical series connection increases voltage and decreases current compared to a single junction. This is fortunate in terms of limiting the detriment of series resistance and producing emf for useful work. This device only requires two terminals and is contacted similar to a single junction.

### 3.1 LATTICE MATCHING

Recall from section 2.2.1 that a crystalline material has a characteristic lattice parameter and from section 2.3.2 that defects in a crystal can reduce solar cell efficiency via a low shunt resistance. The thin junctions of a solar cell are formed on a high quality, single crystal substrate and only a few are commercially available from specialized substrate manufacturers. Ideally, the substrate will also serve as the bottom junction. This presents a

problem for multijunction solar cells because overlying junctions with ideal bandgaps may not have the same lattice parameter as the underlying substrate. Consequently, lattice misfit dislocations can form which aid in non-radiative recombination of carriers, causing poor efficiency. Consider a layer of crystalline material formed on a crystalline substrate with a different lattice parameter. If the layer is relatively thin, the lattice mismatch strain will be accommodated elastically by stretching the atomic bonds at the interface. Strain increases with layer thickness until, at some critical thickness, misfit dislocations form to accommodate the strain.

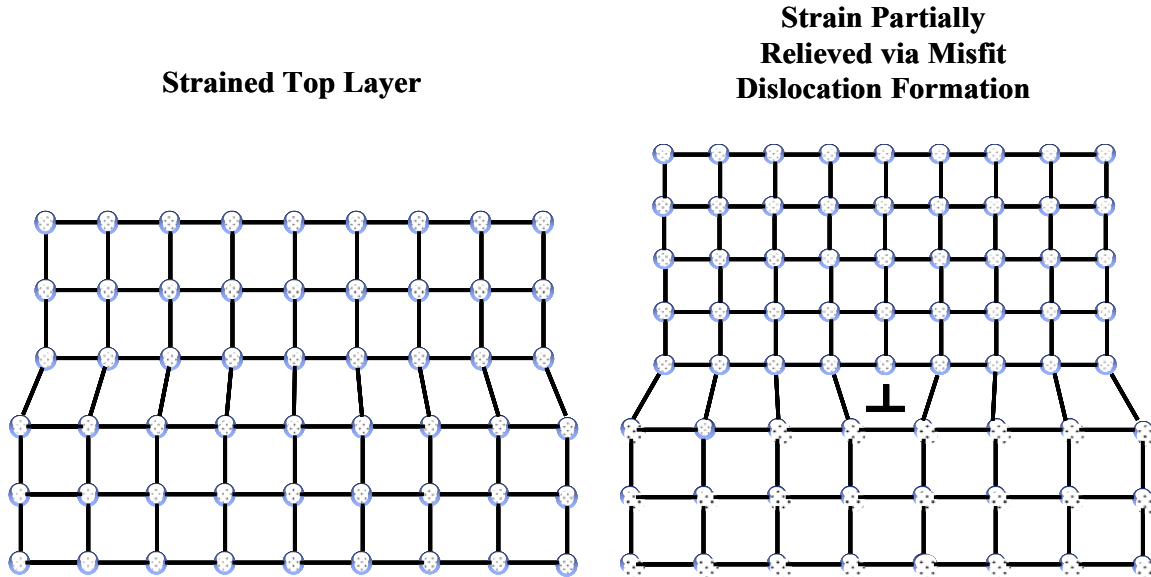


**Figure 3.1** Lattice Mismatch Strain Relaxation via Formation of Dislocations

Two well known models have been presented to predict this critical layer thickness,  $h_c$ . The Matthews-Blakeslee model<sup>71</sup> considers an equilibrium situation where the sum of strain and dislocation energy is minimized to give the following relation:

$$h_c = \frac{b(1 - \nu \cos^2 \theta)}{4\pi f(1 - \nu) \cos \lambda} \left[ \ln \left( \frac{h_c}{b} \right) + 1 \right] \quad [ 3.1 ]$$

where  $b$  is the Burger's vector,  $\nu$  is Poisson's ratio, and  $f$  is the misfit parameter. The model presented by People and Bean assumes an energy barrier exists to the formation of a dislocation such that the strain energy is equal to the dislocation energy, resulting in

$$h_c = \frac{b(1-\nu)}{32\pi f^2(1+\nu)} \left[ \ln\left(\frac{h_c}{b}\right) \right]. \quad [ 3.2 ]$$

Neither model fully describes experimental data and there is considerable debate as to why each one seems to fit certain situations. Several others have contributed both commentary and alternative models<sup>72,73</sup> to the general explanation of this phenomenon. Jain, et al<sup>74</sup> have assembled a thorough review of the topic with valuable discussion of the validity of various models. The critical layer thickness dependence on lattice mismatch is plotted in Figure 3.2 for both popular models. Matthews-Blakeslee is considerably more conservative and will be used in this work as a safe approximation.

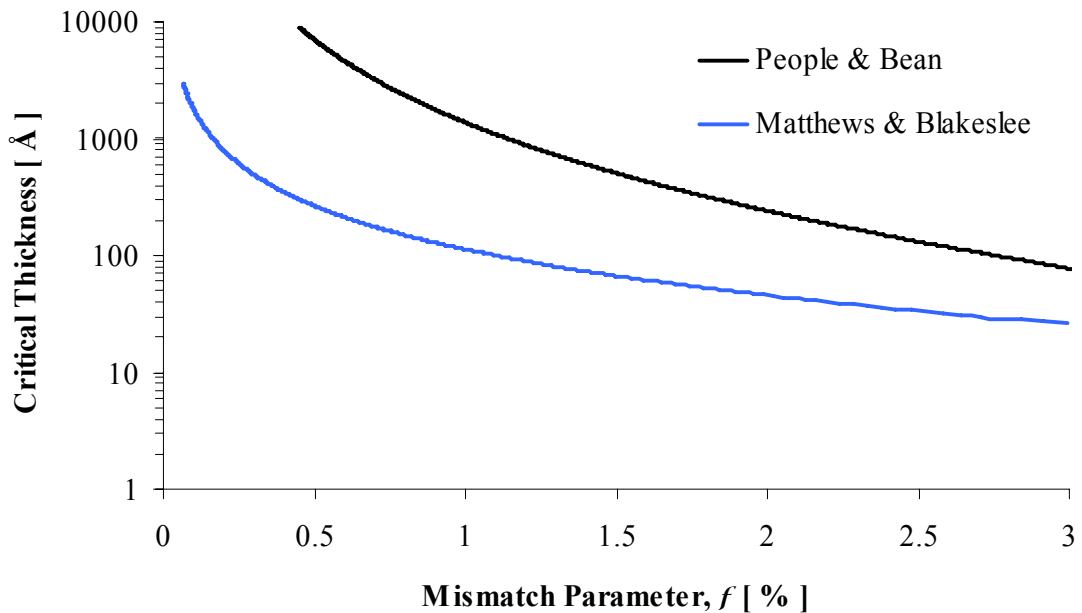


**Figure 3.2** Critical Layer Thickness as Predicted by Matthews-Blakeslee and People-Bean

## 3.2 MATERIALS FOR MULTIJUNCTION PHOTOVOLTAICS

Theoretically, the number of possible junctions has been analyzed up to the limit of infinite junctions.<sup>75</sup> In practice, two-junction (2J) cells have been developed<sup>76,77</sup> and are commercially available<sup>78</sup>. 3J cells are still being developed<sup>79,80</sup> and are available for specialized space applications.<sup>78,81</sup> 3J cells also claim the current world record efficiency<sup>60</sup> and may have potential for the terrestrial market.<sup>17</sup> 4, 5, and 6J cells have been proposed and some preliminary laboratory data can be found in the literature,<sup>82</sup> but not with any record efficiencies. The limiting efficiency model presented in Section 2.3.2 can be applied to multiple junctions to aid in material selection.

### 3.2.1 Candidate PV Semiconductors for High Efficiency

For a 2J cell, we would like to know the bandgap of each cell that yields the highest combined efficiency. The model predicts 1.56eV for the top cell and 0.93eV for the bottom cell for AM 1.5D and no concentration, which is consistent with previous predictions.<sup>83</sup> To visualize the data, a contour plot is constructed of the bottom cell bandgap versus the top cell bandgap, as in Figure 3.3. Iso-efficiency lines indicate the change of efficiency with different bandgap combinations.

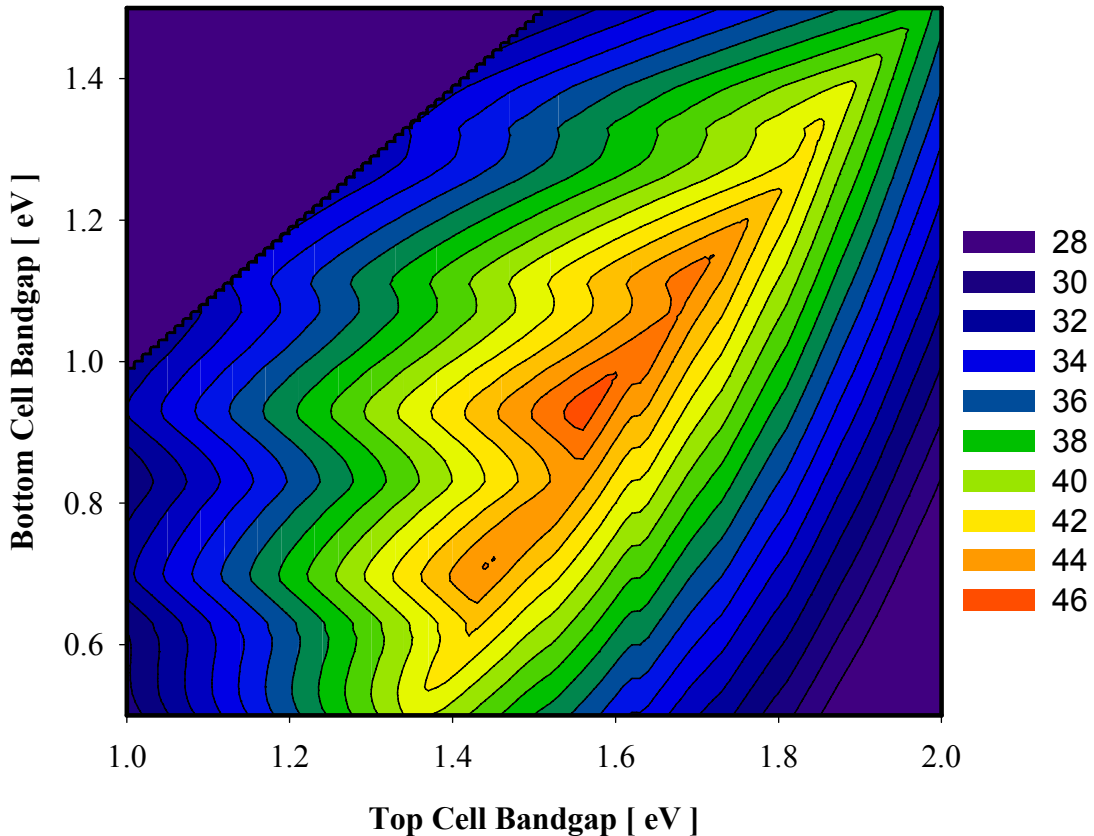


**Figure 3.3** AM1.5D 2-J Cell Thermodynamic Limiting Efficiency Contours (Maximum at 1.56eV and 0.93 eV)

Lattice matching and optimal bandgap for efficiency are the basic materials requirements for multijunction photovoltaics. Several semiconductors are available for consideration. Si and Ge have indirect bandgaps and are therefore not ideal for thin film, high efficiency solar cells. III-V semiconductors have the desired range of bandgaps to match the solar spectrum and have been developed more than other materials except Si. Compound semiconductors have the advantage of forming alloys to modify the bandgap and lattice parameter. Ternary alloys have received the most attention, but many elements may be used to form an alloy if a process is devised that yields high material quality. The recent discovery that InN has a bandgap of 0.7eV<sup>84,85,86</sup> has brought attention to the III-Nitride

system for photovoltaic applications. Alloying InN with GaN(3.4eV) covers a very wide range of the solar spectrum, but the technology is still in it's infancy. Alloys of III-Arsenides, III-Phosphides, and III-Antimonides range from around 0.4eV to 2.5eV, covering a large part of the solar spectrum. Figure 3.4 shows the bandgap dependence on lattice parameter for several important materials. The relationship for ternary alloys is usually non-linear so a bowing parameter,<sup>87</sup>  $b$ , is adapted to the linear relationship to account for the curvature seen in the blue lines connecting binary compounds. Seemingly, we can now just pick the appropriate materials from Figure 3.4 and form a high efficiency solar cell. However, not every composition of alloy can be formed with adequate quality. Coupling this with lattice matching and bandgap requirements, the number of available materials is rather limited.

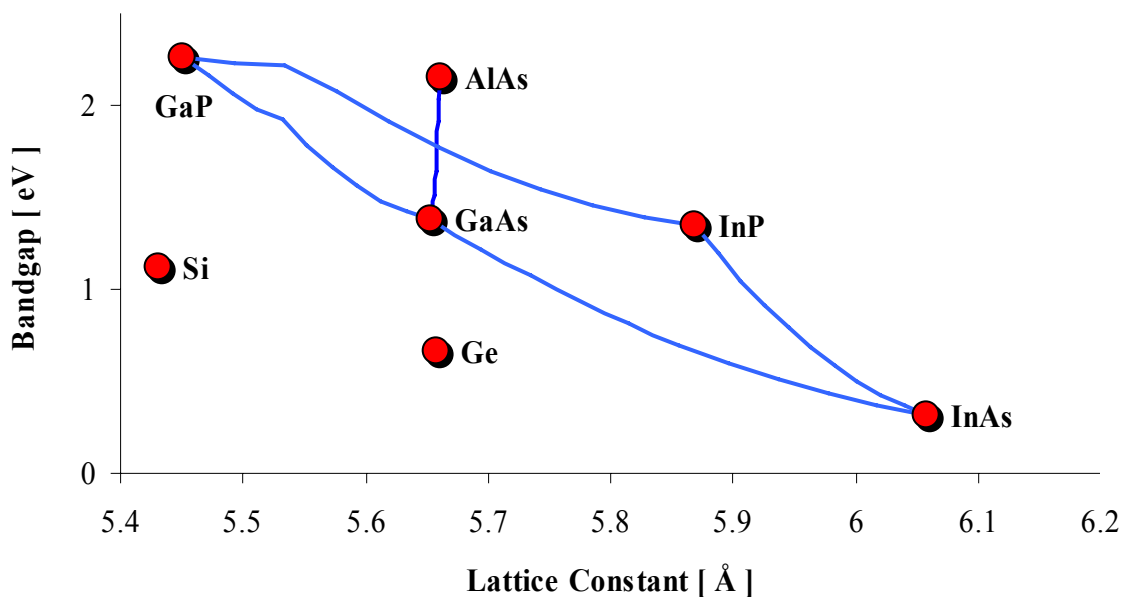


**Figure 3.4** Bandgap vs. Lattice Constant for Some Photovoltaic Semiconductors

### 3.2.2 Survey of Developed PV Materials Systems

Early work focused on using GaAs substrates as the bottom junction in part due to high-quality commercial availability and previous development for photovoltaics. The highest quality and least expensive substrates are Si, but it is clear from Figure 3.4 that none of the potential top cell materials can be lattice matched to Si. From inspection of Figure 3.3, if GaAs(1.42eV) is the bottom cell, it should be coupled with a top cell of around 1.9eV to yield the best efficiency. Two promising ternary alloys, lattice matched to GaAs, meet this requirement;  $\text{Al}_{0.4}\text{Ga}_{0.6}\text{As}$  and  $\text{Ga}_{0.5}\text{In}_{0.5}\text{P}$ . AlGaAs was used initially with promising results, but several problems, including oxygen contamination in the layers, caused inconsistent performance.<sup>88</sup> GaInP was developed<sup>89</sup> and has seen extensive use commercially. The record efficiency for this 2J arrangement steadily increased to 30.3%,<sup>90</sup> reported in 1996.

Widely available, high quality Ge substrates led researchers to utilize them in PV technology. From Figure 3.4, the lattice spacing of Ge is nearly equal to GaAs, so it can be substituted for GaAs in an existing technology with very little mismatch. Compared to GaAs, Ge has higher strength and is less expensive, but has an indirect bandgap of 0.67eV. Nearly lattice matched 2J GaAs/Ge solar cells are well developed<sup>91</sup> and widely used in space applications<sup>92</sup> with efficiency around 20%. GaInP/GaAs 2J cells have also been produced on Ge substrates for space applications with efficiencies around 23%.<sup>93</sup>

Efficiency is increased over a 1J GaAs cell in GaInP/GaAs and AlGaAs/GaAs 2J cells because high energy photons are absorbed by the higher bandgap top junction. This reduces energy lost as heat from carriers relaxing back to the band edges as discussed in section 2.2.3. Commercial success of GaInP/GaAs cells prompted the PV community to

seek a solution for the other major loss mechanism, transparency to low energy photons. A third lattice matched junction with a bandgap lower than GaAs, inserted below the GaInP/GaAs stack, could absorb some of the low energy photons and increase efficiency. Applying the efficiency model with the middle cell set to the bandgap of GaAs, again yields an optimum top cell bandgap around 1.9eV. For the bottom cell, a bandgap around 1eV is indicated as shown in Figure 3.5. Unfortunately, a high quality material with a bandgap of 1eV that is lattice matched to GaAs does not exist in the range of commonly known photovoltaics.

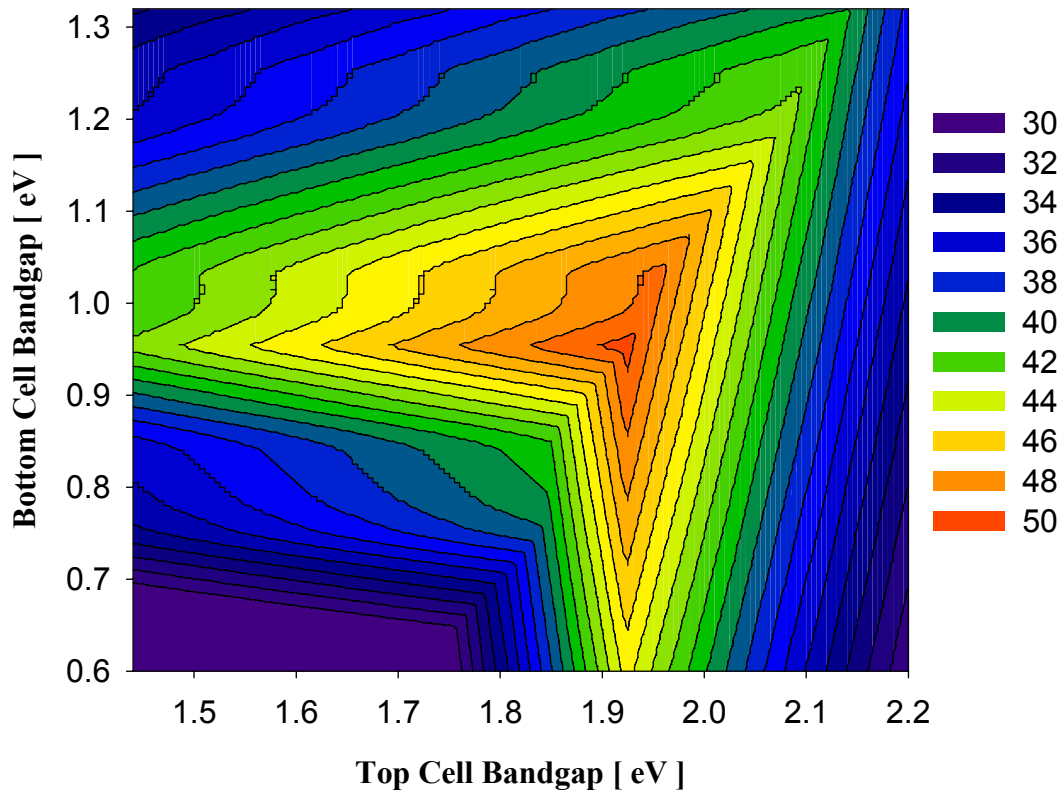


**Figure 3.5** AM1.5D 3J Top and Bottom Cell Efficiency Contours with GaAs Middle Cell

Since a 1eV junction proved to be elusive and 2J GaInP/GaAs cells on Ge had already been developed, it was a natural progression to form a third junction in the Ge

substrate. NREL<sup>94</sup> and Spectrolab, Inc.<sup>95</sup> have led the development of GaInP/GaAs/Ge 3J cells, trading record efficiencies for the past few years and have received prestigious awards for their efforts. Spectrolab narrowly holds the record at this time, as mentioned previously. The reason that Ge can be used successfully despite the indirect bandgap is because the junction is formed on the thick substrate. Low absorption coefficient requires many microns of Ge for complete photon absorption which is available in this case. A thin junction of Ge would be inadequate. The low bandgap of Ge results in excess current generation, so a fourth junction is considered between GaAs and Ge to share the photon flux. Applying the efficiency model to this 4J structure, (Figure 3.6) a bandgap near 1eV is predicted again, consistent with values found in the literature.<sup>96</sup>

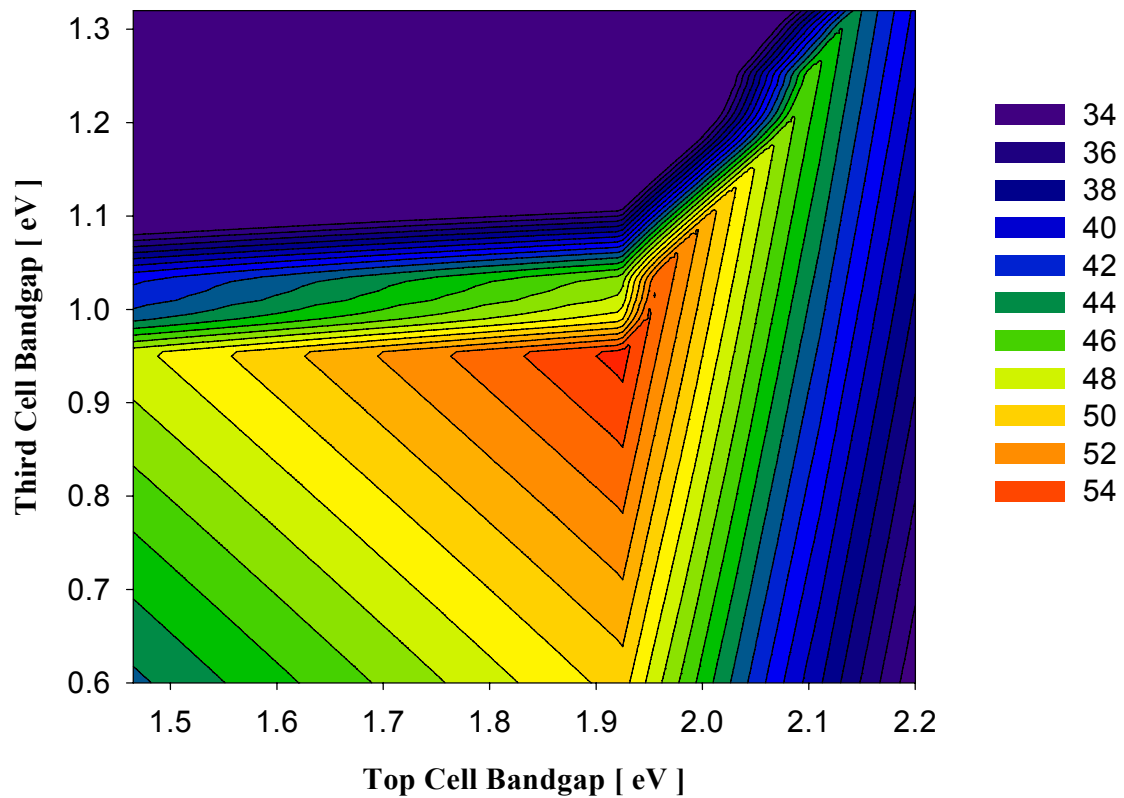


**Figure 3.6** AM1.5D Efficiency Contours for 4J Top/GaAs/3rd/Ge Cell

Without a suitable 1eV material, this established GaInP/GaAs technology is simply unable to make further large gains in efficiency. Some efficiency can be gained by adjusting the composition of the top two junctions to achieve an exact lattice match to Ge, and by tweaking the properties of each layer. Many other high efficiency multijunction arrangements can be envisioned and, in fact, have been proposed by several researchers for a variety of materials. However, none have yet proven to be commercially viable and it is not the intent of the author to detail each possibility. A viable 1eV junction could be quickly integrated into existing technology with significant efficiency gains, but which material(s) will satisfy this requirement?

### 3.2.3 Pursuit of a 1eV Lattice Matched PV Junction

The prospect of a viable 1eV junction for PV applications was grim until the mid-1990's when a relatively unknown material system was introduced. Weyers et al.<sup>97</sup> first reported optical properties of dilute GaAsN in 1992.<sup>97</sup> A strong apparent reduction of the bandgap is reported compared to GaAs, around 100meV for only 0.5% N.<sup>98</sup> Soon after, in 1994, Kondow et al. proposed GaAsN as a Si lattice matched material for light emitting diodes and noted a large bowing parameter.<sup>99</sup> Then in 1996, InGaAsN was proposed for laser diodes for the important fiber optic communications wavelengths, 1.3 and 1.5 $\mu$ m.<sup>100</sup> From this point, GaAsN and InGaAsN held the attention of the broader optoelectronic community with a variety of possible applications.  $\text{In}_x\text{Ga}_{1-x}\text{As}_{1-y}\text{N}_y$  can have a bandgap of 1eV and is lattice matched to GaAs for  $y \approx 0.35x$ , so PV researchers eagerly developed the material. In fact, part of the initial focus of this work involved investigation into thick layers of dilute nitrides, the results of which will be presented later. As with any new material, there is some confusion and disagreement about initial reports. This has prompted at least

two journals to devote an entire issue (Journal of Physics: Condensed Matter **16**, 2004 and Semiconductor Science and Technology **17**, 2002) to reviewing dilute nitrides. Henini also published a very thorough text on the topic in 2005.<sup>101</sup>

The literature is replete with reports of numerous defects and poor material quality, especially for N compositions greater than 1%. Our investigation into the growth of dilute nitrides (details reported in Chapter 8) resulted in generally poor crystalline, optical, and electrical properties with increased N composition. With respect to solar cells and other minority carrier devices, low carrier lifetime reduces performance to unacceptable levels. For the GaAs lattice matched, 1eV  $\text{In}_{0.08}\text{Ga}_{0.92}\text{As}_{0.97}\text{N}_{0.03}$  layer primarily considered for a third junction, it has been demonstrated that the carrier diffusion length is less than the depletion width for material of typical to high quality.<sup>102</sup> Additional reports on this alloy indicate poor quantum efficiency, diffusion lengths, carrier lifetime, photocurrent, and open circuit voltage.<sup>103,104,105,106</sup> Significant work has been done to isolate the specific defect(s) that result in low minority carrier lifetime. Many defects have been identified and ruled out as the primary cause. One suspicious defect has been measured by deep level transient spectroscopy (DLTS) and is the most likely culprit, but the particular defect remains unknown.<sup>107,108</sup>

Despite these troubles, adequate device performance has been demonstrated to justify continued development, especially considering the potential gains if material quality is mastered. Typical parameter values for InGaAsN solar cells grown by OMVPE are  $V_{OC} = 0.3\text{V}$ ,  $I_{SC} = 2\text{mA}/\text{cm}^2$ , and  $FF = 60\%$ .<sup>103</sup> The best reported values are from p-i-n junctions grown by MBE with values of  $V_{OC} = 0.45\text{V}$ ,  $9.5\text{mA}/\text{cm}^2$ , and  $FF = 64\%$ .<sup>109</sup> Expected open circuit voltage for a 1eV junction is around 0.6V. With respect to multijunction cells, the

low short circuit is most concerning as  $\sim 17\text{mA/cm}^2$  is required<sup>110</sup> for current matching in a 3J GaInP/GaAs/InGaAsN cell. If  $I_{\text{SC}}$  can be improved or if the required current can be reduced by adding additional junctions, this material is still very promising. Detailed analysis of 3J GaInP/GaAs/1eV and 4J GaInP/GaAs/1eV/Ge devices with an ideal 1eV junction indicate significant efficiency gains, up to 10%. However, even when the best known InGaAsN 1eV material is considered, the predicted efficiency of the 3J falls short of existing GaInP/GaAs/Ge and the 4J efficiency gains are only marginal.<sup>16</sup> Based on the observed poor material quality and repeated reports of poor performance from the literature despite rigorous efforts of many researchers, the author believes other options should be explored. While research into dilute nitrides continues, this sentiment is echoed with increasing frequency in the literature.<sup>110</sup>

## 4 PROPOSED NOVEL THIRD JUNCTION

If thick 1eV layers of dilute nitrides are inherently defective and thick layers of other III-V materials can not be lattice matched to GaAs, more complex structures can be considered.  $\text{In}_x\text{Ga}_{1-x}\text{As}$  is known to be of excellent quality in the absence of large misfit strain induced dislocations. Lattice matching to InP substrates occurs for  $x = 0.48$ , and this combination has been successfully demonstrated for waveguides,<sup>111</sup> single photon avalanche diodes(SPAD),<sup>112</sup> heterojunction bipolar transistors(HBT),<sup>113</sup> high electron mobility transistors(HEMT),<sup>114</sup> and several other devices. For  $x = 0.3$ , the bandgap is around 1eV and from experience with InGaAs, this composition can be attained with OMVPE with high quality. To take advantage of the high material quality of InGaAs for solar cells, the issue of lattice mismatch must be addressed.

### 4.1 STRAINED LAYER SUPERLATTICES

Strained layer superlattices(SLS) offer a way to avoid generation of misfit dislocations by taking advantage of the critical layer thickness,  $h_c$ , discussed in section 3.1. For example, InGaAs can be grown without misfit dislocations on GaAs with a film thickness less than  $h_c$ . However, for any useful In compositions, the critical layer thickness is relatively low, only 43Å at 30% In according to the Matthews-Blakeslee model. This very thin layer is not adequate to absorb a high percentage of photons due to the absorption coefficient. InGaAs is compressively strained to GaAs, so a second layer of tensile strained material can be grown on top of the InGaAs. This layer should have equal but opposite strain and should also remain below  $h_c$ . Strain is thereby balanced and the average lattice constant of the two layers is equal to the lattice constant of the substrate. Repetition of this

structure is used to provide enough combined InGaAs thickness for efficient absorption. Inspection of Figure 3.4 indicates the use of GaAsP as a strain balancing layer.

In general, the average lattice constant of a SLS,  $a_{SLS}$ , is given by the following equation. Strain balance is achieved when  $a_{SLS}$  is equal to the substrate lattice parameter,  $a_s$ .

$$a_{SLS} = \frac{t_c a_c + t_t a_t}{t_c + t_t} = a_s \quad [ 4.1 ]$$

$t_c$  and  $a_c$  are the thickness and lattice parameter of the compressively strained layer.  $t_t$  and  $a_t$  are the thickness and lattice parameter of the tensile layer. Also, the misfit parameter,  $f$ , or average strain between the SLS and the substrate must be zero for the strain balanced condition.

$$f = \frac{a_{SLS} - a_s}{a_s} \quad [ 4.2 ]$$

From equation 4.1, strain balance is achieved by changing composition to vary the lattice constant and/or varying the thickness of each layer until a match is found. Of course thickness has an upper limit at the CLT, which is composition dependent. A typical SLS is shown in Figure 4.1 with the resulting band diagram for a compressive layer with a band gap,  $E_{G,C}$ , less than the substrate,  $E_{G,S}$ , and the tensile layer with a bandgap,  $E_{G,T}$ , greater than the substrate. While misfit dislocations are avoided by achieving strain balance, the alternating bandgaps introduce additional complexity to the electrical characteristics and will be discussed in the following sections. An additional benefit of SLS's is that the alternating strain fields tend to bend misfit dislocations that originate from the substrate toward the edge of the film.<sup>115,116</sup> This property can be utilized as a dislocation barrier to create a dislocation-free template for active layers.

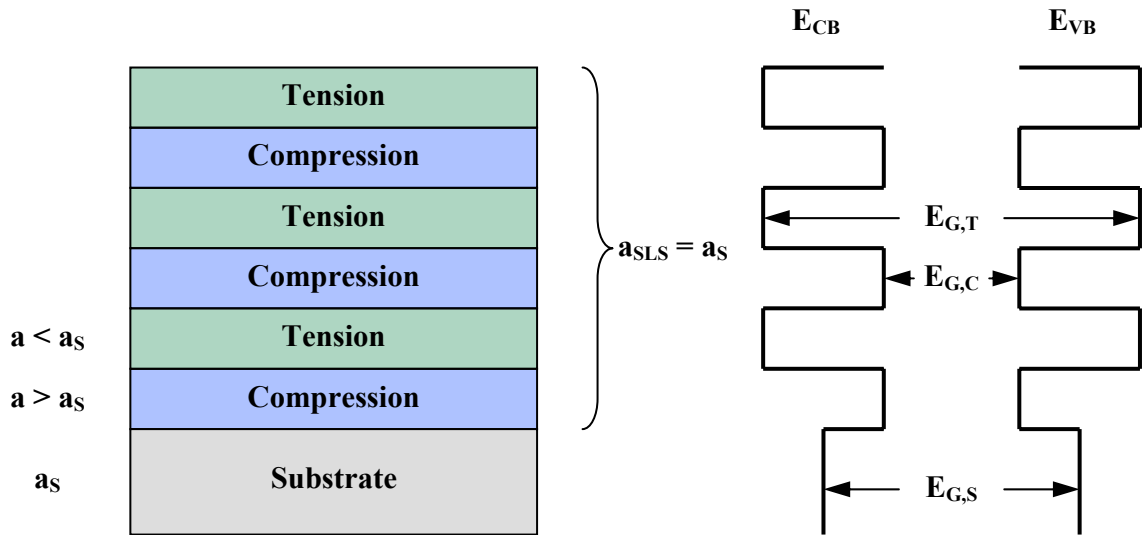


**Figure 4.1** Strained Layer Superlattice with Resulting Band Diagram

At this point, a clarification of terminology is in order due to occasional confusion found in the literature. A semiconductor superlattice is a periodic structure of alternating layers with different bandgaps, first proposed in 1969 by Esaki and Tsu.<sup>117</sup> Strained layer superlattices are a sub-class of these where the local strain in each layer has a significant effect on properties. An important feature of SLS's is that the barrier or wide band gap layer is sufficiently thin that the carrier wavefunctions are no longer confined and tunneling is observed. Multiple quantum wells (MQW) are very similar structures but differ in that the barriers are wide enough to confine carriers in the well.<sup>118</sup> We will see in chapter 9 that this distinction is important for carrier transport through the SLS structure. SLS's are further divided into two classes. In the first class, the average lattice constant does not equal the substrate lattice constant. The total SLS thickness is then limited by the critical layer thickness imposed by the mismatch of the average lattice constant. Binary-ternary systems are the classic example and have been demonstrated for GaAs-GaAsP<sup>71,119</sup> and GaAs-

InGaAs.<sup>120</sup> The second class is strained balanced<sup>121</sup> as previously described and has no fundamental total thickness limit.

#### 4.2 SURVEY OF INGAAS/GAASP STRUCTURES FOR PHOTOVOLTAICS

The use of  $\text{In}_x\text{Ga}_{1-x}\text{As}/\text{GaAs}_{1-y}\text{P}_y$  was first proposed for use in light emitting diodes by our laboratory in 1984.<sup>122</sup> Then in 1987, the same structure was proposed for solar cells in an analysis of the state of high efficiency photovoltaics at that time.<sup>123</sup> Lattice matching is reported for  $y = 2x$  for equal layer thickness and demonstrated for  $x = 0.1$  and  $y = 0.2$ . A pn-junction of the SLS is also reported for  $x=0.14$  and  $y = 0.28$  with  $V_{OC} = 0.85\text{V}$ . Spectral response is extended beyond GaAs to  $9200\text{\AA}$  corresponding to a bandgap of about  $1.35\text{eV}$ . To the best of the author's knowledge, the only other similar reported work in this area is InGaAs/GaAsP MQW structures by Barnham et al.<sup>124</sup> This group has reported extensive data and analysis for compositions around  $x = 0.17$  and  $y = 0.06$ . Carrier transport will be much different in these MQW structures, but there are many similarities that make this data useful when considering the SLS structure.

#### 4.3 ANALYSIS OF INGAAS/GAASP SLS FOR PV APPLICATIONS

Since this structure is considerably more complex than a simple junction of bulk material, several issues must be addressed both theoretically and for application to a real device. In particular, band structure, strain effects, quantum size effect, and carrier transport are radically different from a bulk film. The following analysis will indicate that significant bandgap reduction can be realized, but may fall short of the desired  $1\text{eV}$ . However, the addition of a small amount of N is expected to make up the difference. First, the

InGaAs/GaAsP SLS must be optimized to minimize the amount of N required, to avoid the onset of poor material quality. The requirements of each layer will first be discussed individually and then synergistically. Material constants and parameter values used for calculations in this document are tabulated in Appendix A.

#### 4.3.1 Bandgap Dependence on Strain, Temperature, and Composition

InGaAs is the layer responsible for bandgap reduction and photon absorption. For In compositions around 30% a bandgap of 1eV is expected for bulk films. However, strain in the thin film will modify this value. The effects of strain on energy levels in cubic semiconductors are well known.<sup>125,126</sup> Compressive biaxial strain in the InGaAs layer results in uniaxial expansion perpendicular to the layer, consistent with the Poisson ratio. The lattice in the layer is no longer cubic which splits and shifts the valence band at the  $k = 0$  degeneracy. For compressive strain, the bands shift away from the conduction band resulting in an increase in the bandgap, which has been observed experimentally.<sup>127,128</sup> Band structure around  $k = 0$  for compressive strain, zero strain, and tensile strain is given in Figure 4.2. The degeneracy that exists at zero strain (B) is split for both types of strain. For compressive strain(A), the valence band maxima is of heavy hole(HH) type. The light hole(LH) band shifts above the heavy hole band to form the valence band maxima under tensile strain(C). Split-off orbit (SO) band shift is included for completeness. Strain also introduces anisotropy in the in-plane hole effective masses as seen in the non-parabolic curvature in the bands.<sup>129</sup>

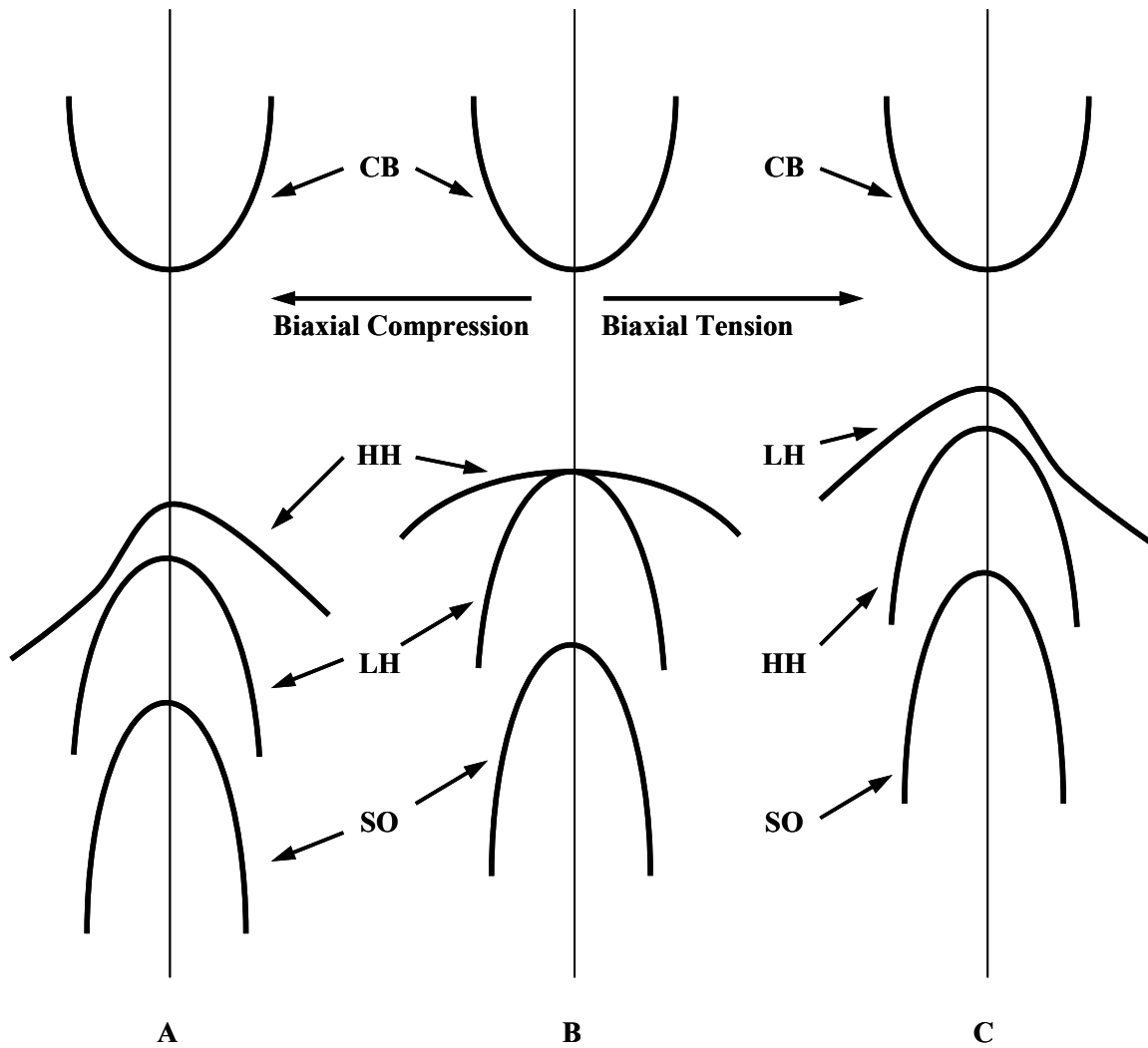


**Figure 4.2** Band Structure of GaAs under (A) Biaxial Compressive Strain, (B) Zero Strain, and (C) Biaxial Tensile Strain (CB=conduction band, HH=heavy hole band, LH=light hole band, SO=split-off band)(After Asai<sup>130</sup> and Bir<sup>129</sup>)

The shift of the light hole band,  $\Delta E_{lh}$ , and heavy hole band,  $\Delta E_{hh}$ , at  $k = 0$  is calculated relative to the conduction band by assuming a two-band model and neglecting the spin-orbit split off band as follows.<sup>130</sup>

$$\Delta E_{lh} = \left[ -2a \frac{C_{11} - C_{12}}{C_{11}} - b \frac{C_{11} + 2C_{12}}{C_{11}} \right] \epsilon \quad [4.3]$$

$$\Delta E_{hh} = \left[ -2a \frac{C_{11} - C_{12}}{C_{11}} + b \frac{C_{11} + 2C_{12}}{C_{11}} \right] \epsilon \quad [ 4.4 ]$$

a is the hydrostatic deformation potential,  $C_{ij}$  are the elastic stiffness coefficients, b is the shear deformation potential, and  $\epsilon$  is the biaxial strain. The hydrostatic deformation potential is calculated from

$$a = -\frac{1}{3}(C_{11} + 2C_{12}) \frac{\partial E_0}{\partial P} \quad [ 4.5 ]$$

where  $\partial E_0/\partial P$  is the hydrostatic pressure coefficient of the lowest energy gap. These values are not available over a wide range of ternary compositions, so they have been interpolated from readily available binary data. Strain increases in the layer with increasing indium composition, so the band shift also increases. This increase in bandgap is in competition with the reduction realized in a bulk film with increasing indium composition. The energy change relative to unstrained GaAs is plotted for light and heavy hole bands in compressively strained InGaAs in Figure 4.3, along with the bandgap reduction with increasing indium in a bulk film at 300K. The resulting effective bandgap shift (conduction band to light hole band) is also plotted for comparison. For  $\text{In}_{0.3}\text{Ga}_{0.7}\text{As}$ , the effective bandgap is 1.11eV, an increase of  $\sim 110\text{meV}$  over the unstrained value. Clearly, if InGaAs is to be used as the active layer, an In composition higher than 30% would be required to approach a bandgap of 1eV. However, increasing In composition will further decrease the critical layer thickness and increase the film strain. This will, in turn, require thicker barriers are higher P concentrations to balance the strain. Therefore, 30% is a practical initial target for In composition.

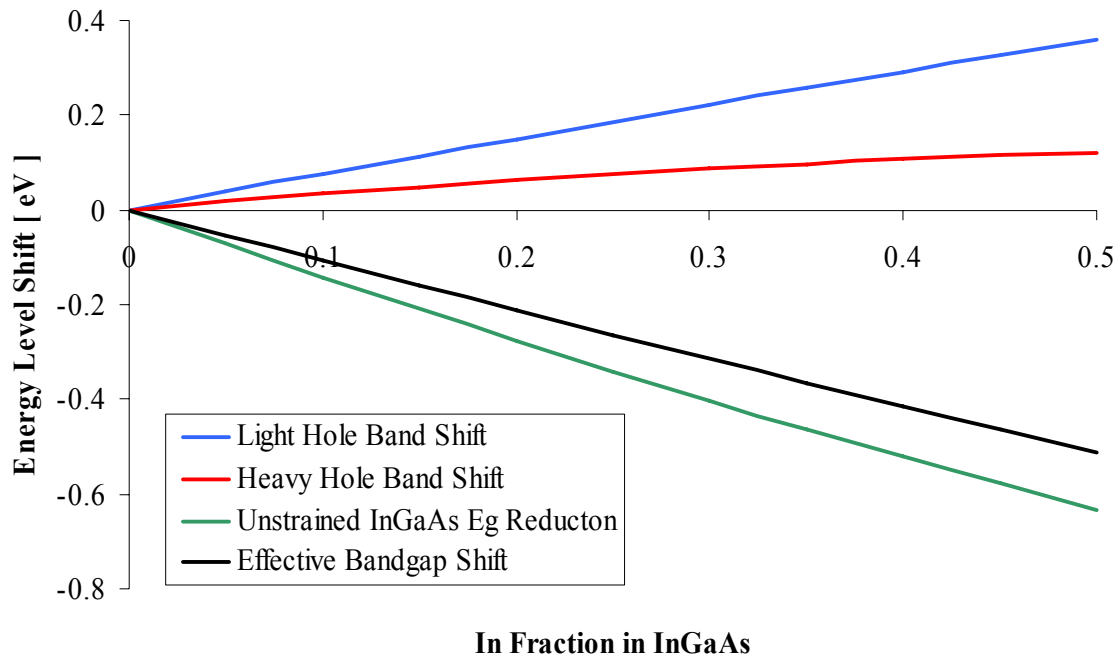


**Figure 4.3** Compressive Strain Induced Light(Blue) and Heavy(Red) Hole Band Shift Compared with Unstrained InGaAs Bandgap Dependence(Green) on In Fraction (300K). Combined Effective Bandgap Shift is also Plotted in Black

GaAsP is intended only to balance strain, but the effect of inserting this high bandgap material into the SLS is critical. Biaxial tension causes a uniaxial contraction perpendicular to the film. As with compression, the valance band is split, but the shift is toward the conduction band, reducing the bandgap. There is not a specific target for the GaAsP bandgap as it is not an active layer, but lower is better for carrier escape. In a multijunction cell, the top junction will filter any higher energy photons that match the higher bandgap of GaAsP. Furthermore, at higher P compositions GaAsP becomes indirect. However, it is important to know the bandgap of this layer for further analysis of the structure. The band energies are calculated in the same manner as described for InGaAs. Figure 4.4 shows the increase in bandgap of a bulk film with increasing P compared to the energy shift of the hole bands toward the conduction band due to tensile strain. Since

GaAsP has an direct-indirect transition around 50% P, both  $E^\Gamma$  and  $E^X$  transitions are plotted. Effective bandgap shift is also plotted for comparison.

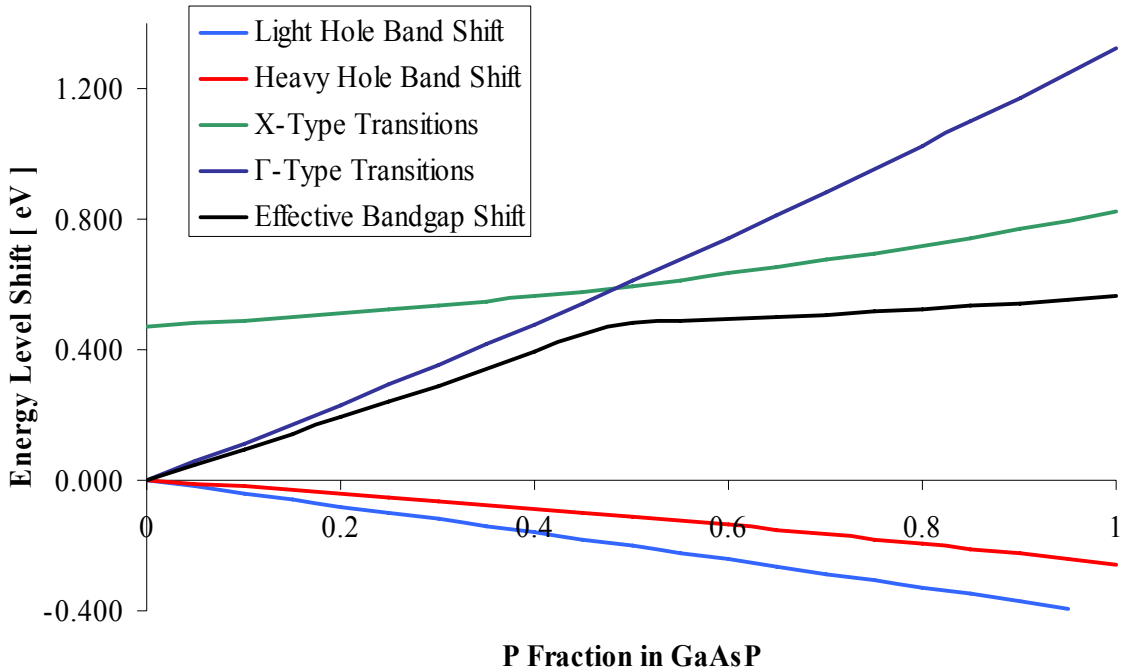


**Figure 4.4** Tensile Strain Induced Light(Light Blue) and Heavy(Red) Hole Band Shift Compared with Unstrained GaAsP Bandgap Dependence(X-Green,  $\Gamma$ -Dark Blue) on P Fraction (300K). Combined Effective Bandgap is Plotted in Black

While developing the calculations for strain effects in spreadsheet format, it proved useful to generalize the evaluation for any composition and any temperature. Simply entering the composition of each film and the temperature returns the bandgap dependence on temperature, composition, and strain. This proved to be a useful tool for theoretical analysis of the structure. The change in bandgap with temperature is calculated with the Varshni model,<sup>131</sup>

$$E_g(T) = E_g(0) - \frac{\alpha T^2}{T + \beta} \quad [4.6]$$

where  $E_g(0)$  is the bandgap at 0K, and  $\alpha$  and  $\beta$  are fitting parameters chosen to fit experimental data. Compositional bandgap changes are linear interpolations of the binary end points, fitted to experimental data with a bowing parameter,  $b$ .

$$E_g(x) = xE_1 + (1-x)E_2 - bx(1-x) \quad [4.7]$$

$E_1$  and  $E_2$  are the bandgaps of the binaries calculated for a given temperature, and  $x$  is the ternary composition. The bowing parameter used for calculation is  $0.375^{132}$  for InGaAs and  $0.21^{133}$  for GaAsP.

#### 4.3.2 Critical Layer Thickness for InGaAs and GaAsP

In addition to an analysis of the individual layers, the SLS must be treated as a complete structure. First, we will consider the limitations imposed by the critical layer thickness (CLT). The critical layer thickness predicted by the Matthews-Blakeslee model is plotted for In composition up to 50% in Figure 4.5. Even for relatively small In fractions, the CLT is well within the range where quantum size effects should be considered. Consider the alternating high and low bandgaps along the growth direction. Carriers experience a series of energy wells and barriers and will become trapped in the lower energy wells. This is true for both conduction and valence bands, as a type 1 band alignment is expected. The depth of the wells depends on the composition of both the barrier and the well and on the band offset. To use this structure in a solar cell, the photo-generated carriers must be extracted from the wells to contribute to conduction.

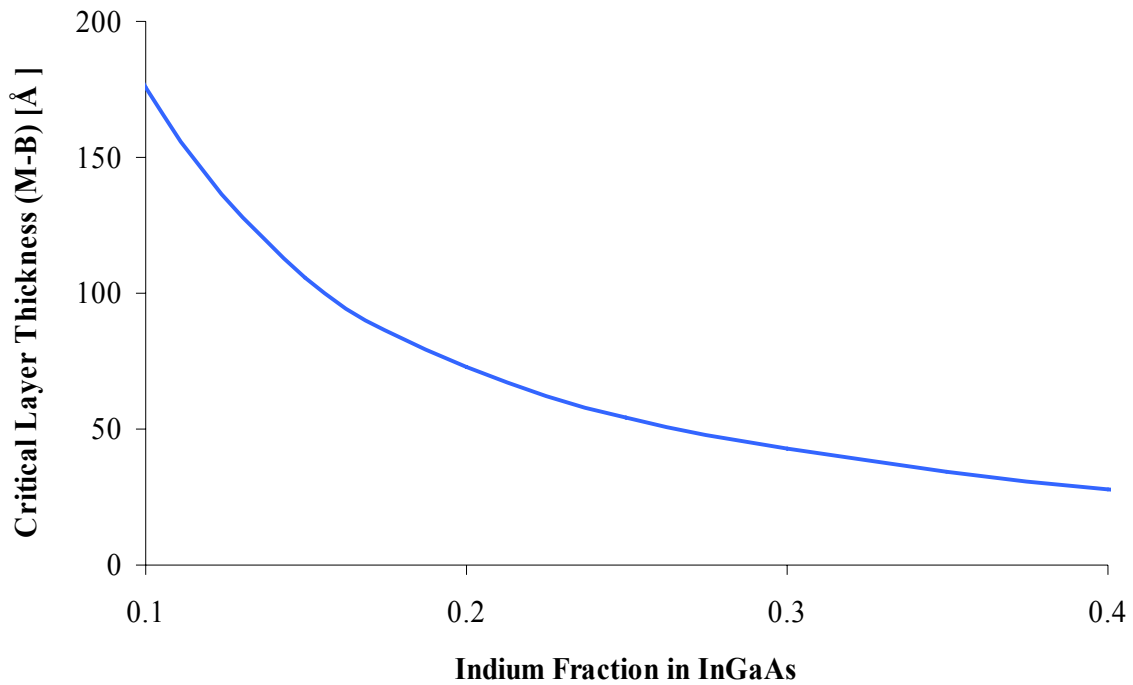


**Figure 4.5** Critical Layer Thickness Indium Fraction Dependence for InGaAs Strained to GaAs (After Matthews-Blakeslee)

Previous work with this structure, discussed in section 4.2, is limited to relatively low indium and phosphorous compositions (less than 20% for each) and thick wells and barriers. As expected, the difference in the bandgap of InGaAs and GaAsP,  $E_{G,C} - E_{G,T}$  in Figure 4.1 is relatively small, and the wells are fairly shallow. Carriers can escape the wells by gaining thermal energy in a process called thermionic emission. This is characteristic of multiple quantum well solar cells. From our analysis of strain induced bandgap shift of InGaAs, significantly higher In compositions are required compared to previous reports. This will result in deeper wells, significantly reducing thermionic emission and effectively impeding carrier transport through the material. Barnham, et al utilizes relatively thick layers of GaAsP, with P around 6%, to balance the strain in InGaAs/GaAsP MQW structures.<sup>124</sup> This is important if thermionic emission is the primary mechanism of carrier

transport, as the barrier height should be as low as possible to promote carrier escape. The proposed alternative method for this structure is to make the GaAsP layers very thin so the carriers are no longer confined and tunnel through the barrier. To realize this, very high P compositions must be used to balance the strain. In the limiting case, the barrier layers would be GaP, but this could be very difficult to achieve while maintaining while maintaining suitable growth conditions for the rest of the structure. A high P concentration will also form large barriers (i.e. deeper wells) making carrier escape via thermionic emission even less probable. A more detailed analysis of carrier transport through the structure is reserved for chapter 9. CLT, plotted in Figure 4.6 after Matthews-Blakeslee, will be reduced significantly by increased P concentration, but should not be problematic as even thinner barriers are desired.

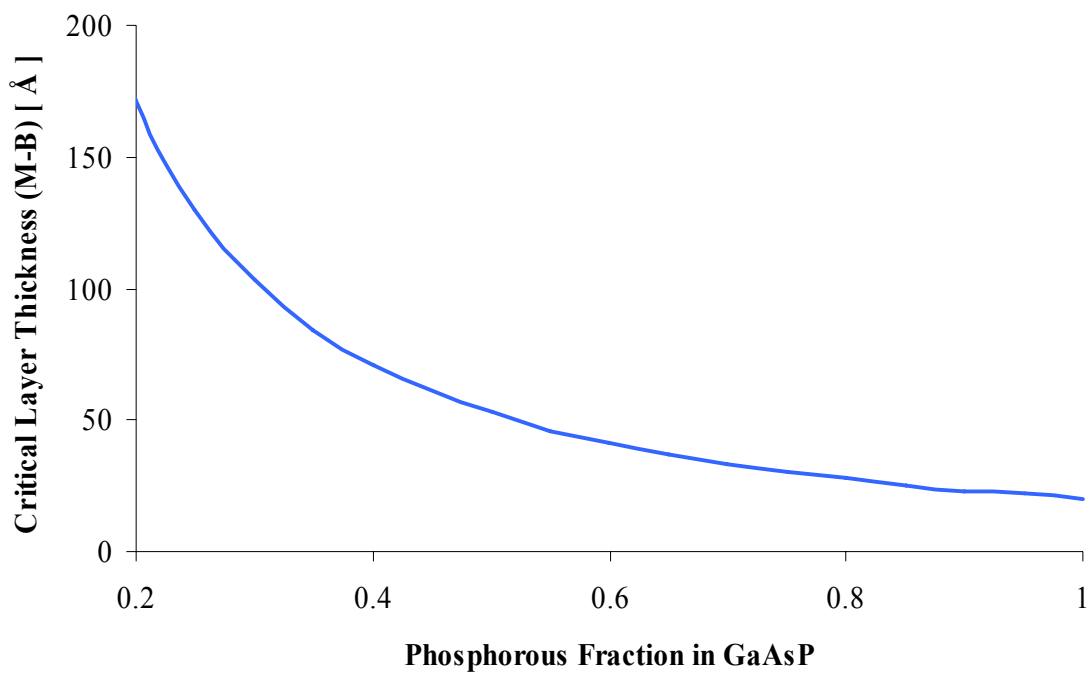


**Figure 4.6** Critical Layer Thickness Phosphorous Fraction Dependence for GaAsP Strained to GaAs (After Matthews-Blakeslee)

### 4.3.3 Quantum Size Effect

The thin layers of the proposed SLS will give rise to quantum size effects. Recall from section 2.2.2 that the conduction and valence bands in a bulk crystalline solid are essentially continuous. Reducing layer thickness to approximately the de Broglie wavelength of electrons in the material or the exciton Bohr radius ( $\sim 10\text{-}100\text{nm}$ ), splits the bands into discrete levels, effectively increasing the bandgap. For the InGaAs wells, this introduces yet another competing parameter for bandgap reduction that must be overcome. For demonstration, the resulting band structure of a  $\text{In}_{0.15}\text{Ga}_{0.85}\text{As}/\text{GaAs}_{0.7}\text{P}_{0.3}$  SLS with  $100\text{\AA}$  wells and barriers is shown schematically in Figure 4.7. The total band offset,  $\Delta E_G$ , between  $\text{In}_{0.15}\text{Ga}_{0.85}\text{As}$  and  $\text{GaAs}_{0.7}\text{P}_{0.3}$  is  $0.452\text{eV}$ . For this structure,  $\Delta E_G$  is distributed 70% or  $0.316\text{eV}$  to the valence band and 30% or  $0.136\text{eV}$  to the conduction band.<sup>134</sup>

Discrete energy levels arising from the quantum size effect in the valence and conduction bands are indicated by  $E_{V,i}$  and  $E_{C,i}$ , respectively. The resulting effective bandgap in the well regions,  $1.3\text{eV}$ , is from the first energy level in the valence band,  $E_{V,1}$ , to the first level in the conduction band,  $E_{C,1}$ . Well depth is greatly exaggerated to show discrete energy levels.

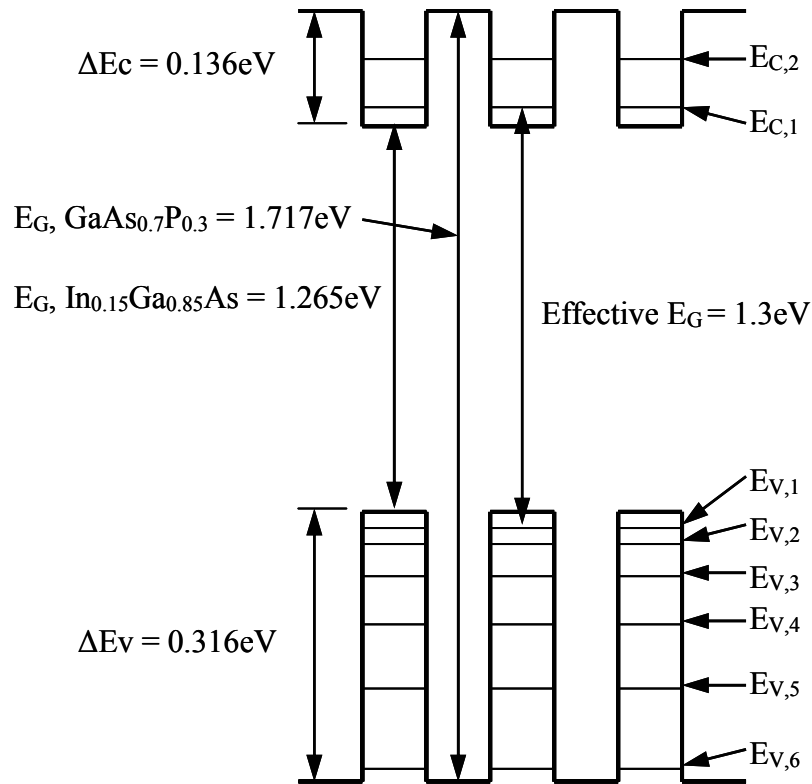


**Figure 4.7** Band Structure of an  $\text{In}_{0.15}\text{Ga}_{0.85}\text{As}/\text{GaAs}_{0.7}\text{P}_{0.3}$  SLS Demonstrating Quantum Size Effect (Well and Barriers Layers are  $100\text{\AA}$ )

Effective band gap is calculated by locating the first discrete energy level in the conduction and valence bands. These discrete levels are calculated by solving the Schrödinger equation, analogous to finding discrete energy levels in an individual atom. In this case we are interested only in size reduction along one dimension, the growth direction. The solution takes the form of the well known Kronig-Penney equation<sup>135</sup> and can be applied to periodic structures created artificially, including SLS's. However, the KP equation is tedious to solve and sometimes fails to give the correct solution for certain situations.<sup>136</sup> Szmulowicz has presented an alternative method to analyze the KP model which simplifies numerical calculation and corrects the special case failures.<sup>137</sup> We know

that the effective mass of carriers in the barrier will differ from the effective mass in the wells. This is incorporated into the model via the effective mass approximation at an interface.<sup>138</sup> Ultimately, the solution is the determinant,  $D_{SZ}$ , of a 2 x 2 matrix derived by Szmulowicz,

$$D_{SZ} = \left[ \tan\left(k_A a + \frac{qd}{2}\right) + \frac{m_A k_B}{m_B k_A} \tan(k_B b) \right] \left[ \tan\left(k_A a - \frac{qd}{2}\right) + m_B k_A \frac{\tan(k_B b)}{m_A k_B} \right] \\ + \left[ \tan\left(k_A a - \frac{qd}{2}\right) + \frac{m_A k_B}{m_B k_A} \tan(k_B b) \right] \left[ \tan\left(k_A a + \frac{qd}{2}\right) + m_B k_A \frac{\tan(k_B b)}{m_A k_B} \right] = 0 \quad [4.8]$$

where<sup>136</sup>

$$k_A = \sqrt{\frac{2m_A(E - V_0)}{\hbar^2}} \quad k_B = \sqrt{\frac{2m_B E}{\hbar^2}} \quad [4.9]$$

and  $a$  and  $b$  are half-widths of the barrier and well respectively,  $d = 2a + 2b$ ,  $m_A$  is the effective mass in the barrier,  $m_B$  is the effective mass the well, and  $V_0$  is the well depth. Discrete energy levels are typically found by plotting  $D_{SZ}$  vs.  $E$ , but the discontinuities arising from the tangents in equation 4.8 can be cleared by multiplying through by cosines.  $D_{SZ}(\cos^2 k_B b)$  vs.  $E$  is plotted in Figure 4.8 for  $\text{In}_{0.15}\text{Ga}_{0.85}\text{As}/\text{GaAs}_{0.7}\text{P}_{0.3}$  and equal well and barrier thickness of  $100\text{\AA}$ , for both the conduction and valence bands. Each zero indicates the position of an energy state relative to the bottom(top) of the well for the conduction(valence) band. (See Figure 4.7) The discontinuity in the CB curve means that there are only two confined states in the well for these conditions. The bandgap change only depends on the first level of the wells in each band. Finding the first level is automated by iterative calculation for a range of  $E$  values and using a string of code to search the data for the first zero. Finally, effective band gap is calculated as  $E_{G,\text{InGaAs}} + E_{V,1} + E_{C,1}$ .

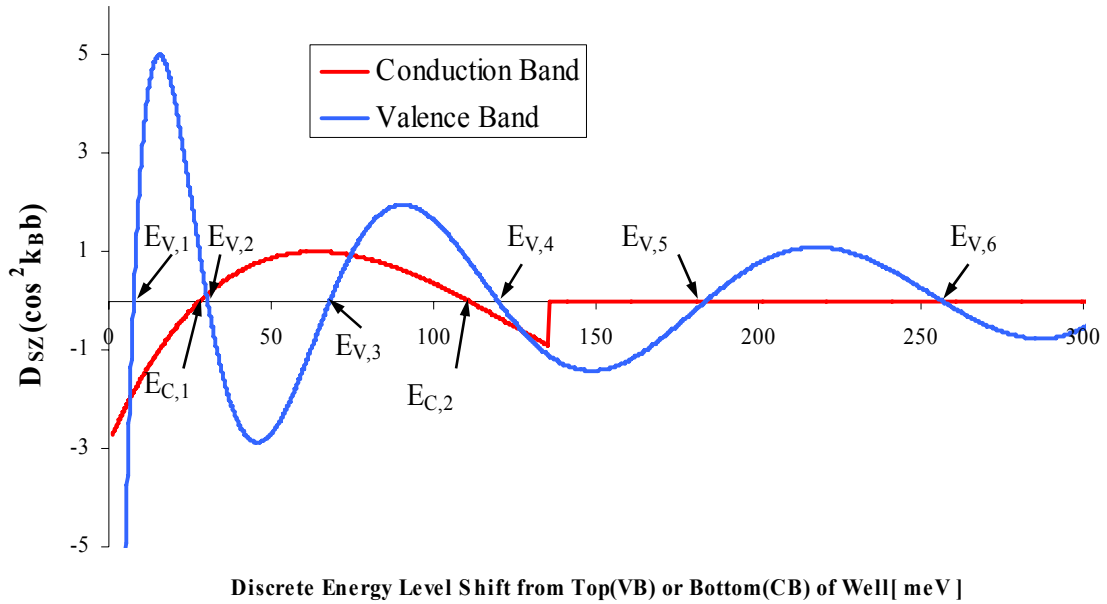


**Figure 4.8** Graphical Solution of the Schrödinger Equation to Find Quantized Energy States in the InGaAs Quantum Well (Each zero represents a discrete energy level formed in the well in the valence band (Blue) and conduction band (Red))

Temperature dependence of the effective mass is significant and can not be ignored. In the calculation above, this dependence is represented by substituting the energy gap change with temperature into a three level  $\mathbf{k}\cdot\mathbf{p}$  formula reported by Adachi.<sup>43</sup>

$$\frac{m_0}{m_i}(T) = 1 + \frac{P^3}{3} \left[ \frac{2}{E_g(T)} + \frac{1}{E_0(T) + \Delta_0(T)} \right] \quad [ 4.10 ]$$

$m_i$  is the carrier effective mass,  $E_g(T)$  is given by equation 4.6 and the light hole band transition  $E_0(T) + \Delta_0(T)$  follows the same dependence with different fitting parameters. Equation 4.10 was applied to binary compounds and ternary values were interpolated from the binary effective masses.

Also important to the calculation is the assignment of the total band offset to the valence and conduction bands. This determines the depth of the wells in each band,  $V_0$ , in

equation 4.9. As stated previously for InGaAs/GaAsP, 70% of the offset is assigned to the valence band and 30% to the conduction band after the convincing report by Froberg, et al for InGaAs/GaAsP QW modulators.<sup>134</sup> For InGaAsN, nearly all of the bandgap reduction occurs in the conduction band for N addition.<sup>139</sup> It is then a reasonable approximation to assign the same offset to the valence band for both InGaAs and InGaAsN and to assign the additional reduction due to N to the conduction band.<sup>140</sup>

This calculation was added to the spreadsheet calculations for temperature, strain, and composition dependence so all effects are updated simultaneously. It is then convenient to plot the combined effect on the bandgap vs. the well width. Unstrained and strained bandgaps of  $\text{In}_{0.3}\text{Ga}_{0.7}\text{As}$  are plotted in Figure 4.9 for comparison to the combined effective bandgap resulting from strain and quantum size effect.

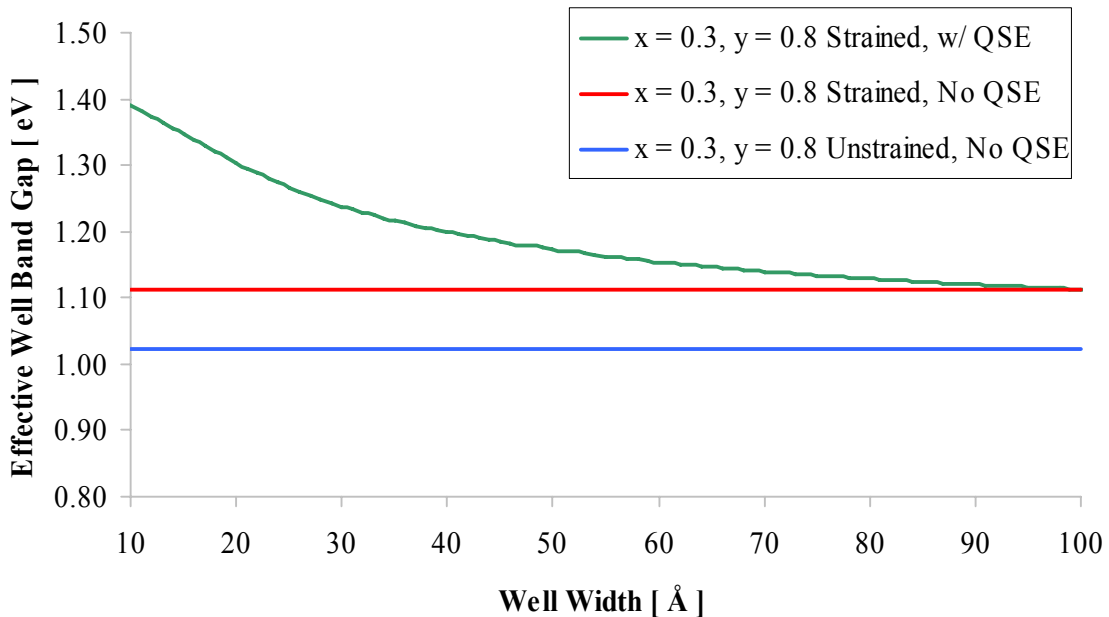


**Figure 4.9** Combined Effective  $\text{In}_{0.3}\text{Ga}_{0.7}\text{As}$  Bandgap (Green) for a Range of Well Widths, Unstrained (Blue) and Strained (Red) Bandgaps are Shown without Quantum Size Effect for Comparison (Barriers are  $\text{GaAs}_{0.2}\text{P}_{0.8}$ )

From Figure 4.10, it is predicted that 1eV can not be attained with 30% indium composition. However, if the calculations are repeated to include the effect of adding a small amount of N to form  $\text{In}_{0.3}\text{Ga}_{0.7}\text{As}_{1-z}\text{N}_z/\text{GaAs}_{0.2}\text{P}_{0.8}$ , 1eV can be attained within the CLT. While this model is not exhaustive, it accounts for expected first order effects and provides a solid framework for analysis of the structure. Comparisons will be made to the photoluminescence and spectral response data in chapter 9.

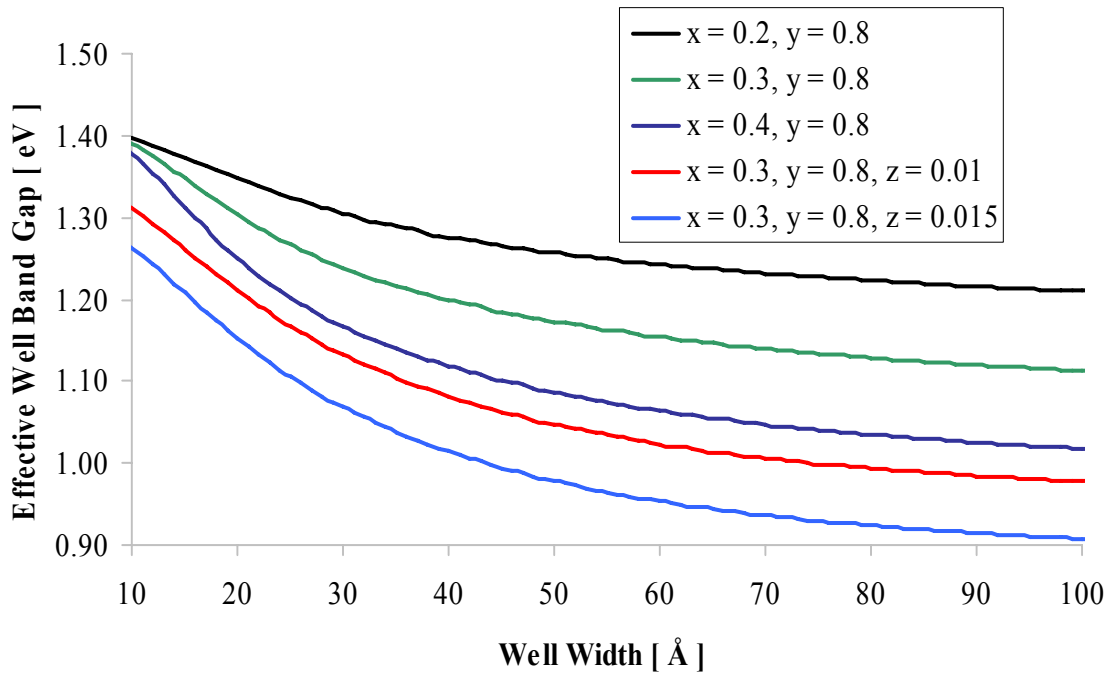


**Figure 4.10** Quantum Size Effect for InGaAs Well Thickness (Effects of Strain, Composition, and Temperature also Included in the Calculation)

#### 4.3.4 p-i-n Device

The SLS structure will be inserted as the i region in a p-i-n diode. A p-i-n diode is very similar to a p-n diode except for an intrinsic layer between the p and n regions. The

built-in bias is the same for p-i-n and p-n structures for equal doping levels, but the field is extended over the undoped intrinsic material. Electric field variation across a GaAs p-n junction, with doping levels used in this research,  $N_A = 2 \times 10^{18} \text{cm}^{-3}$  and  $N_D = 1.1 \times 10^{17} \text{cm}^{-3}$  is plotted in Figure 4.11 at 300K. Depletion width in the n-layer,  $x_n = 139 \text{nm}$ , and in the p-layer,  $x_p = 7.62 \text{nm}$ , is calculated from

$$x_n = \frac{1}{N_D} \sqrt{\frac{2 \epsilon_s V_{bi}}{q \left( \frac{1}{N_A} + \frac{1}{N_D} \right)}} \quad x_p = \frac{1}{N_A} \sqrt{\frac{2 \epsilon_s V_{bi}}{q \left( \frac{1}{N_A} + \frac{1}{N_D} \right)}} \quad [ 4.11 ]$$

where  $\epsilon_s$  is the permittivity of the semiconductor, and  $V_{bi}$  is the built-in voltage,  $\sim 1.3 \text{V}$ .

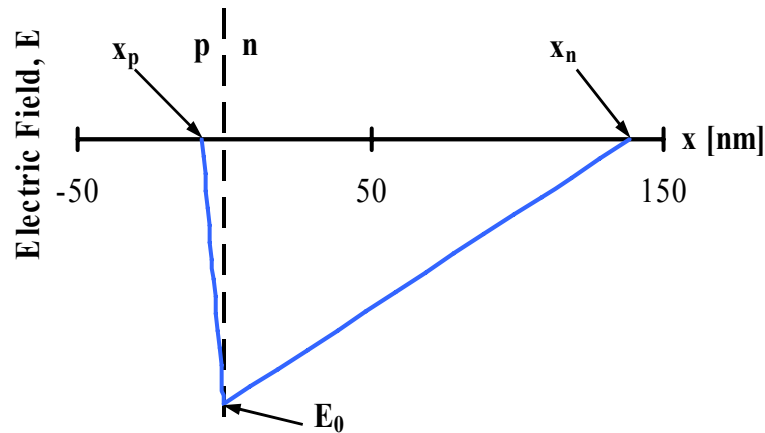


**Figure 4.11** Electric Field Across a GaAs p-n Junction ( $N_A = 2 \times 10^{18}$ ,  $N_D = 1.1 \times 10^{17}$ ,  $x_p = 7.62 \text{nm}$ ,  $x_n = 139 \text{nm}$ ,  $E_0 = 1.9 \times 10^5 \text{ V/cm}$ )

Electric field variation across the junction is calculated in n and p regions by

$$E_n(x) = \frac{qN_D}{\epsilon_n}(x - x_n) \quad E_p(x) = -\frac{qN_A}{\epsilon_p}(x - x_p) \quad [ 4.12 ]$$

where  $\epsilon_i$  is the permittivity of n and p material. The maximum value for field strength,  $E_0$ , across the depletion region occurs at the junction and is  $\sim 2 \times 10^5$  V/cm for the specified doping level. Built-in voltage is determined from

$$V_{bi} = \frac{k_B T}{q} \ln \left( \frac{N_D N_A}{n_i^2} \right) \quad [ 4.13 ]$$

where  $k_B$  is Boltzmann's constant and  $n_i$  is the intrinsic carrier concentration. Intrinsic carrier concentration is computed from

$$n_i^2 = np = N_C N_V e^{-\left(\frac{E_G}{k_B T}\right)} \quad [ 4.14 ]$$

where  $N_C$  and  $N_V$  are the CB and VB effective density of states calculated from

$$N_C = 2 \left( \frac{m_c^* k_B T}{2\pi\hbar^2} \right)^{\frac{3}{2}} \quad N_V = 2 \left( \frac{m_v^* k_B T}{2\pi\hbar^2} \right)^{\frac{3}{2}} \quad [ 4.15 ]$$

where  $m_i^*$  is the carrier effective mass. Table 4.1 summarizes the calculated values used for determining the electric field. In real devices, junctions are not perfectly abrupt which serves to reduce the field and built-in voltage from the ideal calculated value.

**Table 4.1** Parameters for Electric Field Calculation

Parameter	Calculated Value
p-doping Level [ $\text{cm}^{-3}$ ], $N_A$	$2 \times 10^{18}$
n-doping Level [ $\text{cm}^{-3}$ ], $N_D$	$1.1 \times 10^{17}$
Permittivity of GaAs [ F/m ], $\epsilon_S$	13.2
Built-In Voltage [ V ], $V_{bi}$	1.35
p-type Depletion Width [ nm ], $x_p$	7.6
n-type Depletion Width [ nm ], $x_n$	138
Effective Valence Band Density of States [ $\text{cm}^{-3}$ ], $N_V$	$8.1 \times 10^{18}$
Effective Conduction Band Density of States [ $\text{cm}^{-3}$ ], $N_C$	$4.0 \times 10^{17}$
Intrinsic Carrier Concentration [ $\text{cm}^{-3}$ ], $n_i$	$2.1 \times 10^6$
Hole Effective Mass [ kg ]	$0.470m_0$
Electron Effective Mass [ kg ]	$0.063m_0$

For a p-i-n diode, the field distribution across the p and n regions is analogous to Figure 4.11. However, the influence of the i-layer is to extend the electric field over a wider region, as shown in Figure 4.12. For a  $0.3\mu\text{m}$  GaAs i-layer, the maximum field strength is  $\sim 43\text{kV/cm}$ . III-V semiconductors grown by OMVPE frequently have some unintentional background doping, therefore the i-layer may not be truly intrinsic. This structure is more accurately called a p- $\pi$ -n or p- $\nu$ -n diode, where  $\pi$  represents light p-type doping and  $\nu$  represents light n-type doping,<sup>20</sup> but p-i-n is frequently used regardless of the actual doping level. For GaAs and related alloys, the background dopant is often carbon, originating from decomposition of precursors, which is an acceptor. The dashed lines indicate the change in



Some reduction in carrier lifetime is expected even for modest N concentrations and the p-i-n approach can ameliorate this to some degree. Second and most important, the field will assist carriers to traverse the barriers created by the GaAsP layers. Built-in field across the i-layer will bend the conduction and valence bands as shown schematically in Figure 4.11. Carriers can escape the wells either by thermalizing to the continuum states outside the wells or by tunneling through the barrier. Note that the bending induces an effective decrease in the barrier height which increase the probability of escape by both mechanisms. Carrier transport through the SLS structure is critical for device performance and will be discussed in much greater detail in chapter 9, in terms of specific devices.

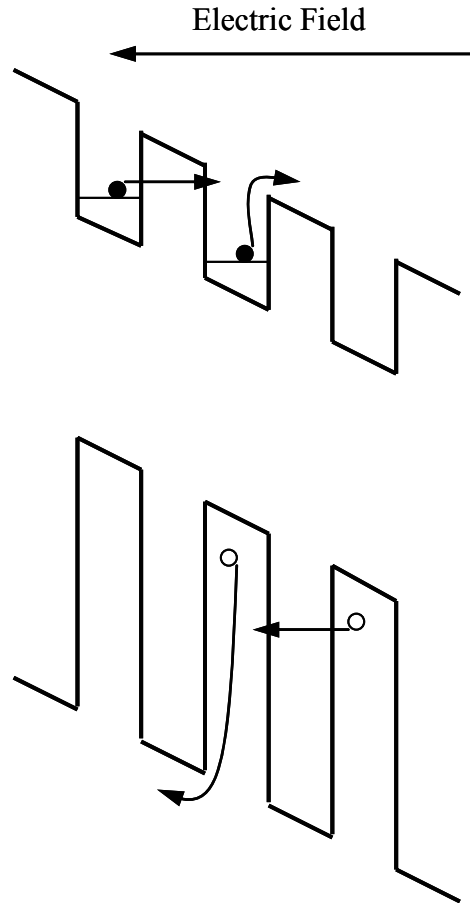


**Figure 4.13** Band Bending and Carrier Escape in the Presence of Built-In Electric Field Across i-layer( open circles = holes, solid circles = electrons)

While the i-layer is useful for carrier transport, there are some drawbacks to this approach that must be considered. If the layer is undoped, conductivity may be poor, contributing to series resistance. Also, the population of holes and electrons will be similar, increasing the probability of loss via recombination. If charged carriers build up in the wells, the field may be screened within the first few periods rather than extending across the structure. The first two problems may be subdued by introducing a low doping level, but there must be a balance so the field is not screened by the dopant carriers. Build-up of carriers in the wells can be prevented by efficient extraction which reinforces the use of thin

barrier layers. Various doping levels in the i-region have been investigated and will be discussed in terms of device performance.

## 5 OMVPE GROWTH

All semiconductor films presented in this research were deposited or “grown” via Organometallic Vapor Phase Epitaxy or OMVPE. Various nomenclature is found in the literature, so it warrants clarification. This process is also known as Metal-Organic Chemical Vapor Deposition (MOCVD) or other iterations such as OMCVD and MOVPE. Organometallic(OM) is the more traditional nomenclature from chemical sciences. CVD is a general deposition process and VPE is one type of CVD. CVD does not indicate any details of the nature of the deposited film while VPE indicates single crystals of material are deposited epitaxially, hence OMVPE will be used. Epitaxy is the general process of depositing thin layers of single crystal material on a single crystal substrate such that there is a crystallographic relationship between the two. The structure of the substrate is replicated in the film, including defects, so substrate quality is critical. In OMVPE, chemicals are delivered in the gas phase to a heated substrate. Heat energy activates the chemical reaction at the surface resulting in epitaxial films. Relatively cold gases reacting at a hot surface is characteristic of VPE. Other epitaxial methods such as liquid phase epitaxy (LPE) and molecular beam epitaxy (MBE) supply heated chemicals to a cold surface for crystallization. For OMVPE, chemicals are delivered to the substrate via a carrier gas such as hydrogen or nitrogen. The reaction is enclosed in a sealed reactor to prevent reaction with surroundings. Contaminants from the air, especially oxygen, can interfere with the crystal growth process. Containment is also important for safety as many of the chemicals are highly flammable and toxic. The reactor also allows pressure to be adjusted via a pump. OMVPE requires a high degree of parameter control compared to other processes, but the primary controls are temperature, pressure, and flux of reactant chemicals through the reactor. All three

parameters must be carefully chosen based on an understanding of the growth mechanism. Crystal growth can be characterized by rate limiting processes; thermodynamic driving force, kinetics, and mass transport. Low temperature and low pressure favor growth limited by kinetics, such as the rate of precursor reaction at the surface. Higher temperature or pressure leads to mass transport limited growth, where movement of precursors through the thermal boundary layer is slower than the reaction rate. For higher temperatures, thermodynamic driving force could limit the reaction via evaporation of precursor elements. Mass transport limited growth produced the highest quality films in this research effort. The general theory of how an atom in the gas phase is incorporated into a semiconductor solid is well known.<sup>143,144</sup> The growing crystal surface consists of atomically flat layers separated by steps. Each step may have some kinks where precursor atoms can be incorporated, advancing the layer across the surface. New layers are continuously nucleated on existing layers to sustain this two dimensional growth mechanism. Various factors can interfere with this process, possibly resulting in an excess of undesired three dimensional growth. The thermodynamic and kinetic processes of OMVPE are highly complex and still not completely understood. However, a well known text by Stringfellow<sup>145</sup> offers a detailed discussion of the wide array of topics relevant to this type of deposition.

## 5.1 ORGANOMETALLIC PRECURSORS

Many of the elements required to form compound semiconductors are metals such as Ga, In, and Al. Organometallic precursors provide a means of delivering metals in the gas phase. An OM molecule typically consists of a central metal atom surrounded by organic ligands or radicals such as -methyl, -ethyl, and -butyl groups. The number of groups is

indicated by the prefix; bi or tri for two or three respectively. Trimethylgallium, for example, is a gallium atom with three attached –methyl groups. These precursors may be liquid or solid, but liquid is preferred for better repeatability. High vapor pressure is indicated so the vapor above the liquid or solid can be collected by the carrier gas and delivered to the reactor. Molecules approaching the heated substrate undergo pyrolysis where the radicals break away and the metal atom is adsorbed onto the growing crystal surface. This process can be very complex and sometimes imperfect in that some of the radicals are incorporated into the film or deleteriously interact with the surface. Frequently, several precursors are delivered to the reactor simultaneously, and may react in the gas phase before delivery to the substrate. Gas-phase reactions can deplete source atoms, create particulates, or form undesirable complexes which can interfere with growth or become incorporated into the film. In this situation, the precursors must be delivered unmixed until just before impingement on the substrate. Non-organometallic precursors can also be used with OM precursors. These are usually gaseous chemicals that can be injected directly into the system.

## 5.2 OMVPE GROWTH EQUIPMENT

In order to realize the OMVPE process, specialized equipment is employed to create the proper reaction environment. For this work, the complete system is a combination of standard commercially available equipment and custom designs. Figure 5.1 is a schematic of the basic components of the OMVPE system. In practice, there are many auxiliary components not shown here and there may be multiples of some components as described in the next few sections.

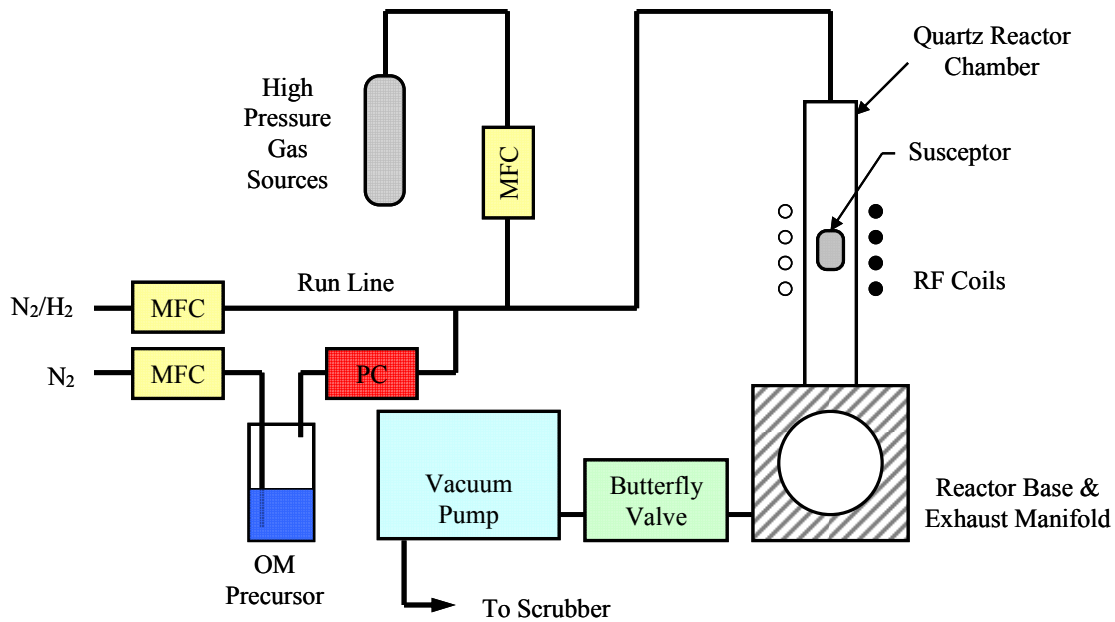


**Figure 5.1** Basic Components of an OMVPE Growth System (*MFC = Mass Flow Controller, PC = Pressure Controller*)

### 5.2.1 Precursor Sources and Delivery

Carrier gas and precursor delivery are realized via a commercial computer controlled system from semiconductor equipment manufacturer, Thomas Swan.<sup>146</sup> Device structures almost always require several layers of different materials. Precursor composition within the gas flow to the reactor is altered to form each material. The interface between layers typically must be sharp, within very few atomic layers, to achieve desired performance. Run/Vent manifolds, shown schematically in Figure 5.2, are used to ensure smooth crystal growth and sharp interfaces. An inert gas, such as nitrogen, flows through both lines at all times and serves several functions. The Run line goes to the reactor and the Vent line bypasses the reactor to an exhaust manifold. A block of valves directs precursor gas flows to either the Run or Vent. When the reactor requires a new precursor flow, it is first

introduced to the Vent line so it does not affect the reactor pressure or gas composition as it stabilizes. Both Run and Vent lines are held at the same pressure, equal to the reactor pressure. So when a precursor flow is switched to the Run line, no large pressure pulses are created that can interfere with crystal growth or interface sharpness. A differential pressure gauge is used to detect pressure differences between the two lines. This reading is sent to a control circuit that automatically increases or decreases nitrogen flow in the Vent line to balance the pressure. This system is adequate for correcting small pressure fluctuations but can not react fast enough when a large flow is switched to or from the Run line. Two make-up lines are available to carry nitrogen to the Run/Vent lines. One make-up line goes to the Vent and one to the Run line. Consider that before a switching event, the pressures are balanced between the Run and Vent lines and the flows are constant. When a precursor is switched from the Vent line to the Run line or vice versa, both make-up lines also switch simultaneously to maintain a constant flow in the Run/Vent lines so there is essentially no change in the flow to cause a pressure fluctuation. For the proposed solar cell, the InGaAs/GaAsP SLS is grown by alternating In and P flux every few seconds to form each layer. During this part of growth, one make-up line balances the P flux and one balances the In flux. These measures provide a smooth transition between materials, but are still not adequate for producing sharp interfaces. When switching precursor composition, the old composition needs to be swept out of the reactor quickly so there is little overlap with the new composition. Otherwise, an additional undesired layer may be formed. The block of Run/Vent switching valves is designed for rapid switching and low dead volume. Dead volume in the lines or valves promotes mixing of the two successive compositions. The system is equipped with two Run/Vent manifolds; one for column III and one for column V

precursors. Multiple manifolds help separate chemicals that may have gas-phase reactions prior to reaching the reactor.

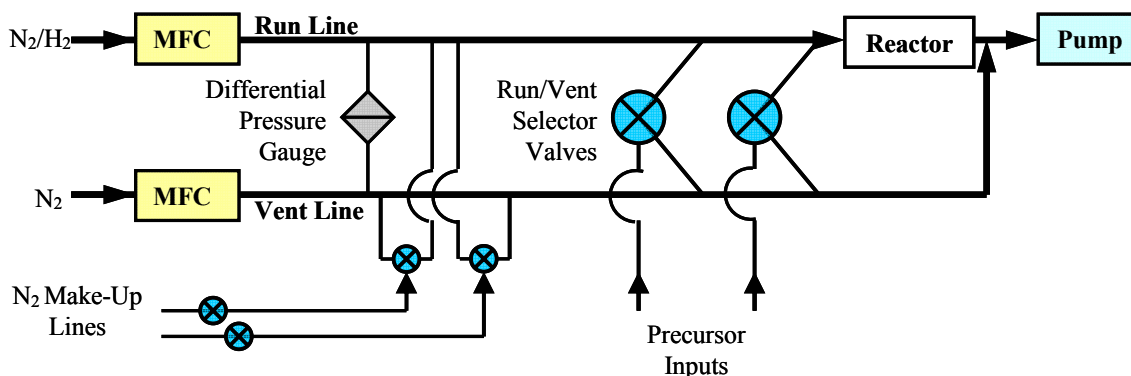


**Figure 5.2** Run/Vent Manifold Schematic

Precursors for this work are either organometallic or gaseous. Gaseous sources come in high pressure bottles and are available with high purity. Pressure is regulated to an appropriate level for direct injection to the manifold delivery system. A large quantity of nitrogen gas is used as both a carrier gas and a continuous purge when the system is idle. Two large tanks (~4600 cu.ft. ea.) of liquid nitrogen (LN<sub>2</sub>), which inherently has high purity, meet this demand.

Organometallic precursors come in stainless steel canisters called bubblers. Seven bubblers can be accommodated by the growth system. The bubbler inlet tube extends into the organometallic fluid, nearly to the bottom, and delivers carrier gas which bubbles up through the liquid to the outlet tube. (See Figure 5.1) This allows the carrier gas to be saturated with precursor vapor to be carried to the reactor. The same design was initially used for solid sources, which are typically granulated. The solid can be depleted around the

inlet dip tube or blown away by the carrier gas, causing poor repeatability and low usable precursor fraction. Simply reversing the flow through the bubbler for solid sources helps this problem significantly. Two reverse flow bubblers in series essentially ensures carrier gas saturation at any reasonable flow rate.

Each bubbler is immersed in a constant temperature bath of an ethylene glycol/water mixture. Constant temperature is required for repeatability, otherwise the vapor pressure of each precursor would fluctuate with room temperature. For this research, relatively low precursor flux demand allowed all bubblers to be maintained well below room temperature. This is advantageous in that downstream lines do not need to be heated to prevent condensation, which can be difficult to achieve uniformly. Individual bubbler temperature is chosen based on vapor pressure and expected demand.

Constant temperature combined with constant pressure allows the amount of precursor delivered to be controlled simply by varying the flow through the bubbler. Constant pressure is maintained with a downstream automated pressure controller for each bubbler. The type of pressure controller used requires upstream pressure to be greater than downstream pressure to function properly. For this research, reactor pressure is always atmospheric (~740 Torr) or less. A bubbler pressure of 900 Torr at the pressure controller located at the bubbler outlet (see figure Figure 5.1) was found to be compatible with flow requirements of all seven bubblers.

Since gas flow is the single parameter that determines the amount of precursor delivered to the reactor, it must be accurately and precisely controlled. Mass flow controllers (MFC's) are used to carefully meter gas flow through the bubblers and all other flows that enter the manifold. MFC's are calibrated for a specific gas and the readout is in

percent of full scale volume flow. In reality, mass flow is measured (not volume flow) via heat transport in the gas flow. Therefore, the volumetric units used are standard cubic centimeters per minute (sccm) or standard liters per minute (slm), based on the gas used for calibration at a given temperature and pressure. This information can be used to calculate the molar flow rate,  $f$ , of precursor delivered by a given MFC setting by the following equation.

$$f = \left[ \frac{P_{om}}{P} \right] f_{mfc} \quad [ 5.1 ]$$

$P_{om}$  is the partial pressure of the organometallic,  $P$  is the total bubbler pressure, and  $f_{mfc}$  is the molar flow of the carrier gas determined by the ideal gas law at manufacturer specified pressure and temperature.

### 5.2.2 Reactor

The standard reactor unit was replaced with a custom reactor, designed and built in-house and shown schematically in Figure 5.4. Temperature is modulated by a 7500W Ameritherm RF power supply inductively coupled to a SiC-coated graphite susceptor. Inductive heating requires the growth chamber walls near the susceptor to be made of non-suscepting material which rules out metals. Quartz is suitable in this role and stock shapes are available in a variety of standard sizes. Quartz can also be machined into complex shapes and has the mechanical strength to withstand the typical temperatures and pressures used in OMVPE. It was found that a dividing plate is necessary between the III and V inlets of the quartz chamber to prevent gas-phase reactions. The optical micrograph on the left of Figure 5.3 reveals small black specs on the surface of GaAs attributed to a gas phase reaction during growth. These features were present on all films grown in the initial growth

chamber without a plate to divide the column III and V gases. The image on the right is a typical smooth GaAs film grown after the growth chamber was redesigned to incorporate the divider plate and reduce gas phase reactions.

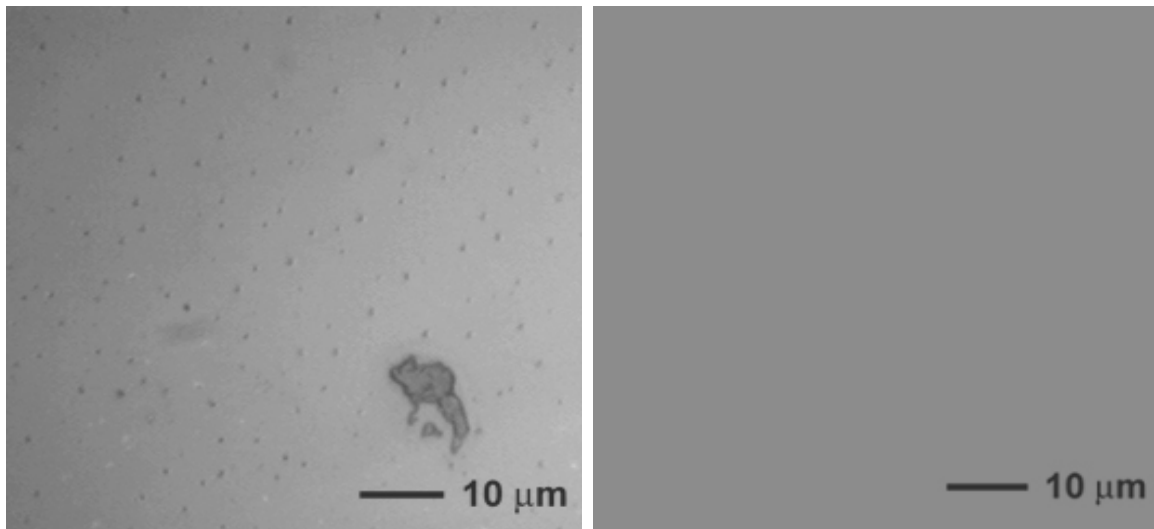


**Figure 5.3** Optical Micrographs(1000X) of Small Surface Features on GaAs from a Gas Phase Reaction (left) and a Smooth Surface for GaAs Grown after a Divider Plate was Added to the Growth Chamber to Seperate Gas Flows(right)

Substrates are heated and supported by the susceptor during growth. Graphite susceptors are used for inductive coupling, but can supply unwanted carbon to the reaction. SiC is used as a coating to contain the carbon and is thermally and chemically stable at temperatures much higher than those typically used for III-V semiconductor growth. Temperature is controlled via a feedback loop consisting of a Type K thermocouple in close proximity to the susceptor, connected to a standard Eurotherm<sup>147</sup> PID process controller.

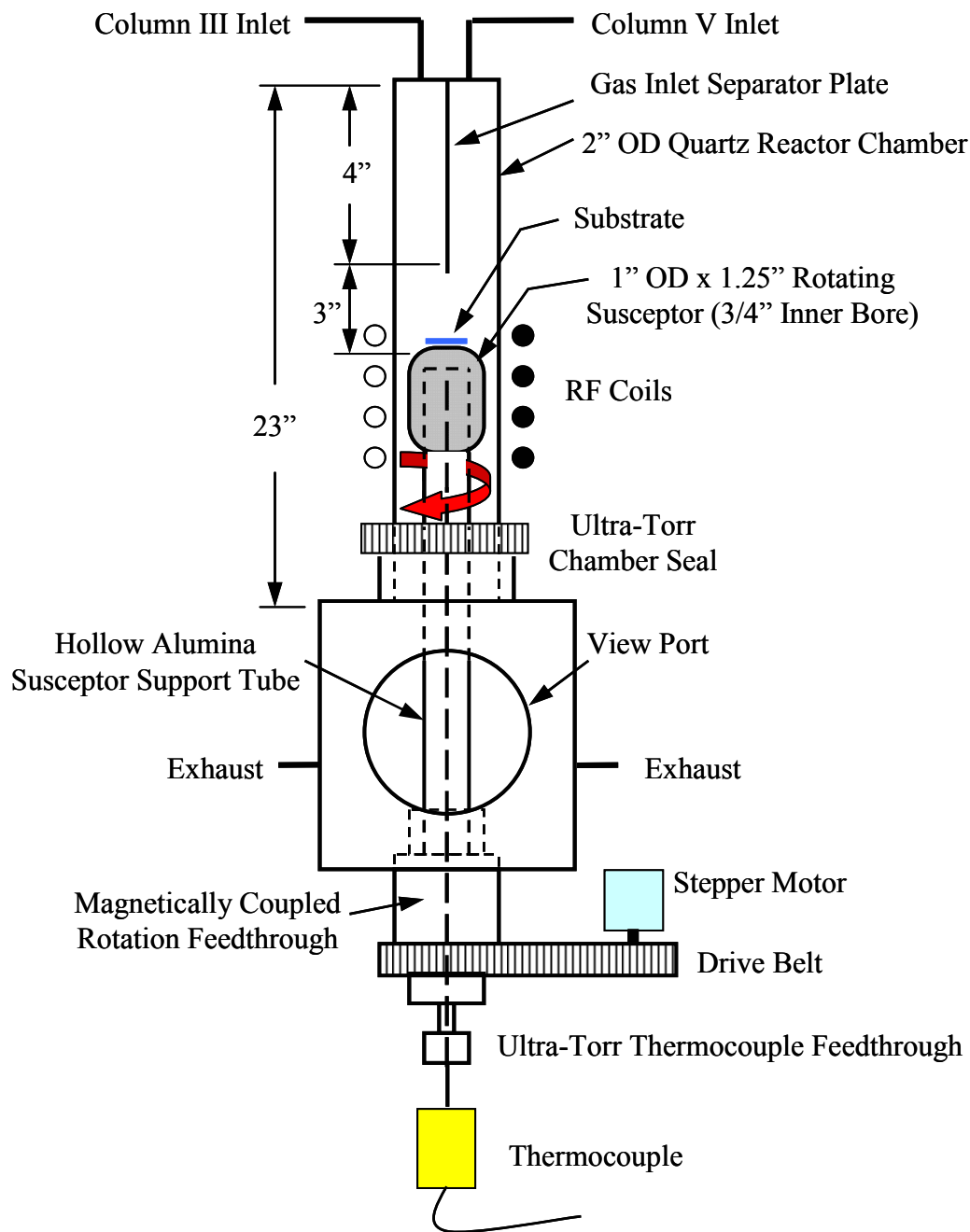


**Figure 5.4** Reactor Schematic

Susceptor rotation is critical for film uniformity. By rotating the susceptor, small inconsistencies in the temperature profile are smoothed out. Also, rotation equally exposes

the substrate to the incident gas flow in case the divided streams are not fully mixed at the growth surface. Temperature measurement of a rotating part can be difficult to realize continuously, reliably, and inexpensively. The unique magnetically coupled feedthrough facilitates both temperature measurement and rotation. The outer hub contains strong permanent magnets which couple to an inner through-bore shaft made of a permanent magnet. This is analogous to a magnetic stirring plate and stir bar found in a typical chemistry lab, but with more controlled rotation and stronger coupling. Many reactors use a mechanical feedthrough for rotation that requires a dynamic seal around a rotating shaft. These seals can be unreliable and can have very short service life especially for dirty processes. The magnetically coupled feedthrough removes the need for such a seal. A drive belt connects the outer hub of the magnetically coupled feedthrough to an electric drive motor which in turn is interfaced to a computer to automate rotation. The inner rotating shaft terminates in a flange. A mating flange was constructed to attach a hollow alumina tube which extends into the growth chamber. The bottom of the susceptor is bored nearly to the top surface, just slightly larger than the alumina tube, so the susceptor slips over the tube. Friction is adequate to couple the two pieces during rotation. The hollow inner shaft and alumina tube allow a thermocouple to be inserted all the way to the inside of the susceptor, less than 2mm from the back of the substrate. The thermocouple remains stationary so the feedthrough is static and simple. Figure 5.5 is a photograph of the reactor.



**Figure 5.5** Photograph of Reactor

Placement of the thermocouple tip should be repeatable for consistency when the thermocouple is replaced as it is a consumable part. This was accomplished by selecting a standard Type K thermocouple with a stainless steel sheath and inserting it until just touching the susceptor. The susceptor was then heated near typical growth temperatures and rotated for several minutes. The SiC coating easily ground away a few microns of the sheath until a very small space was left between the thermocouple tip and the susceptor.

This arrangement proved to be very reliable. Any particles generated while conditioning the thermocouple sheath were well contained within the alumina tube. The tube also protected the thermocouple from reaction chemicals and vice versa. All reported temperatures are as-read from the thermocouple readout. Calibration to the actual substrate temperature, via optical pyrometer, indicates a deviation of 20-25°C.

### 5.2.3 Exhaust System and Scrubber

Reactor pressure is modulated via a 25CFM Alcatel rotary vane pump and a micro-stepping butterfly valve, located downstream in the exhaust system. The pressure feedback loop consists of a Baratron pressure sensor, located near the reactor exit, and standard pressure controller, both from MKS Instruments.<sup>148</sup> Dual exhaust ports on the reactor helps maintain vertical flow through the reactor without cumbersome baffles. Reduction of pressure below one atmosphere is common in OMVPE growth to reduce gas-phase reactions or to reduce convection eddy currents in poorly designed reactors. Gas velocity and mean free path increase with decreasing pressure. By increasing the mean free path, molecules have fewer collisions before impinging on the substrate, so the probability of a premature reaction is reduced. Increasing the gas velocity can reduce eddy currents or deleterious buoyancy effects, and will increase growth rate in the mass transport limited regime.

Initial qualification of the reactor used in this research was performed at atmospheric pressure. Gas-phase adduct formation, manifested as surface features similar to the left image of Figure 5.3, required a pressure reduction and ~70 Torr was chosen. Adduct formation was reduced, but film quality was poor and hazy to the eye. Under magnification, the surface of GaAs films appeared to have metallic droplets, presumably Ga. The optical micrograph in Figure 5.6 is from a region near the edge of the substrate where the problem

is worse. Increased gas velocity reduces the residence time of precursor molecules in the heated area near the susceptor. Pyrolysis efficiency can be greatly reduced below the expected rate for a given growth temperature. While some pyrolysis of TMG must occur to deposit Ga, volatile As will desorb from the surface if TBA pyrolysis efficiency is not adequate to provide an As overpressure in the reactor. The effective V/III ratio in this scenario is less than expected compared to the case of complete pyrolysis of the precursors.

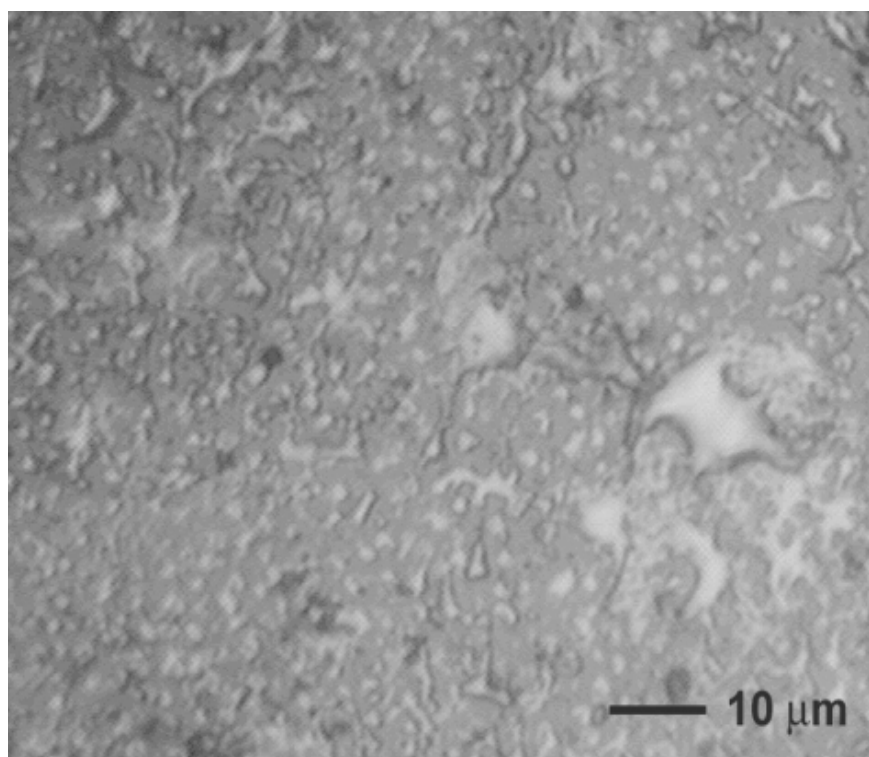


**Figure 5.6** Optical Micrograph (1000X) of a GaAs Surface Grown at 70 Torr (Metallic Droplets are Presumed to be Unreacted Gallium)

An increase in the group V precursor, or V/III ratio, significantly improved film quality, demonstrating a common problem with reduced pressure growth. To conserve expensive precursors, the pressure was optimized to balance gas-phase reactions and gas

velocity. A pressure of 200 Torr produced essentially zero gas-phase adducts and reduced the gas velocity to the point that only a marginal increase in the column V source was required. Films grown at these conditions were featureless and specular under magnification. From a reactor design perspective, this problem could be solved with a better susceptor. Incoming gases establish laminar flow and the flow stagnates at the hot susceptor where the reaction occurs. If the flow is to stagnate over the whole substrate, the susceptor should be significantly larger so the substrate is positioned in a “sweet spot.” Viewing the current susceptor from the top, the 14mm x 14mm substrate covers most of the surface area of the 24mm diameter susceptor. (See Figure 5.7) Clearly the corners may suffer from improper flow stagnation. Fortunately, a pressure of 200 Torr provided uniform high quality films and no gas-phase reactions. In retrospect, matching the shape of the susceptor to the shape of the substrate, is preferred over a square substrate on a circular susceptor.

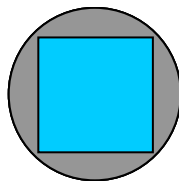


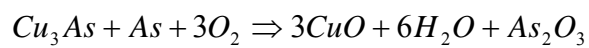
**Figure 5.7** Substrate Susceptor Coverage

In addition to regulating reactor pressure, the exhaust system carries reaction byproducts away from the reactor. Many of the byproducts are still volatile and dangerous, so they are pumped through a pyrolysis furnace (400°C) for further decomposition. The pump is protected from the hot reactive gases by Fomblin®, an inert, non-flammable perfluorinatedpolyether (PFPE) lubricant used in place of mineral oil. The pyrolysis furnace is a heated section of tubing filled with stainless steel beads to provide a large surface area to

catalyze the reaction. Exhaust gases then pass through a particle filter to remove the bulk of the contaminants. Many of the remaining contaminants are harmless elements or molecules and are safe to return to the environment. Arsenic and arsine which form from the decomposition of TBA, however, are toxic and must be removed. Exhaust gases pass through a Novapure effluent gas scrubber designed to remove these hazardous materials before finally being returned safely to the environment. The scrubber houses proprietary chemisorptive resins in a canister. Exhaust gases are pumped through the canister before returning to the common exhaust facility. As an example, a typical reaction for the removal of arsine is



For safety, the trapped As is rendered inert by the following oxidation reaction.



The scrubber is oxidized on a monthly basis by a 10 liter/minute flow of a nitrogen/oxygen mixture that is gradually increased from 5-100% oxygen over at least 4 hours. Five thermocouples are spaced along a thermowell in the canister to monitor temperature. Any rise of more than a few degrees indicates the oxygen fraction is being increased too rapidly.

#### 5.2.4 Equipment Cleanliness and Film Purity

Semiconductor devices require the highest levels of material purity for proper performance. As we have seen from the discussion of dopants, which are intentional impurities, a very small fraction of impurity atoms can greatly affect electrical properties. Film purity is directly linked to precursor purity and growth system cleanliness.

Most common precursors can now be delivered with adequate purity from the supplier. All gas sources used in this research are passed through a resin filter to ensure a

high purity level is attained. The filters also serve as a safeguard against supplier errors and from water vapor and oxygen that may enter the system during a gas bottle replacement. Organometallic precursors can be further purified by careful distillation, but this practice is very dangerous and should be avoided if possible. All OM sources in this work were used as supplied by the manufacturer.

OMVPE growth systems are constructed of low vapor pressure materials that will not outgas and contribute unwanted species to the reaction. Additionally, the construction materials must not chemically react when exposed to precursors. 316L stainless steel (SS) is appropriate for most applications and is used extensively. The gas delivery manifold is constructed of a series of stainless steel tubing, valves, mass flow controllers, and pressure controllers. While some of these components are constructed with other materials, the wetted surfaces are almost entirely stainless steel. One exception is polymer valve stem seats that ensure full valve closure which comprise a very small fraction of the total wetted surface. For the reactor, high temperature refractory materials, such as alumina, quartz, and SiC, can be used when SS is inappropriate. Use of these materials should be limited however due to high porosity and surface roughness. Rough surfaces can absorb large amounts of water vapor when the system is exposed to air which negatively impacts crystal growth because of the strong affinity between water and organometallic compounds. The large number of gas lines represent a very large surface area, so they are internally electropolished to produce an extremely smooth finish with low surface roughness. Loading a substrate into the reactor is the most frequent opportunity for contaminants to enter the system. A load lock can minimize exposure by first loading the substrate into an intermediate chamber between the growth system and the surrounding environment. The

load lock is repeatedly purged with an inert gas and then opened to the system. Substrates are then transferred via a manipulation arm to the susceptor. While effective, load locks can be expensive, complicate reactor design, and are time consuming to operate. Another solution is to enclose the reactor unit in a glove box continuously purged with an inert gas to displace air. A simplified load lock is then used to pass substrates into the glove box. Both sides of the load lock can be accessed by hand, removing the need for mechanical manipulators. Glove boxes have the added advantage of reducing contamination via diffusion. Inevitably, some species will diffuse through all construction materials into the growth system. While this can not reasonably be prevented entirely, some materials are more susceptible to this problem than others. Metals typically have a low diffusion rate for contaminants whereas polymers have a much higher rate. This is important at the junctions of various system components. All seals between components in the gas delivery system are metal, but this is not always possible in the reactor. Polymer o-ring seals are used for various reasons included sealing between two dissimilar materials and to ease substrate loading or maintenance. A glove box helps minimize the amount of contaminants exposed to these high-diffusivity polymer seals.

Even with all of these measures in place, some contamination will occur either from build-up over time, maintenance procedures, or human error. To maintain an existing clean system, a flow of pure inert gas such as nitrogen is used to purge all wetted surfaces while the system is idle. The flow is continuous, around the clock, and gradually cleans the system from small amounts of contamination. For a system recently exposed to air, a more rapid cleaning is required. Using the system pump, the exposed volume is reduced to a low pressure and heated to increase contaminant desorption rate. After some time, determined

by the degree of contamination, pressure, temperature, and wetted surface characteristics, the level of contaminants is reduced to an acceptable level. Since water vapor is common and more difficult to remove than other contaminants, the growth system is equipped with a commercially available moisture monitor, sensitive to parts-per-billion water vapor concentration. The readout display for the sensor is expressed as the dew point. Water vapor concentration can easily be attained by dividing the vapor pressure at the indicated dew point by the total pressure at the detection location or by reading the value from a chart supplied by the manufacturer. The lower limit of detection for the sensor used is  $-110^{\circ}\text{C}$  dew point which corresponds to less than 1ppb for the 100psi process line where the sensor is located. During normal operation, water vapor concentrations drop below the detection limit. In practice, the system is not operated until the water vapor level drops below the detection limit and all activities are ceased in that event that the concentration rises into the detectable range until to problem is corrected.

### 5.3 GROWTH CONDITIONS AND PROCEDURES

Growth of final device structures is precluded by many growth runs of single layers to qualify the reactor and to calibrate precursor flows to produce the desired film composition and quality. Careful integration of each layer into the final structure leads to the development of a recipe that accounts for the fundamental OMVPE process applied to a specific reactor. Various procedures are developed consistent with cleanliness, reactor requirements, and the final device structure.

### 5.3.1 GaAs Substrates

All films were grown on (001) oriented GaAs substrates, off-cut  $2^\circ$  toward the [011] direction from Wafer Technology Ltd.<sup>149</sup> These wafers are produced with the vertical gradient freeze (VGF) method which produces the lowest dislocation density. Zinc doped p-type, silicon doped n-type, and undoped semi-insulating wafers were all used when appropriate. Detailed specifications of each can be found in Appendix B. Misorientation of the wafer by  $2^\circ$  produces steps which encourages the preferred step growth mechanism discussed previously. Two inch diameter wafers are received from the manufacture with a surface polish that renders them ready for immediate epitaxial growth without further preparation, or “Epi Ready.” However, for this work, the wafers are cleaved into seven 14mm x 14mm square substrates, significantly reducing the substrate budget. Care is taken to handle the substrate as little as possible while cleaving, but subsequent preparation is required to restore the surface integrity. All substrate manipulation is performed with tweezers. Each square substrate was subjected to the following procedure before loading into the reactor for growth. Very clean Teflon® beakers were used as cleaning vessels. Substrates were placed in the beaker and the active chemicals were introduced for the specified amount of time and then thoroughly rinsed by repeated filling and draining with deionized (DI) water.

1. Sulfuric acid ( $\text{H}_2\text{SO}_4$ ) etch for 1 minute to remove metals or ions remaining from the polishing process
2. Thorough DI water rinse for several minutes
3. 5:1:1 ratio of DI water – hydrogen peroxide( $\text{H}_2\text{O}_2$ ) – ammonium hydroxide( $\text{NH}_4\text{OH}$ ) etch for 30 seconds ( $\sim 10\text{nm}$ ) to remove subsurface damage

4. Thorough DI water rinse for several minutes
5. Hydrochloric Acid(HCl) etch to remove native oxide
6. Thorough DI water rinse for several minutes
7. Remove substrate from beaker and quickly dry with pure, dry nitrogen
8. Immediately load substrate into reactor

It was noted that the substrate should remain immersed in liquid for the duration of the procedure, until extraction for drying, to prevent forming hazy spots on the surface. Drying should be done by directing a jet of nitrogen from one edge of the substrate to the opposite edge so the water is driven off with a sheeting action.

### 5.3.2 Reactor Loading and Routine Maintenance

Substrates are loaded into the reactor by removing the quartz chamber to expose the susceptor. (See Figure 5.4) The substrate is then carefully placed on the susceptor with tweezers. The quartz chamber is then replaced and the reactor is cycle-purged several times with nitrogen to remove air and contaminants. In practice, the quartz chamber accumulates a significant amount of deposition during a growth run which should be removed between consecutive runs. Films grown with a coated chamber from a previous run were typically hazy to the naked eye. Multiple identical quartz chambers were constructed so a clean chamber is installed each time a substrate is loaded. Dirty chambers are etched in an *aqua regia* (50% Nitric Acid – 50% Hydrochloric Acid) solution which rapidly removes any deposition. After removal from the acid bath, the chamber is rinsed successively in DI water, methanol, and acetone. Finally, it is dried with nitrogen and stored for the next use. This type of reactor design is not ideal in that the wetted surfaces are exposed to air during

each loading sequence. The effect is noticed in carrier mobility values, reported later, that are somewhat below the best values reported in the literature. A glove box would improve this situation, but the measured mobility values are adequate for the purposes of this research.

The susceptor accumulates deposition over several runs which must be removed. Otherwise, the build-up acts as an additional source of both precursors and contaminants which disrupts normal growth. Removal is accomplished by heating the susceptor a few hundred degrees above the growth temperature and reducing the system pressure to only a few Torr. It was found that this is necessary to bake the susceptor approximately every four growth runs at 900°C for 1 hour to restore it to near original condition.

### 5.3.3 Film Growth Details

Once a new substrate is loaded, system operation is fully computer automated. A recipe is loaded into the control software which dictates temperature control, pressure control, precursor flux, susceptor rotation, and gas switching. Each layer has specific requirements, but many conditions are similar and can be generally summarized. Organometallic and gaseous precursors for each element are listed in Table 5.1. Precursors are supplied by various manufacturers, including Epichem, Inc., Voltaix, Inc., EMF Ltd., and Rohm and Haas Electronic Materials.

**Table 5.1** List of Precursors

Element	Precursor	Chemical Formula	Abbreviation
Ga	Trimethylgallium	$\text{Ga}(\text{CH}_3)_3$	TMG
As	Tertiary-butylarsine	$\text{C}_4\text{H}_9\text{AsH}_2$	TBA
In	Trimethylindium	$\text{In}(\text{CH}_3)_3$	TMI
P	Tertiary-butylphosphine	$\text{C}_4\text{H}_9\text{PH}_2$	TBP
Al	Trimethylaluminum	$\text{Al}(\text{CH}_3)_3$	TMAI
N	Dimethylhydrazine	$(\text{CH}_3)_2\text{NNH}_2$	DMHz
Mg (p-dopant)	Bis(cyclopentadienyl)magnesium	$\text{Mg}(\text{C}_5\text{H}_5)_2$	$\text{Cp}_2\text{Mg}$
Si (n-dopant)	Disilane	$\text{Si}_2\text{H}_6$	-

Film growth initiation is similar for all growth runs. A  $1.5\mu\text{m}$  thick layer of GaAs is grown with doping levels similar to the substrate. Material at the initial growth interface can be defective and this buffer layer creates a new template removed from the defective area for subsequent layers. Temperature is first ramped to  $625^\circ\text{C}$  with an overpressure of TBA to prevent arsenic desorption and held for 2 minutes to desorb any native oxides that may have formed. Then temperature is reduced to the growth temperature and TMG flow is directed to the reactor along with any dopant precursors to begin growing the buffer layer. Once the buffer layer is complete, the gas composition is modified to create the next desired layer. Device requirements of the proposed structure dictate that a balance of many competing growth parameters be made and many growth runs are required develop the correct conditions for each layer. Nearly 1000 individual runs were performed over the course of this work. For the solar cell structure in this research, growth conditions can be divided into bulk growth and quantum well growth as summarized in Table 5.2 and Table 5.3. Total reactor pressure is 200 Torr and susceptor rotation speed is 120RPM for all layers.

**Table 5.2** Bulk Film Growth Parameters

	GaAs	n-GaAs	p-GaAs	p <sup>+</sup> -GaAs	p <sup>+</sup> -AlGaAs
Temperature °C	600	575	625	625	625
TMG Flux (moles/min)	0.00894	0.00894	0.00894	0.00894	0.00894
TBA Flux (moles/min)	0.10346	0.13794	0.06897	0.08621	0.08621
TMAI Flux (moles/min)					0.00175
Dopant Flux (moles/min)		1.16 x 10 <sup>-7</sup>	0.000059	0.000082	0.000073
V/III Ratio	12	15	8	10	8
Growth Rate (Å/sec)	7	7	7	7	7

Quantum well growth required extensive calibration to isolate the required parameters. For multinary alloys, a flux range may be given to represent the compositions studied. The SLS is grown by alternating TMI and TBP flow into the reactor while TMG and TBA are continuous and constant. A 1 second pause between switching the flows helps prevent intermixing of the compositions in the gas phase. Characterization of the SLS by x-ray diffraction, as described in section 6.2, does not clearly indicate a periodic structure if the 1 second pause is omitted. Intermixing of the TMI and TBP precursors at each switching event may produce an unwanted layer of unknown composition that disrupts the InGaAs/GaAsP interface.

**Table 5.3** Quantum Well Growth Parameters

	InGaAs	InGaAsN	GaAsP	GaAsPN
Temperature °C	575	575	575	575
TMG Flux (moles/min)	0.00268	0.00268	0.00268	0.00268
TBA Flux (moles/min)	0.03448- 0.06897	0.03448- 0.06897	0.03448- 0.06897	0.03448- 0.06897
TBP Flux (moles/min)			0.40789- 0.81579	0.81579
TMI Flux (moles/min)	0.00044- 0.00202	0.00152- 0.00202		
DMHz Flux (moles/min)		0.46290- 0.86793		0.46290- 0.57862
Silane/Cp <sub>2</sub> Mg Flux if Doped (moles/min)	5.80 x 10 <sup>-8</sup> / 5.03x10 <sup>-5</sup>			
V/III Ratio	7-11	106-192	165-317	338-533
Growth Rate (Å/sec)	5.5	5.5	5.5	5.5

TBA and TBP were selected as arsenic and phosphorous precursors over traditional arsine(AsH<sub>3</sub>) and phosphine(PH<sub>3</sub>) for several reasons. Both arsine and phosphine are highly toxic gases. Large volumes stored in high pressure bottles for industrial use present a serious safety hazard for personnel during handling. In the event of a leak, the deadly gases can rapidly expand to fill a room or building and present a large liability. TBA and TBP are somewhat less toxic and more importantly are liquids, usually stored near atmospheric pressure. Handling is much safer and a leak should be localized to a small area. In addition to safety concerns, arsine and phosphine are stable molecules, requiring high growth temperatures, up to 700°C<sup>150</sup> and 900°C<sup>151</sup> respectively, for complete pyrolysis. Incomplete pyrolysis is problematic because the concentration of the precursor is highly sensitive to

temperature. Small changes can dramatically change the amount of available reactive species. Even slight temperature non-uniformity across the substrate can result in poor compositional uniformity in the film. Growth of high quality InGaAs with high In content requires relatively low growth temperatures, as noted in the table above. Likewise, dilute nitrides require lower temperatures to achieve appreciable N composition.<sup>152</sup> TBA and TBP undergo full pyrolysis at temperatures lower than those used in this research. When TBA and TBP were first proposed as replacements for arsine and phosphine, reported material quality was poor.<sup>153</sup> Purification methods have improved since then and material quality matches and sometimes exceeds material grown with arsine and phosphine.<sup>154</sup> The need for lower growth temperatures prevents use of the traditional N source, ammonia(NH<sub>3</sub>). Even at 950°C, only 15% of NH<sub>3</sub> decomposes to provide elemental N.<sup>155</sup> Cracking efficiency at the desired growth temperature is essentially zero. Only in the past several years have alternative N precursors been available and very recently are available with acceptable purity level. DMHz decomposes at temperatures similar to TBA and TBP, and has been utilized successfully as a N precursor for both dilute nitrides<sup>156,157</sup> and GaN<sup>158</sup> at low temperatures. Silane(SiH<sub>4</sub>) is frequently used as the Si dopant source in III-V growth, but also suffers from incomplete decomposition at the desired temperatures. Fortunately, less stable disilane(Si<sub>2</sub>H<sub>6</sub>) is readily available with high purity and has been effectively demonstrated for GaAs doping.<sup>159</sup> The relatively low disilane flux reported in Table 5.2 is a result of both the high doping efficiency of Si and the fact that each disilane molecule provides two Si atoms. Achieving such a small flow can be difficult. First, the source bottle contains only 1% disilane in nitrogen. A dilution manifold is used to thoroughly mix the Silane/nitrogen mixture with additional nitrogen. This new mixture is mostly dumped to the

vent and a small amount is bled off to the input manifold through a MFC. A typical scenario is to have 2.5SLM of diluting  $N_2$  mixed with 100sccm of the tank mixture, with 4sccm of the resulting mixture going to the reactor. It is important to note that growing the proposed structure is simply not possible without these relatively new precursors.

## 6 CHARACTERIZATION

Development of a successful OMVPE process requires that film properties be related back to specific growth conditions. For a particular film or structure, several successive runs are performed with varying growth parameters. Post-growth film analysis yields a data set describing the nature and magnitude of the effect of adjusting each growth parameter. Using this information, growth conditions can be modified with predictable results. A myriad of standard characterization equipment and techniques is available for this purpose.<sup>160</sup> Following is a review of each one utilized in this device structure development.

### 6.1 OPTICAL MICROSCOPY

Before any complex analysis is performed on a newly grown film, a good deal of information may be gained by simply observing the surface with an optical microscope. This is perhaps the most under-utilized technique because it is largely qualitative, but a well trained eye can frequently relate observed features to specific growth problems. In reality, the first characterization step is observation with the naked eye. For this material system, high quality films appear specular and smooth. With rare exception, hazy or pitted surfaces indicate poor film quality. An Olympus optical microscope (BX41) reveals features too small to distinguish with the naked eye. The microscope is fitted with differential interference contrast (Nomarski) capabilities to produce contrast even with very small surface features. For example, Figure 6.1 is an image of an n-GaAs layer on GaAs that appeared specular and smooth to the naked eye. The surface roughness was caused by a growth temperature that was too low. When this sample was dried during pre-growth cleaning, the water was not removed with complete sheeting action. Sometimes small drops

break away from the water sheet during drying and leave stains as indicated by the arrow. By comparison, the third image in Figure 6.2 is a typical high quality featureless surface.

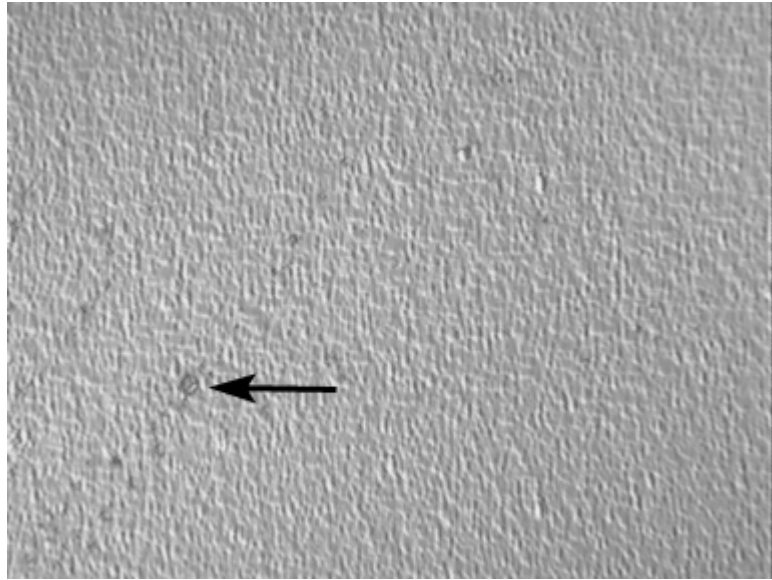


**Figure 6.1** Optical Micrograph (500X) Rough Surface of n-GaAs Caused by Low Growth Temperature (Arrow indicates a water stain from improper sample drying)

Lattice misfit dislocations in these cubic materials are inclined at  $60^\circ$  along two orthogonal  $\langle 110 \rangle$  directions. Analysis of the strain reveals that relaxation occurs preferentially along these directions.<sup>161,127</sup> Surface features from this relaxation mechanism can be viewed under magnification. This can be used as a quick method to determine if strain balance has been achieved when growing strained layer superlattices. The type of strain, either tensile or compressive, can be determined due to the different morphologies produced. Figure 6.2 shows compressively strained  $\text{In}_{0.1}\text{Ga}_{0.9}\text{As}$ , tensile strained  $\text{GaAs}_{0.8}\text{P}_{0.2}$ , and strain balanced  $\text{InGaAs}/\text{GaAsP}$  surfaces, all on GaAs substrates. Note that compressive strain results in continuous lines along both directions. Tensile stress produces discontinuous lines in one direction and continuous lines in the other. The strain balanced sample is featureless.

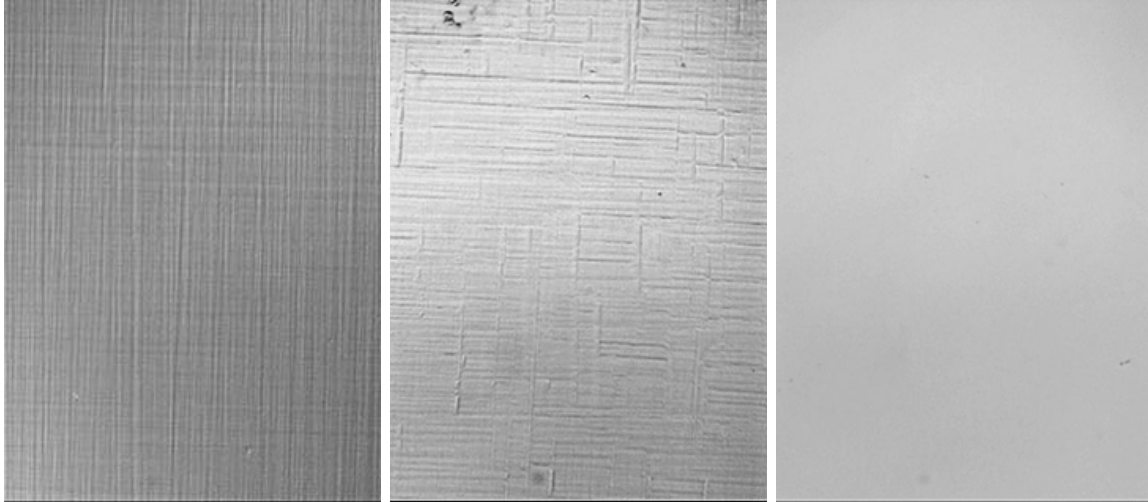


**Figure 6.2** Optical Micrographs (400X) of Cross Hatching in (1) Compressively Strained  $\text{In}_{0.1}\text{Ga}_{0.9}\text{As}$  and (2) Tensile Strained  $\text{GaAs}_{0.8}\text{P}_{0.2}$ , Plus the (3) Featureless Surface of a Strain Balanced  $\text{In}_{0.1}\text{Ga}_{0.9}\text{As}/\text{GaAs}_{0.8}\text{P}_{0.2}$  SLS

Optical microscopy is also utilized for some quantitative analysis. A sufficiently thick film, about 1 micron or more, can be measured in cross-section to establish a good approximation of the growth rate. A sample is first cleaved to expose an edge to view in cross-section. Since (001) GaAs cleavage planes are perpendicular to the top surface, very flat edge surfaces are produced without polishing. For similar materials of high structural quality, the film/substrate interface is usually not observable without additional preparation. However, the interface does have an appreciable dislocation density which can be exploited. Etching with dislocation preferential chemicals will delineate the interface adequately for observation with a microscope. Abrahams-Buiocchi chemical etch<sup>162</sup> (AB Etch) is well known and ideal for this application. The sample edge is dipped in the solution (8mg- $\text{AgNO}_3$  : 2mL- $\text{H}_2\text{O}$  : 1g- $\text{CrO}_3$  : 1mL-HF) for 2-3 seconds, quickly rinsed with DI water, and dried. For an accurate measurement, the sample must be mounted with the edge perpendicular to the focal axis. The measurement is made by capturing a digital image

(Figure 6.3) and comparing to a length scale calibrated to the magnification used. Since the substrates used are 14mm x 14mm, the thickness uniformity can also be determined.

Typically, films had excellent uniformity except for the expected edge crown, also shown in the figure.

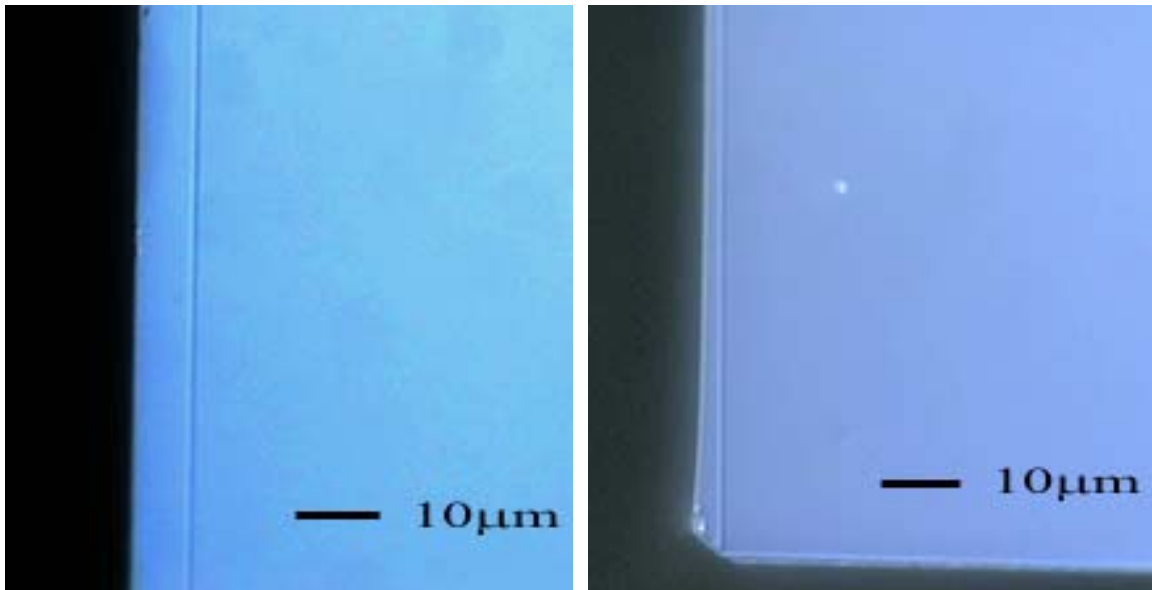


**Figure 6.3** Cross-Section Optical Micrographs (1000X) of AB-Etch Delineated Interface and Edge Crown

While cross-hatching is a qualitative way to observe the effects of lattice mismatch, it is possible to more directly observe the misfit dislocations. Since misfit dislocations are inclined at  $60^\circ$ , they terminate at the surface. Preferentially etching at points where dislocations intersect the surface forms pits, which can be counted over some area to give the dislocation density. This method works well unless the density is so high that there is a large amount of overlap of the pits, making it difficult to discern them for counting.

Samples were immersed in molten KOH at  $450^\circ\text{C}$  for 45 minutes to reveal the etch pits.

Refer to ASTM standard F 1404<sup>163</sup> for a detailed procedure. Two images in Figure 6.4 show the effect of strain balancing in reducing misfit dislocations. The first image is a thick relaxed layer of InGaAs grown on GaAs with an etch pit density (EPD) of  $\sim 10^5$ . The second image is a In<sub>0.12</sub>Ga<sub>0.88</sub>As/GaAs SLS on GaAs with an EPD of  $\sim 10^4$ .

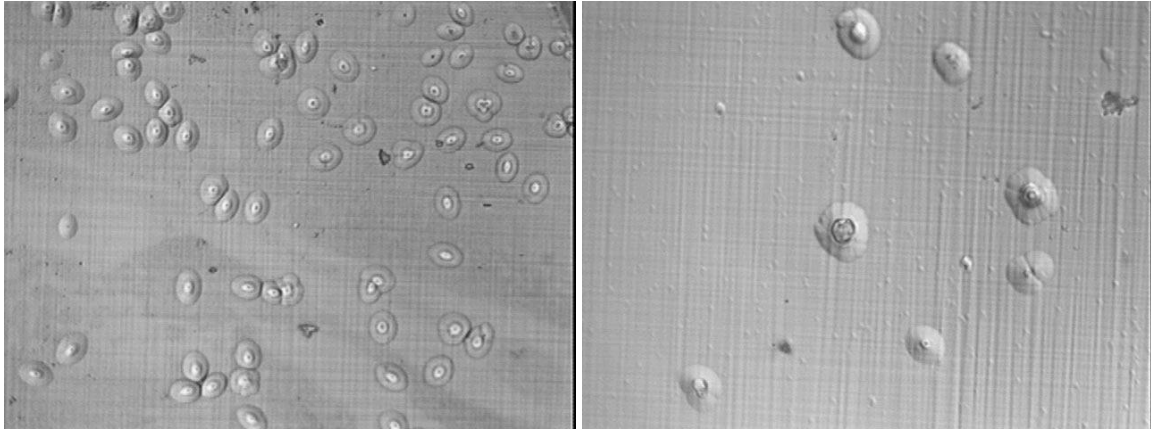


**Figure 6.4** Optical Micrograph (400X) of Etch pits for InGaAs/GaAs Double Heterostructure and InGaAs/GaAs Strained Layer Superlattice

## 6.2 X-RAY DIFFRACTION

X-Ray diffraction (XRD) is a non-destructive technique to analyze the crystalline structure of materials. When x-rays interact with a material, they are scattered by atoms. The regular periodicity of atoms in a crystalline solid scatter x-rays only at certain angles where there is strong constructive interference. At most angles, there is no scattering because the rays cancel each other. A typical diffractometer has a fixed source of x-rays directed to the material sample of interest and a detector. The sample and detector rotate to scan through a range of angles. Diffraction peaks are found at angles that satisfy the Bragg Law.

$$\lambda = 2d \sin \theta \quad [ 6.1 ]$$

$\lambda$  is the x-ray wavelength,  $d$  is the spacing between crystalline planes, and  $\theta$  is the diffraction or Bragg angle. The fundamentals of XRD are interesting and have been widely applied for materials characterization. Formal theory is presented by Cullity<sup>30</sup> and requires a detailed understanding of crystallography, also given by Wyckoff<sup>32</sup> and Kelly.<sup>31</sup> XRD was used to determine a variety information about individual films and the complete device structure.

Basic  $\theta$ - $2\theta$  scans were performed with a older Rigaku Geigerflex diffractometer. High resolution rocking curves where collected with a modern, 3-axis Philips X'Pert system. Both machines produce Cu  $K_{\alpha}$  (1.541838Å) radiation, but the Philips tool uses a four-bounce Ge (220) crystal to select only Cu  $K_{\alpha 1}$  (1.540562Å).  $\theta$ - $2\theta$  scans were used to determine the composition of ternary alloys. To do this, we first assume that Vegard's Law holds for the material being studied. Vegard's Law states that there is a linear relationship between alloy composition and the lattice parameter,  $d$ , if the atoms of each binary have similar bonding properties. In other words, the lattice parameter is only influenced by the relative size of the atoms. Consider an  $A_xB_{1-x}C$  ternary alloy as a mixture of AC and BC binaries with different lattice parameters. The lattice parameter of the ternary is given by

$$d = xa + (1 - x)b \quad [ 6.2 ]$$

where  $a$  and  $b$  are the lattice parameters of AC and BC, respectively. For this technique to be valid, a knowledge of the strain state of the film is required. If the film is under tensile or compressive strain, the lattice spacing will change to accommodate the strain. This can cause significant error in the composition calculation. It is possible to incorporate the effect of strain into the calculation with further analysis, but it is frequently more convenient to grow the film well past the critical layer thickness. Once the strain energy is accommodated

by misfit dislocations, the lattice constant returns to equilibrium. A typical  $\theta$ - $2\theta$  scan for a relaxed film of GaAsP is given in Figure 6.5. Each peak appears as a doublet because  $K_{\alpha 2}$  is not filtered from the beam.

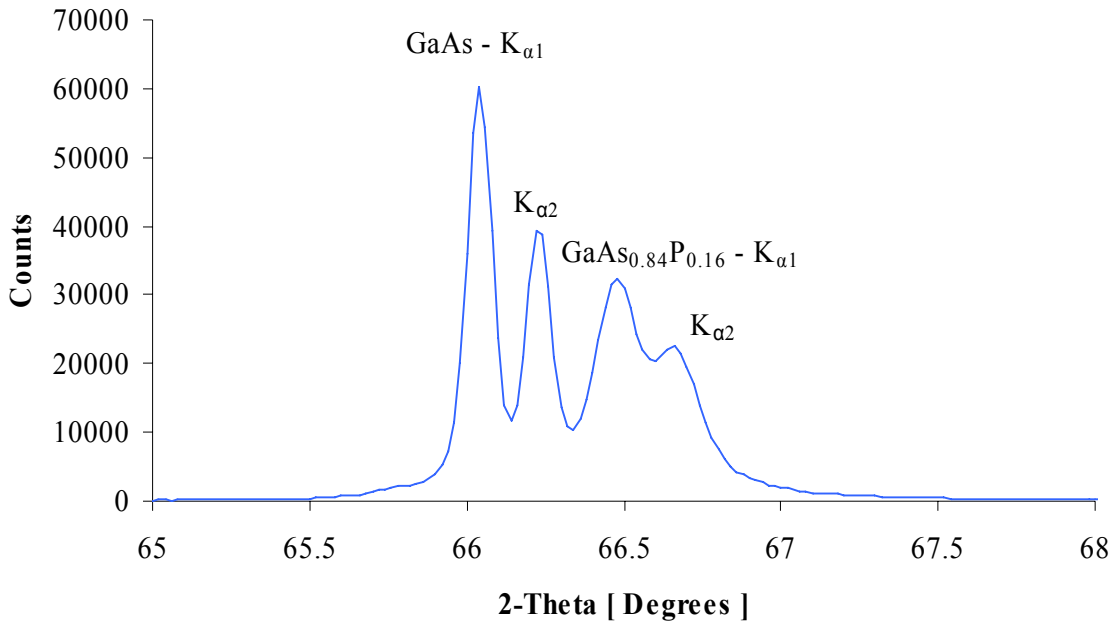


**Figure 6.5**  $\theta$ - $2\theta$  XRD Scan of a Thick GaAsP Film

High resolution rocking curves were used to evaluate the crystalline quality of films. The sample is scanned through a Bragg angle with very small angular steps. The full width at half maximum is increased by defects in the material, so this is a good method for evaluating changes in growth conditions. The incident beam must be highly parallel for rocking curves or it will also contribute to peak broadening, so the Philips system was used. Figure 6.6 is a sample rocking curve of a GaAsN film. Notice the broadening of the GaAsN peak compared to the very narrow GaAs substrate peak.

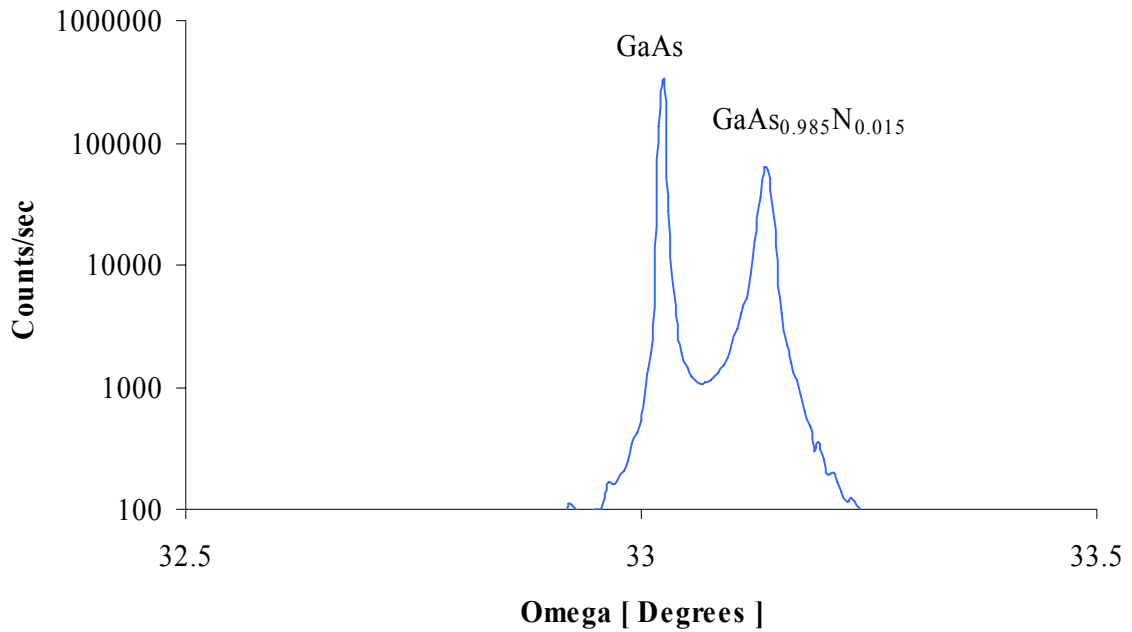


**Figure 6.6** HRXRD Rocking Curve of a GaAs<sub>0.985</sub>N<sub>0.015</sub> Film on GaAs

XRD analysis is possible because of the ray interaction with the periodic array of atoms in the crystal lattice. It is not surprising that other periodic structures also interact with x-rays. We take advantage of this to analyze the periodicity of SLS's. As x-rays travel through the structure they interact to form an interference pattern. The pattern is visible in the data as periodic, or Pendellosung, fringes decreasing with intensity away from and centered around the 0<sup>th</sup> order peak.<sup>164</sup> The periodicity of the SLS is related to the position of the peaks by

$$\sin(\theta_n) - \sin(\theta_{SLS}) = \frac{n\lambda}{2(t_1 + t_2)} \quad [ 6.3 ]$$

where  $\theta_n$  is the diffraction angle of the n<sup>th</sup> order peak,  $\theta_{SLS}$  is the angle of the 0<sup>th</sup> order peak, n is the order of the peak, and  $(t_1+t_2)$  is the period of the structure.  $t_1$  and  $t_2$  are the thicknesses of each layer in the structure and can not be found independently with this

method alone. Many of the samples analyzed had very few fringes, but this is expected because very thin layers have widely spaced peaks. This combined with the successive intensity decrease with increasing order makes high order peaks indiscernible. Poorly formed peaks were present for the thinnest layers investigated which may indicate imperfect interfaces. This is also not surprising because the growth time for very thin layers approaches the sweep out time for switching gas composition. For future work, this could be improved with a lower growth rate. However, rough interfaces may be advantageous for this structure. Most quantum well growth is intended to take advantage of quantum confinement which is enhanced with sharp interfaces. In this case, poor confinement will help carrier transport, but it is difficult to consistently introduce the same roughness. In addition to determining the periodicity, this technique helps fine-tune lattice matching. Notice in Figure 6.7, the 0<sup>th</sup> order peak is to the left of the substrate peak. This means that the average lattice parameter of the SLS is slightly larger than GaAs. Calculated misfit is 0.42%. When the 0<sup>th</sup> order peak appears concurrently with the GaAs peak, the lattice parameters are equal and the layers are lattice matched. To shift the 0<sup>th</sup> order peak in the figure to the right, the influence of In should be reduced. This can be done by reducing either the In composition or the InGaAs thickness. Conversely, the P concentration could be increased or the GaAsP thickness increased to correct the problem.

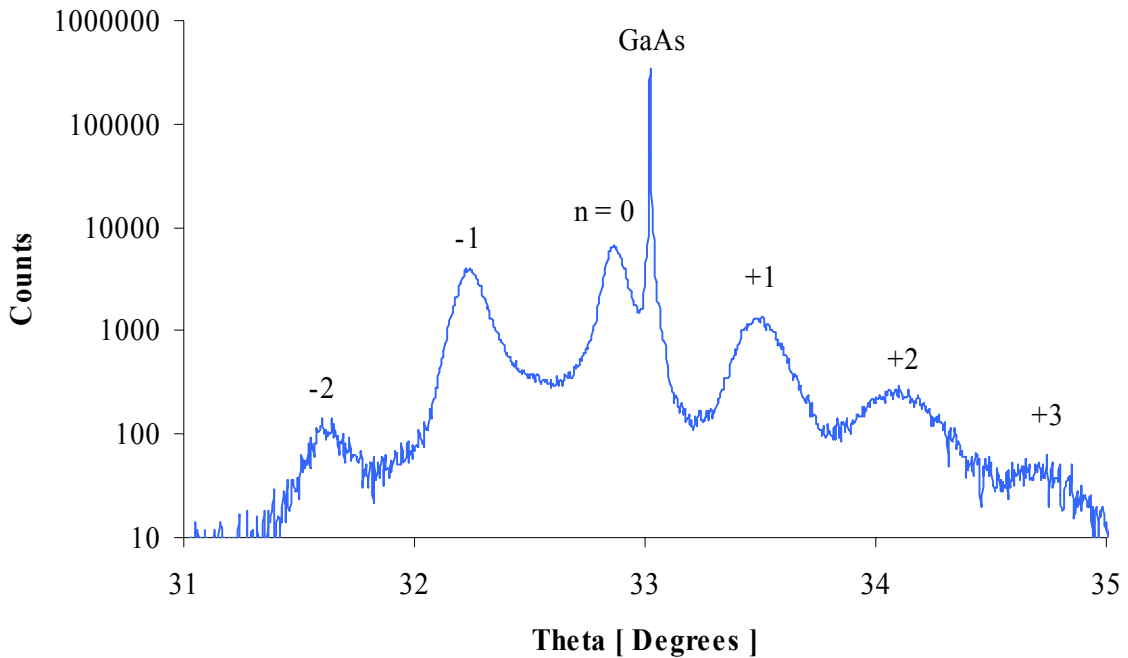


**Figure 6.7** HRXRD Scan of a Slightly Lattice Mismatched SLS with Pendellosung Fringes

### 6.3 PHOTOLUMINESCENCE

Photoluminescence is also a non-destructive technique and is useful for analysis of optical properties. Excess electron-hole pairs are created by exposing a sample to photons with energy greater than the bandgap of the material to be studied. The carriers quickly decay back to the band edges and then recombine. Radiative recombination generates photons which can be detected and yield valuable information. In a high quality semiconductor, the recombination will be from the conduction band back to the valence band which generates photons equal in energy to the band gap. Scanning a detector across wavelengths will show a peak at this energy, which is useful for bandgap determination in new materials. FWHM of the peak is an indication of optical quality, as XRD rocking curves are for crystalline quality. Other radiative recombination events can also be detected, such as transition from mid-gap impurity states, or “deep levels.” Deep levels may indicate

poor precursor purity, secondary phase formation, gas-phase reactions, or growth system contamination. PL can even be used for ternary composition determination to support, or in the absence of, XRD. Minority carrier lifetime time can be determined by time resolved photoluminescence (TRPL). Short pulses of light generate e-h pairs and the return to equilibrium is measured over time.

Photons are generated with a Spectra Physics Ar-Ion laser. The 514nm line (~1W) is selected via a prism, chopped, and focused onto the sample with a series of lenses and mirrors. Detection consists of a wavelength scanning monochrometer, a photomultiplier, and lock-in amplifier. Data collection is computer automated. PL scans of individual layers at 77K are given in Figure 6.8. Note the small deep level found in GaAsP and the broadening of the InGaAs peak.

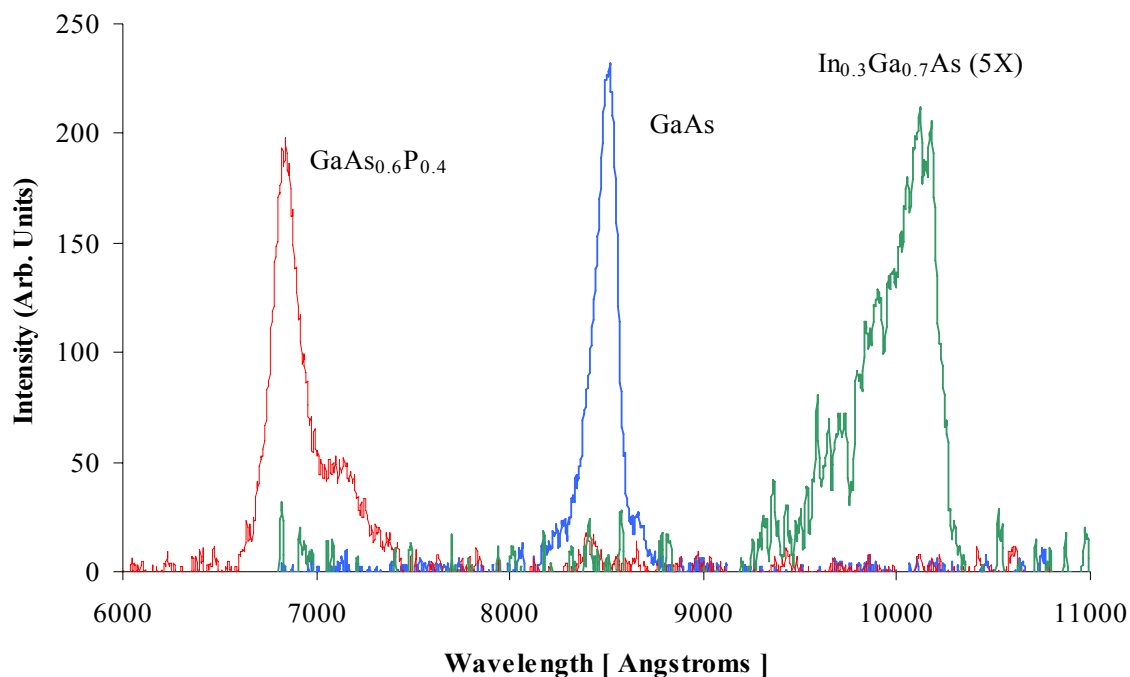


**Figure 6.8** 77K PL Scans of Thick Films of GaAs<sub>0.6</sub>P<sub>0.4</sub>, GaAs, and In<sub>0.3</sub>Ga<sub>0.7</sub>As

## 6.4 HALL EFFECT

Basic electrical characteristics were determined with Hall measurements in the van der Pauw<sup>165</sup> configuration. Resistivity, carrier concentration, mobility, and carrier type are determined with this measurement. With no magnetic field, the sheet resistance,  $R_s$ [Ohms/sq], is measured, so resistivity,  $\rho$ [Ohm-cm], is calculated by

$$\rho = R_s t \quad [ 6.4 ]$$

where  $t$  is the specimen thickness.

When a magnetic field,  $B$ , is applied perpendicular to a current flow, an electric field,  $E_{Hall}$ , is established to exactly balance the Lorentz force ( $qv \times B$ ) exerted on the majority carriers.  $E_{Hall}$  is mutually perpendicular to the magnetic field and current,  $I$  and is related to the current density and magnetic field by

$$E_{Hall} = \frac{R_{Hall} IB}{A} \quad [ 6.5 ]$$

where  $R_{Hall}$  is the Hall coefficient and  $A$  is the specimen cross section. The voltage resulting from  $E_{Hall}$  measured across the sample width,  $w$ , or the Hall voltage is given by

$$V_{Hall} = w E_{Hall} \quad [ 6.6 ]$$

Then by substitution into equation 6.5, the Hall voltage is

$$V_{Hall} = \frac{R_{Hall} IB}{t} \quad [ 6.7 ]$$

where  $t$  is the sample thickness. The sign of the of  $V_{Hall}$  and  $R_{Hall}$  indicate the carrier type, negative for electrons and positive for holes. For a single carrier type, the concentration ( $p$  or  $n$ ) is given by

$$R_{Hall} = -\frac{r_n}{nq} \text{ or } \frac{r_p}{pq} \quad [ 6.8 ]$$

Finally, the Hall mobility,  $\mu_{Hall}$ , is given by the following quotient.

$$\mu_{Hall} = \frac{|R_{Hall}|}{\rho} \quad [ 6.9 ]$$

Contacts were made with indium dots annealed for 1 minute at 440°C in nitrogen to establish ohmic behavior. The indium dots are then used as solder for gold wires for connection with the external circuit. An electromagnet provides a magnetic field of 3 kGauss. Current and voltage is supplied by Keithly sources interfaced with an Agilent multiplexer. The entire apparatus is computer automated for data collection. Measurements were also made at 77K by immersing the entire sample holder in liquid nitrogen.

Films for Hall analysis were grown on semi-insulating substrates so that only the film properties are measured. From the measurements, the carrier type, resistivity, and mobility is determined.

## 6.5 CURRENT-VOLTAGE AND SPECTRAL RESPONSE

Additional electrical characterization was performed on device structures. Current-voltage (I-V) measurements were performed with an Hewlett-Packard 4145B Semiconductor Parameter Analyzer. Dark measurements verify diode behavior of the junctions. Measurements performed under illumination reveal open circuit voltage,  $V_{OC}$ , and short circuit current,  $I_{SC}$ . These measurements are also used to calculate fill factor and, ultimately, efficiency. Illumination is produced with a 1000W Oriel solar simulator equipped with high pressure xenon bulb. The output spectrum is similar to the solar

spectrum, but requires conditioning for accurate simulation. This is done by placing specialized filters in the beam path. (see Figure 6.9) AM0 and AM1.5D options were available for testing. Mild concentration up to 8X is possible by adjusting beam power. A probing station is used to electrically contact the devices. The back contact was adhered to the probe station stage with silver paste. The top contact is probed with a micromanipulator, assisted with a microscope.

Spectral response is determined by repeated I-V measurements over a range of illumination wavelengths. Parts of the spectrum are selected with a series of 20nm bandpass filters rotated into the beam for each measurement. A standard GaAs pn-junction is used as the control for the experiment. Spectral response testing is key for evaluating solar cell performance and is discussed in detail in chapter 9.

The testing equipment is shown schematically in Figure 6.9. The solar simulator and filter wheel slide on rails and can be positioned over the probe station as needed. To probe the top contact, both are moved aside and a microscope (not shown) folds into place to assist probe placement with the micromanipulator. Dark I-V measurements are taken without the simulator or filters in place with all light sources extinguished. For light I-V, the simulator slides into position above the solar cell and is calibrated to the correct spectrum and power. For spectral response, a rotating wheel holding 8 filters is placed in the beam path. The wheel simplifies sampling different ranges of the spectrum by rotating a filter into the beam for each I-V measurement.

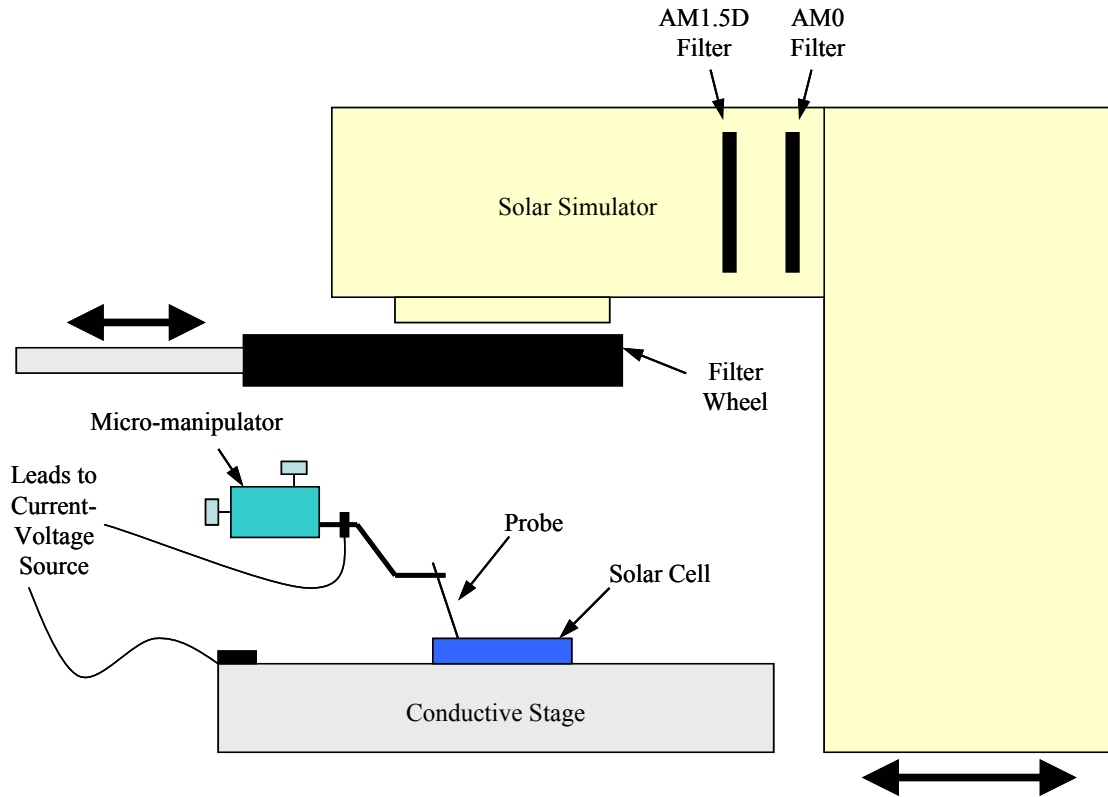


**Figure 6.9** Current-Voltage and Spectral Response Test Apparatus

## 6.6 TRANSMISSION ELECTRON MICROSCOPY

The thickness of the individual SLS layers is of critical importance to the intended function of the solar cell device. Therefore it is prudent to verify the XRD thickness measurement with some additional technique. Transmission electron microscopy (TEM) is the best method for measuring such small features, but is time consuming and labor intensive. As a result, it is used as the supporting evidence rather than the primary measurement technique. For these purposes, TEM is analogous to the measurement of thicker layers with optical microscopy discussed in section 6.1. An electron beam focused by magnetic lenses is used instead of a light beam focused by optics. The sample is also

extremely thin, or electron transparent, so the electron beam is scattered by the sample and detected by a phosphor screen. The optical technique can use transmitted light or reflected light and the detector is the eye or a camera. TEM is a complex technique and can be used to analyze far more than thickness, including morphology, ordering, defects, composition, and strain. Several texts are available to the reader for understanding fundamentals and applications.<sup>166,167,168</sup>

Cross-sectional samples were prepared by cleaving the sample into two pieces and gluing them together with the film surfaces touching. This sandwich piece is then cut into several smaller samples with a diamond saw. One sample at a time is secured, in cross-section, to a glass disc with wax. The samples are ground and polished by hand into a thin wedge. Additional thinning was performed with an ion mill. Once the sample is adequately thin, it is glued to a metal ring for loading into the microscope. The actual measurements were performed by a trained microscopy expert. XRD measurements were in excellent agreement. An advantage of the TEM analysis is that the individual thickness of each layer can be measured. With XRD, the period is measured which is the sum of the thickness of the two types of layers. The thickness of each layer is estimated by assuming that the growth rate of each layer is similar. TEM measurements indicated that some error results from this assumption. Specific images are presented and discussed in chapter 9.

## 7 DEVICE PROCESSING

Final device structures were processed into individual 2mm x 2mm solar cells with top contact shading of approximately 7%, using an in-house, class 100, modular cleanroom. Basic processing techniques such as photolithography, chemical etching, reactive-ion etching, annealing, and metallization are available. Installation of the cleanroom was prompted by the high cost of using other available facilities where processing a single batch of devices could cost several thousand dollars. With easy access to the cleanroom, approximately 350 solar cells were processed and tested in a relatively short time. Drawing from the vast amount of knowledge available for GaAs processing,<sup>169</sup> a method was developed over several trial runs. The final process flow is listed below and each technique is described in detail in the following sections.

1. Apply photoresist mask to define top contact fingers
2. Deposit top contact metallization
3. Liftoff excess metallization and photoresist
4. Apply photoresist mask to define mesas
5. Chemically etch mesas
6. Remove mesa photoresist
7. Deposit back contact metallization
8. Anneal to enable ohmic contact behavior

## 7.1 PHOTOLITHOGRAPHY

Photolithography is the process of transferring shapes defined on a mask to the surface of a material. Photoresists (PR) are chemicals sensitive to UV light and are first applied to the sample surface by spin-coating. Spin-coating involves placing viscous liquid photoresist onto the sample and spinning at high speed to produce a uniform layer.

Photoresist can be positive or negative. Positive PR becomes more soluble in a developer solution when exposed to UV light, so any exposed regions are removed leaving a positive image of the mask on the surface. Negative PR polymerizes with UV exposure so exposed areas remain while shaded areas are dissolved in a developer leaving a negative image of the mask on the surface. The mask is placed between the UV source and the photoresist to define which regions are exposed. PR essentially protects one region of the sample while some procedure is executed on another region. Typical uses are masks for metal deposition and etching.

A positive resist (Shipley 1813) is used as a metallization mask for the top contact. The device sample is first baked on a hot plate for several minutes at 110°C to drive off any water vapor. Then it is placed in a spin-coating machine where it is held in place by a vacuum chuck. Three to four drops of resist are placed on the sample with an eye-dropper. The sample then spins at 5000RPM for 45 seconds resulting in a uniform PR coating a few microns thick. The sample is returned to the hotplate for a “soft bake” at 110°C for 2 minutes. This evaporates solvents from the PR, making it less tacky which helps with handling. A Karl Suss mask aligner (MJB3) is fitted with the appropriate mask and the sample is loaded underneath. This is a contact mask aligner, so the sample comes in physical contact with mask. Inadequate soft baking will result in the PR sticking to mask,

making it nearly impossible to align and soiling the mask. Conversely, excessive soft baking renders the PR unresponsive to UV exposure, so a proper balance must be found. Once the sample is properly aligned with the mask, it is exposed to UV light for 9.5 seconds. The aligner is equipped with a 200W high-pressure mercury UV light source, calibrated to a power density of  $19\text{mW}/\text{cm}^2$  at the mask surface. The sample is then returned to the hotplate for 1 minute at  $100^\circ\text{C}$  to harden the PR. At this point, the sample would be immersed in a developer solution to remove the unwanted area of PR. However, positive PR does not naturally give the desired undercut for the metallization step. UV light travels through the resist, top to bottom. For a negative resist, the top surface is slightly more polymerized than the bottom surface, so when excess PR is dissolved by the developer a slightly under-cut sidewall remains. For a positive resist, the top surface is more soluble than the bottom surface which results in an over-cut profile. Fortunately, a colleague had already found a way to artificially harden the top surface of the positive PR after exposure, by dipping the sample in toluene. After a 2 minute toluene dip, the sample was dipped in developer for 1 minute, rinsed with DI water, and dried. The result is a surface almost entirely covered by PR with windows to the substrate in the shape of the top contact, ready to receive metallization.

The same positive PR is used as an etch mask for the mesas and the procedure above is repeated. Under-cut is not required for etching, so the toluene dip is omitted. The final product of this step is an array of PR squares which are essentially unresponsive to the etchant chemicals.

## 7.2 METALLIZATION AND LIFTOFF

Metal contacts to semiconductor devices provide a means for connection to an external circuit. Therefore, ohmic behavior with very low resistance is desired to avoid parasitic losses. Placing a metal in contact with a semiconductor usually forms a rectifying, rather than an ohmic, contact. While the basic physics is understood, the application to real systems is largely experimentally driven. In fact, the formation of contacts with ohmic behavior can be so difficult to quantify scientifically that it is sometimes referred to, in jest, as technological art rather than science.

An electron-beam evaporator from Thermionics is used to deposit the top and back metal contacts. Thermal emission of electrons from a tungsten filament is used to heat metals to very high temperatures sufficient for evaporation. The apparatus is equipped with a 3kW power supply for the filament and eight pockets for different metals in a rotating crucible. The pockets are typically populated with Au, AuGe eutectic, Ti, Ni, Pt, Cr, Pd, and Al, but many materials can be evaporated including non-metals. Hot metal vapor condenses on every cool exposed surface in the containing bell jar. The process occurs in high vacuum provided by a turbo-pump. Before loading samples into the evaporator, a 1 minute dip in hydrochloric acid followed by a DI water rinse and drying ensures the surface is clean and free of oxides, to promote metal adhesion. The contacts consist of several layers of different metals deposited in succession by rotating the crucible to select the next source. The evaporator is equipped with a thickness monitor to measure the thickness of each deposited layer. Metallization schemes for both contacts are slightly modified versions of those commonly found in the literature. Only a couple of iterations were required to find

a suitable combination, detailed in Figure 7.1. For all devices processed, the top layer is p-type and the substrate is n-type.

Post-deposition, both the PR and exposed sample areas are coated with metal. Dissolving the PR with acetone lifts off the unwanted metal and leaves behind the contacts. This is where under-cut is critical as it creates a discontinuity in the metal film at the contact edges. Without under-cut, the entire metallization may be removed. Note that the back contact does not require any lithography as it is uniformly deposited.

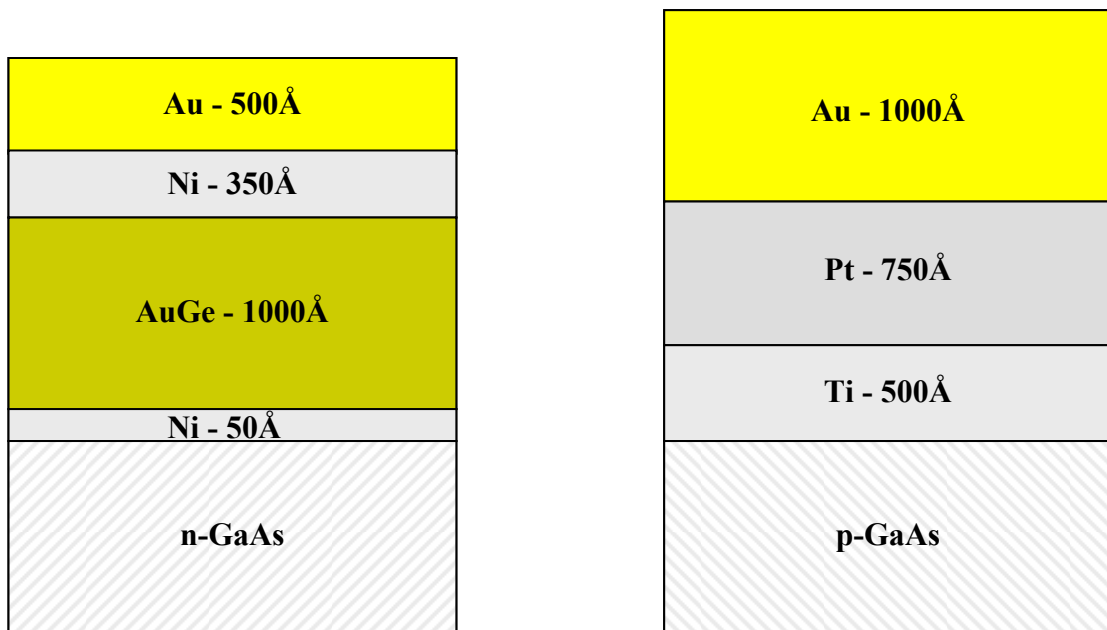


**Figure 7.1** Contact Metallization Schemes

### 7.3 ETCHING

A reactive ion etcher was available, but chemical etching was deemed adequate and more convenient for these devices. Samples masked with PR for mesa etching were etched in three steps. The top GaAs layer was removed by etching in a 3:1:1 solution of

H<sub>2</sub>O:H<sub>2</sub>O<sub>2</sub>:H<sub>3</sub>PO<sub>4</sub> for 2 minutes to expose the AlGaAs window layer. AlGaAs is also typically used as an etch stop in GaAs processing. Samples were removed from the 3:1:1 solution, rinsed with DI water, and etched in HCl for 4 minutes to remove the AlGaAs layer. Samples were again rinsed and returned to the 3:1:1 solution for 5 minutes to complete the mesa etch. A DI water rinse and an acetone rinse to remove the PR, followed by drying with nitrogen, completes the process.

#### 7.4 ANNEALING

An annealing station was constructed from a former OMVPE growth chamber heated with IR lamps. While this setup is not true rapid thermal annealing, the heating rates are similar. A series of annealing studies were performed to determine the best conditions for ohmic contact formation. For the metallizations described above, the lowest contact resistance was measured at annealing conditions of 430°C for 30-40 seconds. This is fortunate in that two separate annealing steps are not required.

## 8 GaAsN

An initial goal of this research was to investigate the growth of dilute nitride alloys and evaluate feasibility for use in photovoltaic applications. It has been reported that  $\text{In}_{0.07}\text{Ga}_{0.93}\text{As}_{0.98}\text{N}_{0.02}$  is lattice matched to GaAs with a bandgap of 1.0eV.<sup>105</sup> This appears to be ideal for the desired third junction, but needs further investigation due to poor material quality. To develop an understanding of the effects of N and required growth parameters, GaAsN films were grown to avoid the added complexity of a quaternary alloy.

Most OMVPE research uses hydrogen( $\text{H}_2$ ) as the primary carrier gas so the reaction occur in a  $\text{H}_2$  ambient environment. The OMVPE system described earlier in this chapter uses nitrogen as the primary carrier gas and hydrogen can be injected as needed. It was discovered that hydrogen plays a significant role in the N incorporation into the film. The large difference in N and As atoms make high N concentrations incompatible with GaAs. The highest reported N concentration in GaAsN using a hydrogen carrier gas is 5.6%.<sup>170</sup> It was noted that samples grown with a nitrogen carrier gas yielded higher N compositions compared to data reported in the literature for hydrogen. We performed a series of experiments where the carrier gas composition was varied over 0-67%  $\text{H}_2$  with a balance of  $\text{N}_2$  with all other parameters held constant. The results, plotted in Figure 8.1 for 600°C growth temperature, demonstrate that higher N composition can be attained by using a nitrogen carrier gas. At a growth temperature of 575°C, the N composition was increased to 8.1%, believed to be the highest reported value to date for OMVPE GaAsN. The details of this experiment were previously published including a discussion of the possible mechanisms responsible for this phenomenon.<sup>152</sup> Similar previous work was found in the

literature after publication and is in agreement with our findings.<sup>157</sup> It is worth noting that a similar effect is reported for In in the InGaN material system.<sup>171</sup>

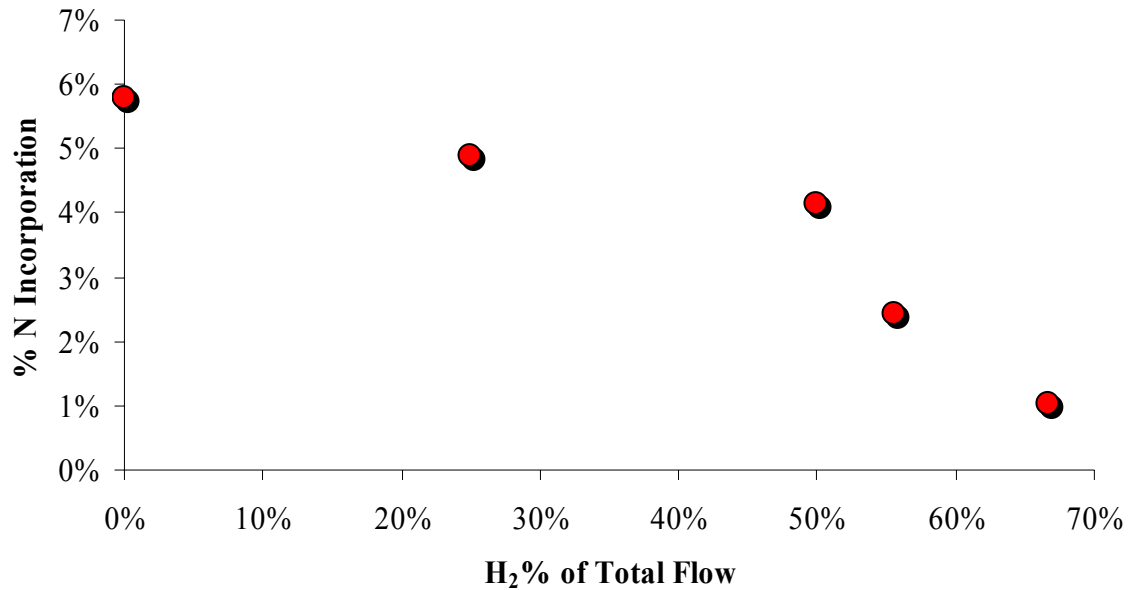


**Figure 8.1** Effect of Carrier Gas on N Incorporation at 600°C

Further analysis of the GaAsN films revealed several trends supporting data found in the literature that are now widely reported. As expected, lower growth temperatures favor higher nitrogen composition as the reaction moves further from equilibrium. This behavior was found to be independent of carrier gas. Results for pure nitrogen and a 50/50 H<sub>2</sub>/N<sub>2</sub> mix are plotted in Figure 8.2.

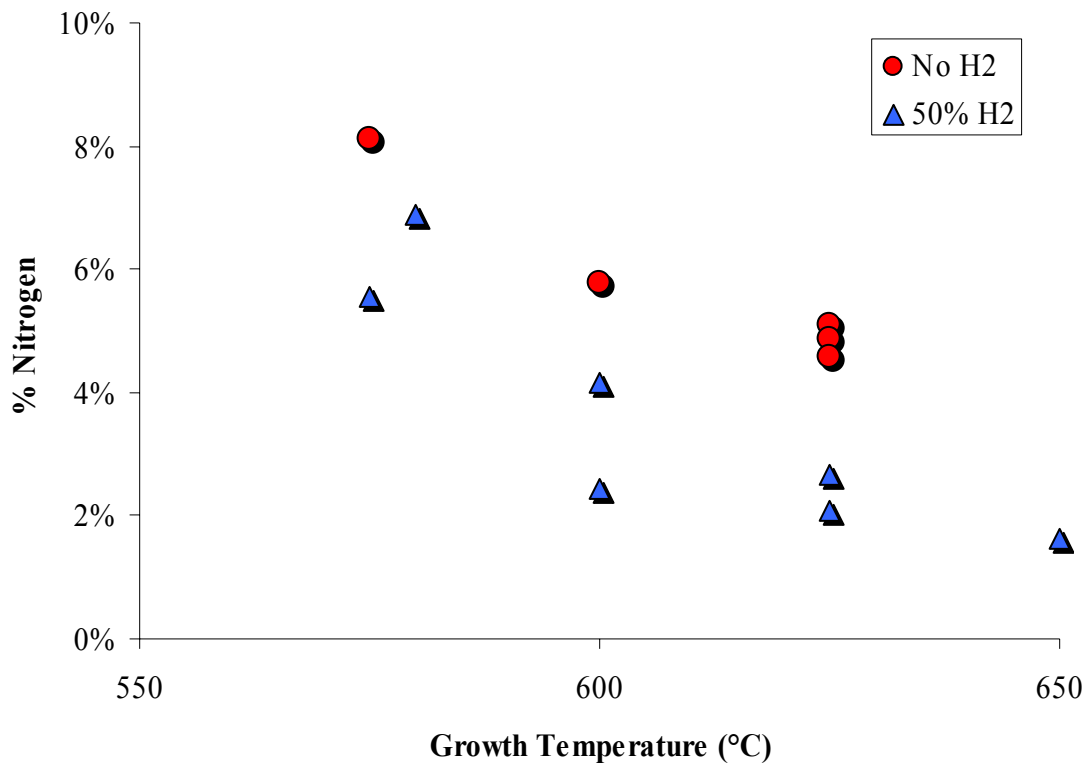


**Figure 8.2** Growth Temperature Dependence of N Incorporation in GaAsN

Several measurements were taken to evaluate the quality of the films. X-ray diffraction and photoluminescence give an good indication of crystal and optical quality, respectively. Each technique is described in Chapter 6 and results from several concentrations are plotted in Figure 8.3 and Figure 8.4 for 600°C. A rapid decrease in film quality with increasing nitrogen composition is evident from both measurements, indicated by low intensity, broad peaks for even small N concentrations. X-Ray diffraction curves are distributed along the y-axis for easier viewing.

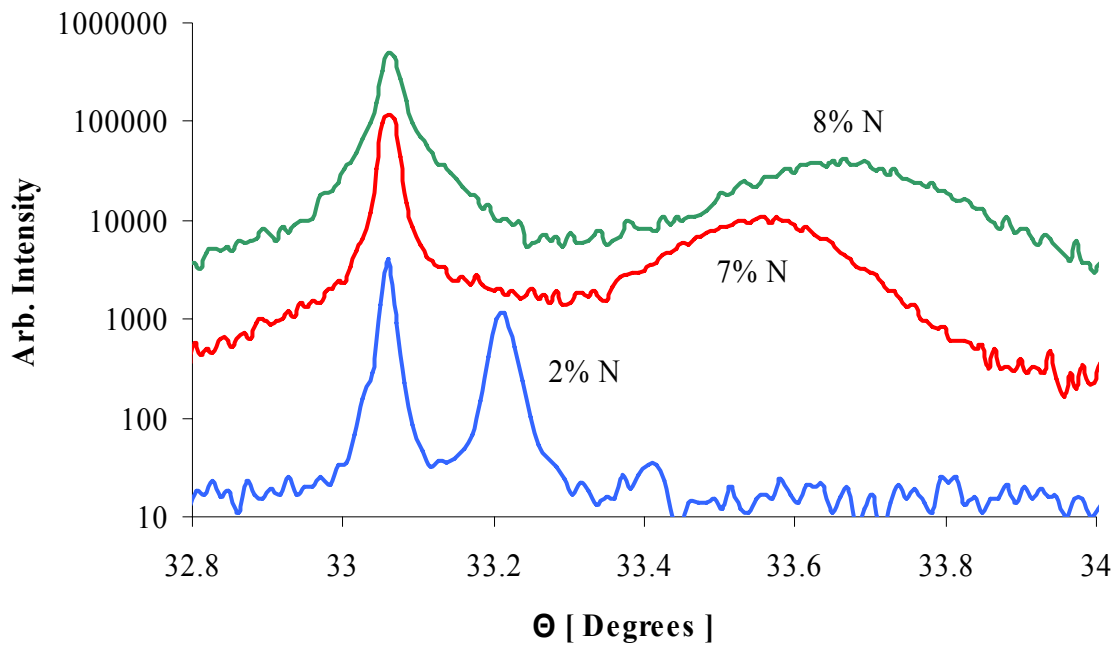


**Figure 8.3** X-Ray Diffraction Data for Various N Compositions in GaAsN

As-grown GaAsN did not exhibit a measurable PL signal. Post growth annealing for 15 minutes at 675°C under N<sub>2</sub> at 700 Torr appeared to restore optical properties to measurable levels. In fact, the need for annealing is widely reported, but is still poorly understood.<sup>101</sup> Annealing likely reduces one or several types of non-radiative centers.<sup>172</sup> Polimeni, et al have demonstrated that annealed GaAsN hydrogenated via ion-beam irradiation returns to a pre-annealed state with poor optical properties.<sup>173</sup> Annealing after hydrogenation again restores optical properties. Polimeni argues that hydrogen forms a complex with and passivates the nitrogen, resulting in drastically reduced optical quality. Annealing can dissociate the H-N complex resulting in restored properties. While convincing, this does not fully account for many other reported defects and the exact nature of the complex remains unknown. Furthermore, our GaAsN films grown without hydrogen

also required annealing, but perhaps sufficient hydrogen is available from precursor decomposition to form H-N complexes even in the absence of a hydrogen carrier gas.

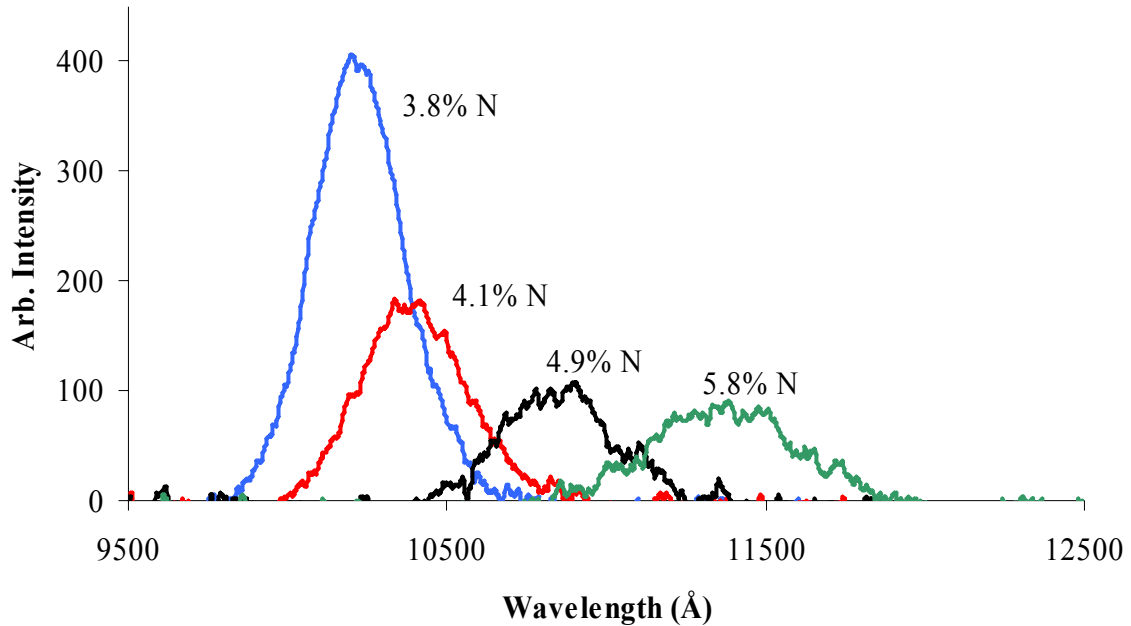


**Figure 8.4** PL Data for Various N Compositions in GaAsN

In addition to these findings, a considerable array of defects have been reported.<sup>174,175</sup> The most discouraging picture for photovoltaic use is that many of these defects are efficient non-radiative recombination centers that severely reduce carrier lifetime, especially for N concentrations above 1%. In terms of photovoltaic applications, InGaAsN suffers from the same problems as GaAsN. The overwhelming evidence of poor material quality has led the author to believe these nitride alloys may not be suitable for solar cells at the required N concentrations. In some respects, it is similar to lattice mismatched material where misfit dislocations reduce carrier lifetime. Alloys containing 1% N or less show promise due to relatively high quality, but must be used in a different

manner since this composition can not be lattice matched to GaAs in a thick 1eV film.

Research continues and solutions may be found, but the current situation warrants pursuit of alternative means such as the structure presented in this work.

## 9 STRAINED LAYER SUPERLATTICE SOLAR CELLS

Progression of this research can be classified by three distinct modes. The first is general investigation into GaAsN in terms of crystal growth and application to PV, as discussed in the previous chapter. Second is to reduce GaAsP barrier thickness while increasing P composition to maintain strain balance. Third is to increase the In composition as high as possible to offset the strain and quantum size effect induced increase in bandgap. These goals are pursued with the knowledge that a small amount of N addition to the structure may be required to achieve the desired bandgap. The following sections contain experimental results and discussion with respect to the degree of success in meeting the goals stated above. Some corollary effects were encountered over the course of this research and are presented as well.

### 9.1 DEVELOPMENT OF THE INGAAS/GAASP SLS

Most of the effort in creating this device involved the SLS. Creating the p and n regions and the window layer follows standard OMVPE procedures and does not warrant further discussion. The general growth conditions are given in Chapter 5. To the best of the author's knowledge, no previous data exists in the literature for the growth of this structure by OMVPE at the target compositions. Consequently, the approach to growing the SLS was to start with relatively low In and P concentrations and thicker wells and barriers. The work by Barnham, et al with InGaAs/GaAsP MQW solar cells<sup>124</sup> serves as a good point of comparison for lower In and P compositions. These layers are relatively easy to produce and are used to establish a baseline for control of thickness, composition, and lattice matching. Once the ratios are understood, composition is increased while thickness is

decreased. As an example of initial efforts to produce this structure, consider the XRD scans in Figure 9.1. The lower curve is for a GaAs/GaAs<sub>0.76</sub>P<sub>0.24</sub> SLS with nominally 91Å GaAs and 45Å GaAsP layers. The middle curve is for a In<sub>0.12</sub>Ga<sub>0.88</sub>As/GaAs SLS with equal 131Å layers. Note the n = 0 peak is shifted to the right or left of GaAs, indicating 0.28% and 0.45% lattice mismatch, respectively. Individual layers are below the respective CLT's, 136Å for GaAsP and 140Å for InGaAs. However both SLS's are ~5000Å thick and exceed the overall CLT, 520Å for GaAs/GaAsP and 328Å for InGaAs/GaAs.. Characteristic tensile or compressive cross-hatching was observed from optical micrographs in Figure 9.2. Growing a series of these binary-ternary structures, with varying composition and thickness, develops an understanding of the InGaAs and GaAsP layers individually. The layers are then combined into a InGaAs/GaAsP SLS and tweaked to achieve lattice matching

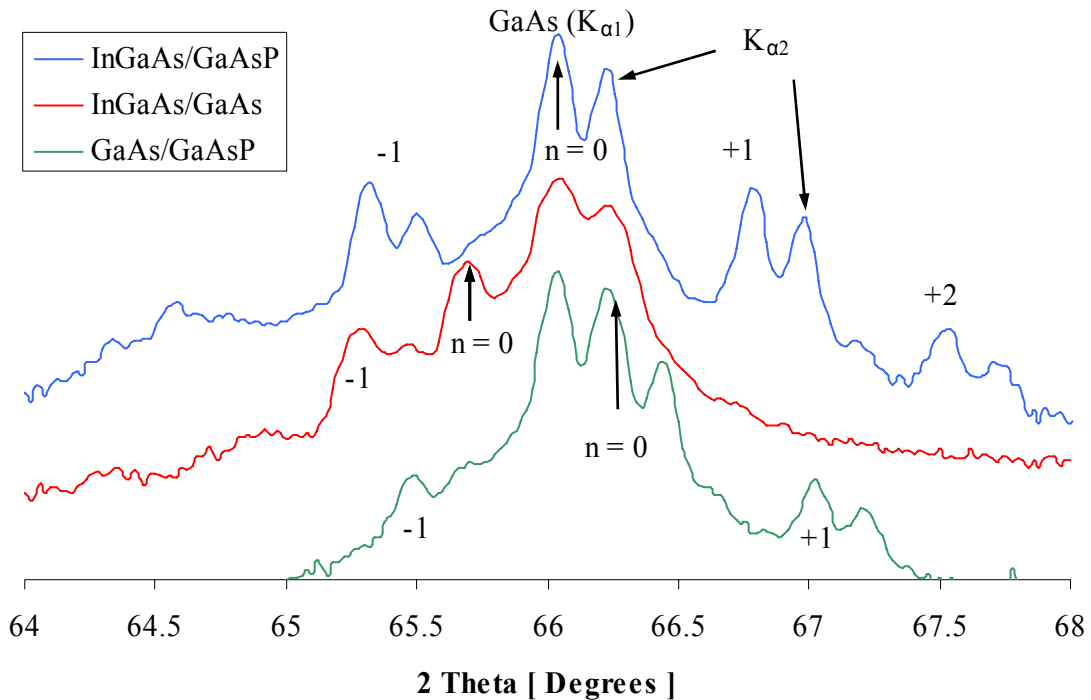


**Figure 9.1** XRD for Strained GaAs/GaAsP and InGaAs/GaAs and Strain Balanced InGaAs/GaAsP SLS's

. The top curve in Figure 9.1 is for a  $\text{In}_{0.1}\text{Ga}_{0.9}\text{As}/\text{GaAs}_{0.76}\text{P}_{0.24}$  SLS with 75Å InGaAs and 69Å GaAsP.  $n = 0$  is aligned with the GaAs substrate peak, indicating a close lattice match. These values are near the calculated relationship for lattice matching, given in equation 4.2. No cross hatching was observed for this surface in the middle micrograph of Figure 9.2.

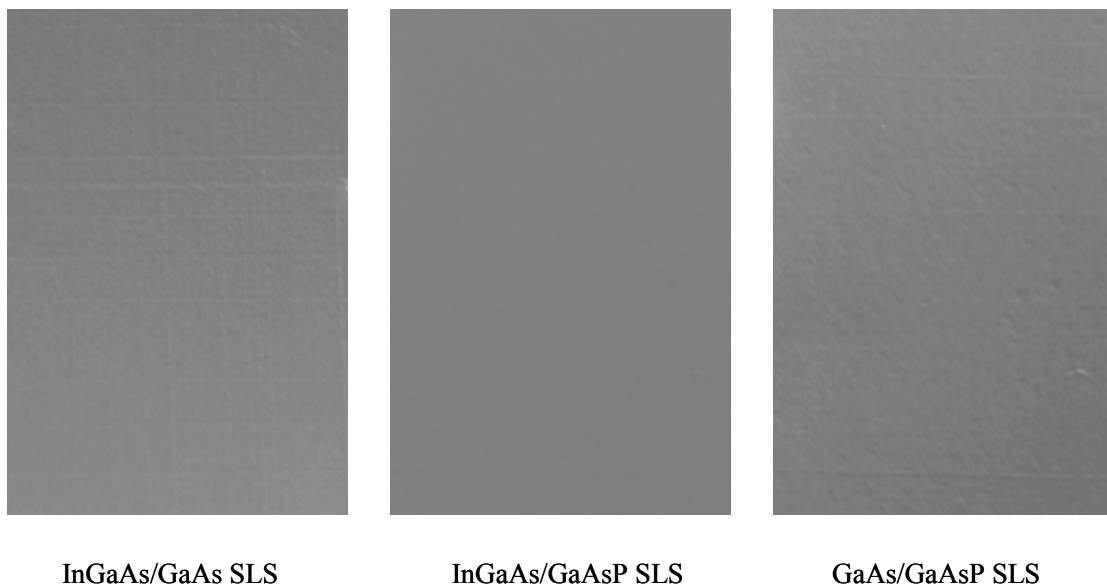


**Figure 9.2** Optical Micrographs of Surfaces Corresponding to Each Sample in Figure 9.1

Reported composition values for the SLS layers are assumed from bulk film measurements as described in section 6.2. Thickness values of these thin layers can only be approximated from XRD from the overall growth rate and the period. The average growth rate was first assumed to be the same for both InGaAs and GaAsP, with the understanding that for higher In concentrations the increase in growth rate of InGaAs may not be negligible. TEM measurements were made to verify this assumption for a

$\text{In}_{0.14}\text{Ga}_{0.86}\text{As}/\text{GaAs}_{0.25}\text{P}_{0.75}$  test sample with  $79\text{\AA}$  wells and  $29\text{\AA}$  barriers as estimated from XRD calculations alone. The TEM measurements indicated that InGaAs is roughly 5% thicker( $83\text{\AA}$ ) than our approximation and GaAsP is accordingly thinner( $28\text{\AA}$ ). Incorporating this into the collected thickness data brings the thickness ratios into very close agreement with the calculated values for lattice matching by equation 4.1. The representative TEM image in is adequate for thickness determination, but the samples would need to be prepared with a more sophisticated technique for more detailed analysis. The wedge angle is at least  $13^\circ$ , which reduces the area that is sufficiently thin for electron transparency.

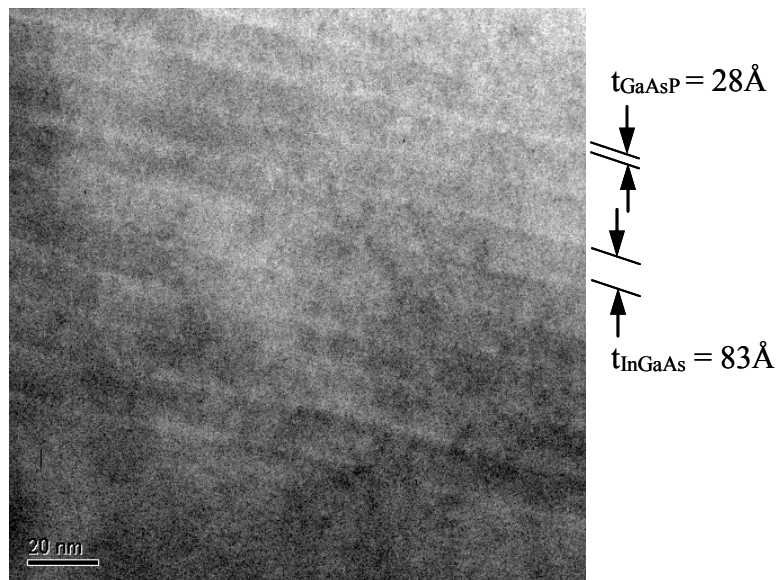


**Figure 9.3** TEM of InGaAs/GaAsP SLS

Increasing In composition for bandgap reduction requires a reduction in layer thickness to remain below the CLT. Reducing the barrier thickness requires a corresponding increase in P composition. Lower growth temperatures favor higher In content while higher growth temperatures are typically used for high P content. As compositions increase, the growth window for high quality material gets progressively smaller due to this competition.

Broader, less defined satellite peaks were observed for thinner layers, demonstrated in Figure 9.4. The test specimen is nominally  $\text{In}_{0.14}\text{Ga}_{0.86}\text{As}/\text{GaAs}_{0.25}\text{P}_{0.75}$  and 83Å and 28Å, respectively. Critical layer thickness is 115Å for  $\text{In}_{0.14}\text{Ga}_{0.86}\text{As}$  and 30Å for  $\text{GaAs}_{0.25}\text{P}_{0.75}$ . The peaks profiles are partially due to the fact that the peak spacing increases and intensity decreases naturally with decreasing layer thickness. However, this may also indicate a well/barrier interface morphology modulation. While this is detrimental to devices that gain efficiency from quantum confinement, such as QW lasers or LED's, slightly diffuse interfaces could benefit the solar cell device. Poor confinement may promote carrier escape from the well and moderate the quantum size effect, providing lattice matching is retained. A natural consequence of the step flow growth mechanism is retained atomic steps at the interface. Steps are continuously advancing across the surface with new layers nucleating to form the next step. When growth is switched to the next film composition, it conforms to the steps so the interface can not be atomically sharp unless special growth techniques are used to minimize the number of incomplete steps. It is also well known that two or more steps may bunch together at some growth conditions to advance in a lower energy growth mode.<sup>145</sup> The effects of these small perturbations may be negligible for thick films, but the influence is increased for thin films as the dimension of the steps may be a significant fraction of the thickness. Step bunching may also have macroscopic effects for multi-layer structures, far beyond a slightly diffuse interface. Large super-steps can induce a wavy growth pattern driven by elastic strain, especially for a high number of periods. This has been demonstrated in the  $\text{InGaAs}/\text{GaAsP}$  system<sup>176</sup> as thermodynamic step bunching dominating kinetic bunch suppression.<sup>177</sup> This effect is undesirable because it can interrupt the periodic structure to the extent that well and barrier layers overlap. The large variation

mis-aligns strain fields so strain balance may not be achieved across the whole structure. Fortunately, reduced growth temperatures appear to mitigate this problem and are already required for this structure.

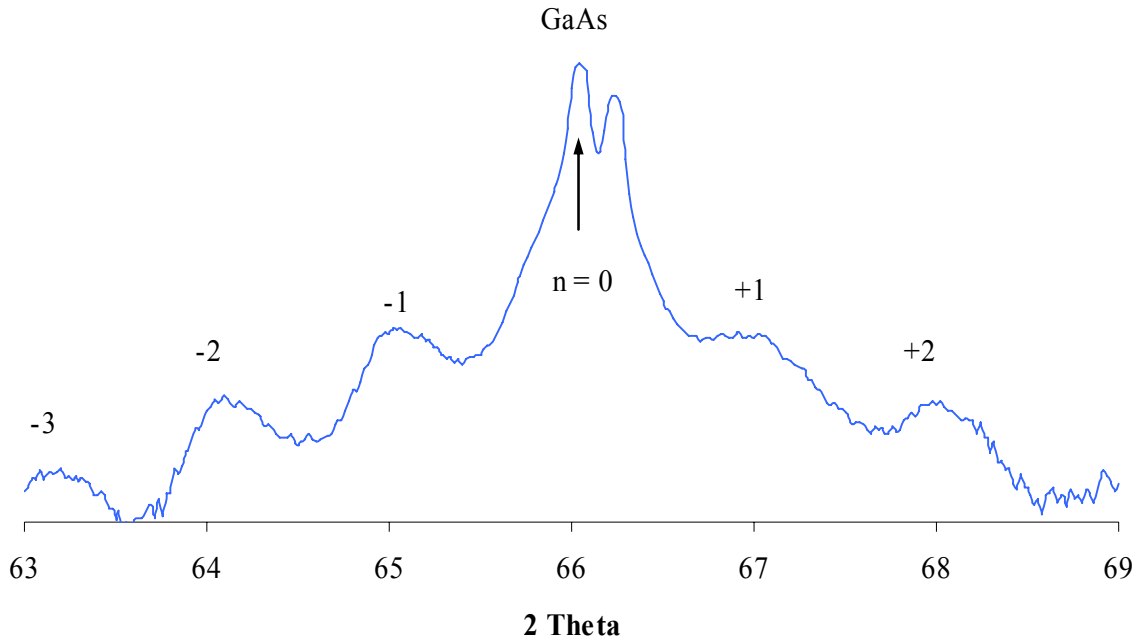


**Figure 9.4** XRD for an  $\text{In}_{0.14}\text{Ga}_{0.86}\text{As}/\text{GaAs}_{0.25}\text{P}_{0.75}$  SLS with 83Å Wells and 28Å Barriers

Attempts to increase P composition above ~75% by increasing TBP flux were unsuccessful. Switching off the TBA flow during the GaAsP layer was considered to achieve GaP barriers. However, this was deemed unlikely to be successful due to the volatility of the group V species. Constant TBA flux through growth of both layers ensures there is no interruption of As overpressure. Attempting to alternate In and As with P is very likely to result in unpredictable compositional fluctuations which could disrupt strain balancing. Additionally, it is known that group V atoms are retained on the surface after switching.<sup>145</sup> Given the small thickness of the barrier layer, As will still be incorporated through the film. The decision was made to reduce the TBA flux by 50% for both SLS

layers as the growth time is too short to reliably ramp the flow to a different point for each layer and two independent TBA sources were not available. Reducing the TBA flow risks impairing InGaAs quality. Several re-calibrations were made with the reduced TBA flow which indicated good InGaAs quality and an increase in P composition to approximately 90%.

An increase of P composition to 90% allowed barriers to be thinner. XRD data from the Rigaku machine became difficult to discern, so the more sensitive Philips system was used for samples with thinner barriers. Both XRD tools are described in section 6.2. The best lattice matched structure achieved, in terms of high In and P compositions with thinnest barriers, is  $\text{In}_{0.28}\text{Ga}_{0.72}\text{As}/\text{GaAs}_{0.1}\text{P}_{0.9}$  at  $38\text{\AA}$  and  $23\text{\AA}$ , respectively. Figure 9.5 is an XRD scan of this sample. For comparison, the calculated CLT is  $47\text{\AA}$  for  $\text{In}_{0.28}\text{Ga}_{0.72}\text{As}$  and  $25\text{\AA}$  for  $\text{GaAs}_{0.1}\text{P}_{0.9}$ .

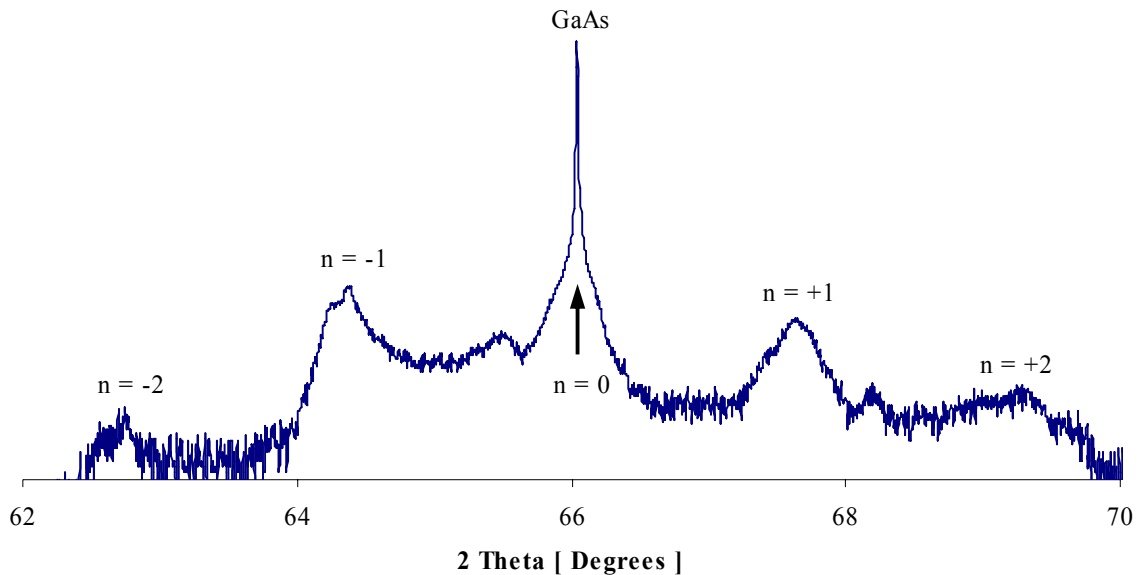


**Figure 9.5** XRD for an  $\text{In}_{0.28}\text{Ga}_{0.72}\text{As}/\text{GaAs}_{0.1}\text{P}_{0.9}$  SLS with  $38\text{\AA}$  Wells and  $23\text{\AA}$  Barriers

Bandgap reduction for initial structures was verified by room temperature photoluminescence measurements and compared to the theoretical calculations presented in section 4.3. The results for several representative test structures are plotted in Figure 9.6. For lower In compositions, experimental values agree with calculated values within the error of determining the values for composition and thickness. At 18% In some deviation is observed which may be attributed to interface effects. The model simulates the periodicity of the structure, but does not include information about the interface. Also, many ternary parameters are interpolated from binary data which may introduce error for compositions further away from the binary endpoints. Measurement of bandgap reduction below  $\sim 1.2\text{eV}$  was not possible with this PL system. The particular photomultiplier tube that was available has an exponential decrease in sensitivity for longer wavelengths. However, at this point the basic behavior of the system has been measured up to 60% of the target In composition. Readily available device processing facilities and spectral response testing offer an alternative method. Spectral response measurements, as described in section 6.5, have somewhat less resolution than PL, but are ultimately the more important performance metric.

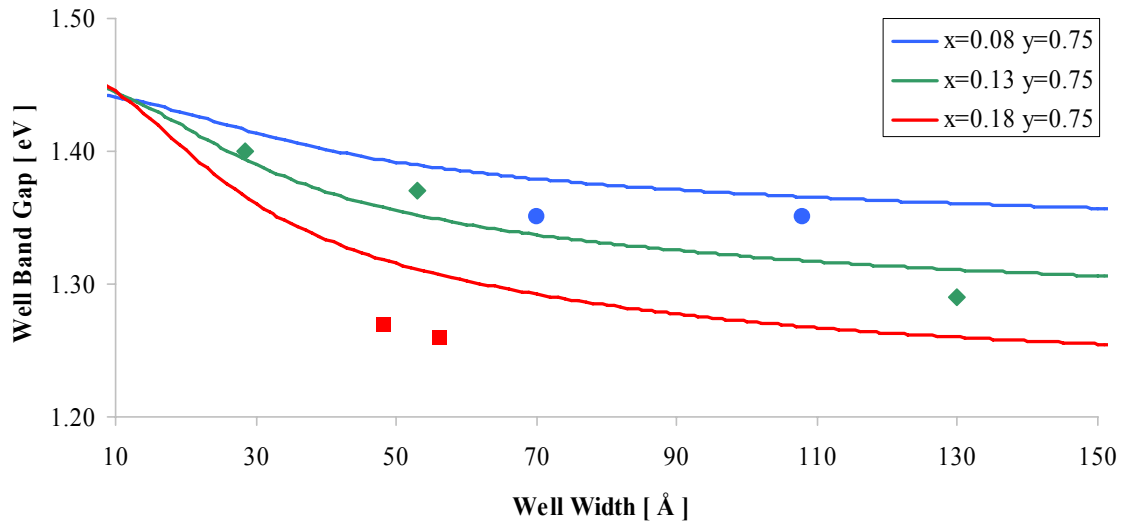


**Figure 9.6** PL for Various Compositions and Well Widths (Experimental data points are color coordinated with the corresponding calculated curves)

In order to utilize the SLS structure as an i-region in a p-i-n diode, it is important to verify the doping level. Hall effect measurements were performed, as described in section 6.4, to determine carrier concentration in  $\text{In}_{0.28}\text{Ga}_{0.72}\text{As}/\text{GaAs}_{0.1}\text{P}_{0.9}$  SLS samples. Measured samples were p-type and carrier concentration values ranged over  $2\text{-}5 \times 10^{15} \text{ cm}^{-3}$ .

Dissociation of TMG is a well known source of carbon in III-V semiconductor growth which is a p-type dopant for InGaAs and GaAsP. The light background doping measured by Hall is most likely due to incorporation of carbon from TMG. A truly intrinsic material would be too resistive and contribute to the series resistance of the device, so the measured low level of unintentional doping is desired.

## 9.2 DEVICE PERFORMANCE

Once developed, the SLS structure is inserted as the i-layer of a p-i-n diode to test overall solar cell performance. Current-voltage measurements were made under various

conditions to correlate effects of barrier and well thickness and composition. A generic test structure is given in Figure 9.7. An AlGaAs window layer is used to reduce surface recombination and is capped with a heavily p-doped GaAs layer for ohmic contact formation. Aluminum composition is estimated to be around 20% from the TMAI fraction of the total column III flux (TMG + TMAI). No anti-reflective coating was applied. Compositions are nominally 28%In for all devices tested and either 75% or 90% P. CLT for GaAsP was the limiting parameter for film thickness. GaAsP is near the CLT and the InGaAs thickness is then governed by strain balance. A GaAs pn-junction with identical doping profiles was used as a control for the testing.

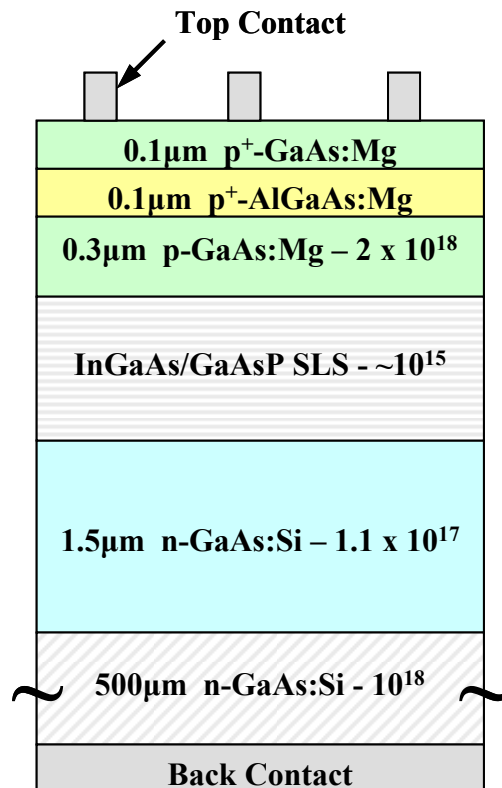


**Figure 9.7** Typical Final Test Structure (SLS thickness ranged from 0.3μm to 0.8μm)

### 9.2.1 Light and Dark Current

Open circuit voltage and short circuit current values were determined from current-voltage measurements under 1 Sun AM1.5D illumination and corrected for 7% shadowing of the top contact. Of course,  $V_{OC}$  is limited by the contact potential which in turn is less than the bandgap voltage,  $E_g/q$ . Accordingly, all measured values of  $V_{OC}$  were well below 0.9eV. Generally, many devices exhibited short circuit current values less than the reference cell. Only devices with the thinnest barriers were able to surpass the  $I_{SC}$  of the control cell. Light I-V curves for four representative devices (A, B, C and D) and for the reference junction are plotted in Figure 9.8. Sample A has an SLS of  $In_{0.28}Ga_{0.72}As/GaAs_{0.25}P_{0.75}$  with 30 periods with 40Å wells and 30Å barriers. Sample B has an SLS of  $In_{0.28}Ga_{0.72}As/GaAs_{0.25}P_{0.75}$  with 50 periods with 40Å wells and 30Å barriers. Samples A and B have a total SLS thickness of 0.2µm and 0.35µm, respectively. Comparing samples C and D, compositions and barrier and well thicknesses are equal, but C has 50 periods(0.3µm) and D has 100 periods(0.6µm). In general, C and D have higher  $I_{SC}$  and thinner barriers than A and B which supports the assumption that tunneling is a significant mode of carrier transport. The low current in A and B may be largely due to efficient recombination of localized carriers in the well. However, recombination does not solely dominate the devices since the additional periods in B increase the current. While the current of C and D are enhanced relative to the control cell, fill factor is significantly reduced. The parameter values for these devices are summarized in Table 9.1.

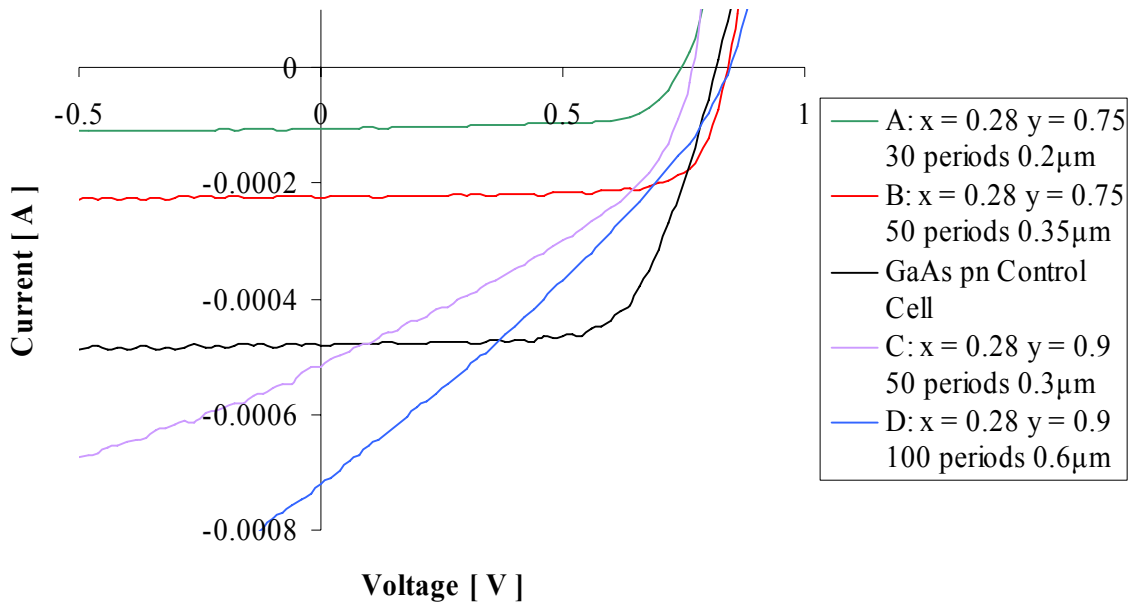


**Figure 9.8** AM1.5D 1-Sun Light Current of Selected Test Cells A, B, C and D Compared to GaAs Control Cell (A:  $\text{In}_{0.28}\text{Ga}_{0.72}\text{As}/\text{GaAs}_{0.25}\text{P}_{0.75}$ , 30 periods,  $0.2\mu\text{m}$ , B:  $\text{In}_{0.28}\text{Ga}_{0.72}\text{As}/\text{GaAs}_{0.1}\text{P}_{0.75}$ , 50 periods,  $0.35\mu\text{m}$ , C:  $\text{In}_{0.28}\text{Ga}_{0.72}\text{As}/\text{GaAs}_{0.1}\text{P}_{0.9}$ , 50 periods,  $0.3\mu\text{m}$ , D:  $\text{In}_{0.28}\text{Ga}_{0.72}\text{As}/\text{GaAs}_{0.1}\text{P}_{0.9}$ , 50 periods,  $0.3\mu\text{m}$ )

Plotting the dark current for the same samples (Figure 9.9) reveals a significant decrease in dark current for A and B relative to the reference cell. This could indicate a deficiency in the control cell, but it is unlikely as the control cell material was grown in the same reactor with identical doping profiles. For A and B, the dark current can be fitted to the dark current term of equation 2.9 with an ideality factor,  $n \sim 2$ . This is typical of a device dominated by Shockley-Read-Hall(SRH)<sup>178,179</sup> type recombination. It is assumed that increasing the number of barrier layers will serve to increase dark current by increasing recombination in the deep wells such that the wells dominate the dark current. This assumption is not consistent with the reduced dark current in samples A and B. In high quality bulk semiconductor devices, the dark current is primarily determined by lowest energy gap.<sup>180</sup> Apparently, the GaAsP barriers must also influence recombination to

decrease dark current. Connolly, et al have reported simulations to show that the high bandgap of the barrier material in this type of structure may, in fact, be responsible for reduced dark current.<sup>181</sup>

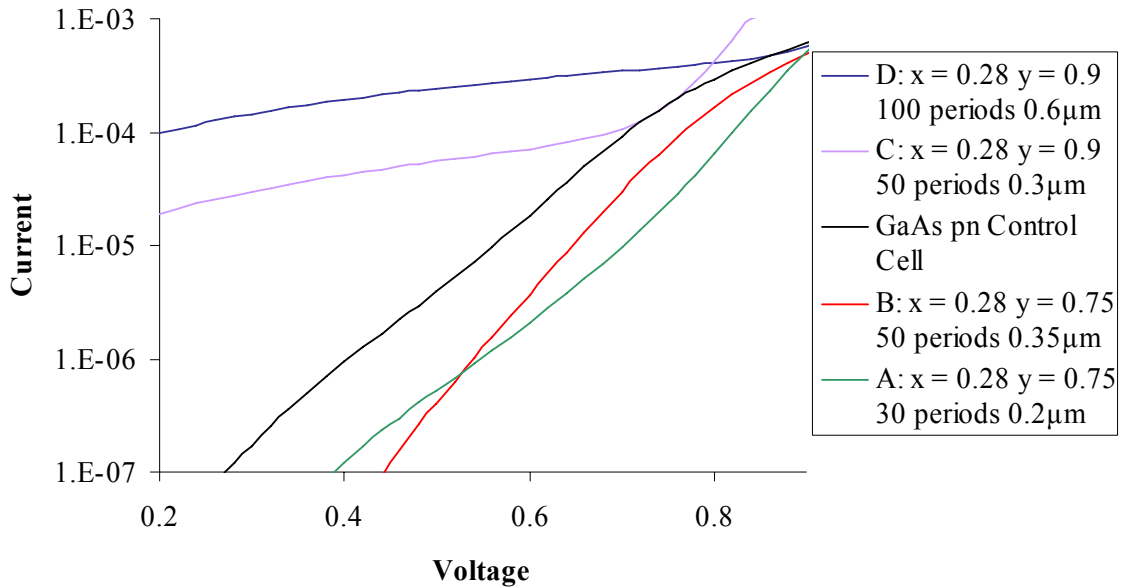


**Figure 9.9** Dark Current for Test Cells in Figure 9.8

Comparing samples A and B or C and D, the dark current is somewhat increased for a higher number of periods. However, the i-layer width is also increased which can increase recombination. It is uncertain if additional periods or increased i-layer width is more responsible for the observed dark current increase. Since B and C have the same number of periods and similar i-layer widths, the particular characteristics of the barriers must also play a significant role to explain the high dark current in C. Ekins-Daukes, et al<sup>182</sup> attribute some decrease in the dark current in InGaAs/GaAsP MQW's relative to GaAs to the higher bandgap of GaAsP as in reference [181]. However, they also observe a large increase in dark current as well depth increases, which may explain the increased dark current in our devices.

For D, the total SLS thickness is increased which effectively extends the depletion over a larger volume. Increasing the i-layer width where electron and hole populations are similar, increases the rate of SRH recombination. This effect combined with the expected dark current increase from additional periods can explain a significant increase in the dark current. It was not possible to estimate the magnitude of each effect individually with the range of samples tested or if the two effects are sufficient to account for the very large observed dark current. The large increase in ideality factor is not clearly understood at this time, but is attributed to unknown recombination events in the SLS as all parameters are similar across devices.

**Table 9.1** Performance Parameters for Test Cells Under AM1.5D Illumination

Sample	V <sub>oc</sub> [ V ]	J <sub>sc</sub> [mA/cm <sup>2</sup> ]	FF	η
pn-reference	0.82	12.03	0.67	8.56%
A	0.74	2.63	0.71	1.80%
B	0.84	5.60	0.75	4.59%
C	0.78	12.1	0.40	4.93%
D	0.84	18.0	0.31	6.01%

In an attempt to verify the assumption that the field across the i-layer is needed to promote carrier transport, samples very similar to B and D were lightly doped in the SLS region to  $\sim 5 \times 10^{16} \text{ cm}^{-3}$ . The I-V characteristics are plotted in Figure 9.12. Sample E

corresponds to undoped B, and F and G correspond to undoped D. All 50 periods are doped n-type for sample E, half the periods are doped n-type for sample F, and G is a p-n junction. In all cases, a large reduction in  $I_{SC}$  is observed along with a reduction of  $V_{OC}$ . The field across the i-region must be important for carrier escape from the wells. The charged impurities effectively screen the field resulting in low current generation. In the absence of a field across the SLS, efficiency of carrier escape from the wells is greatly reduced.

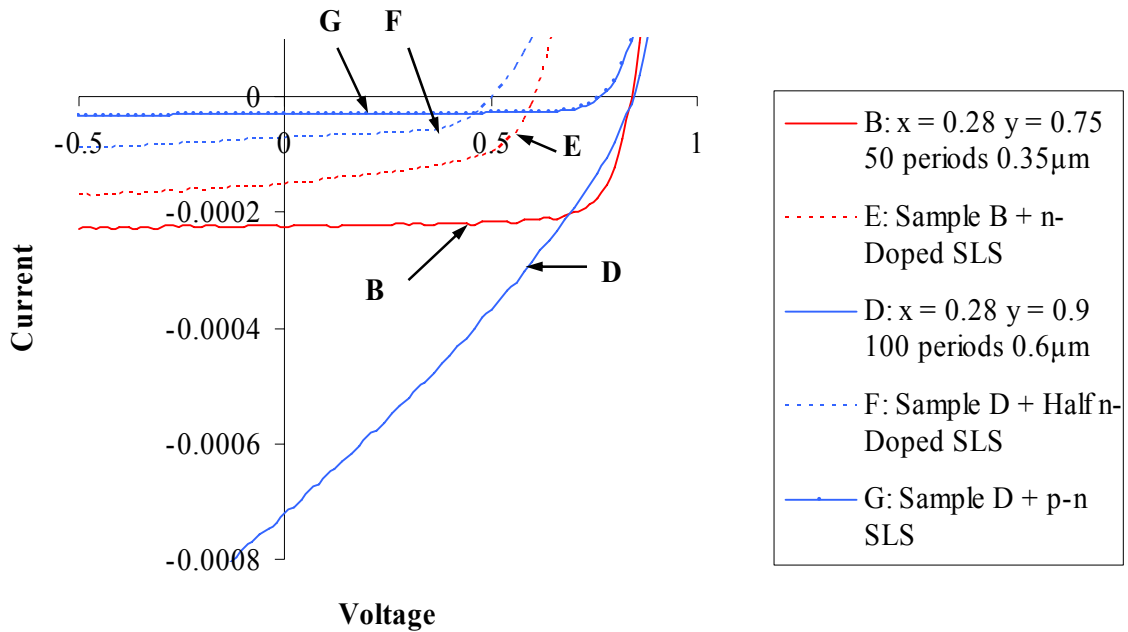
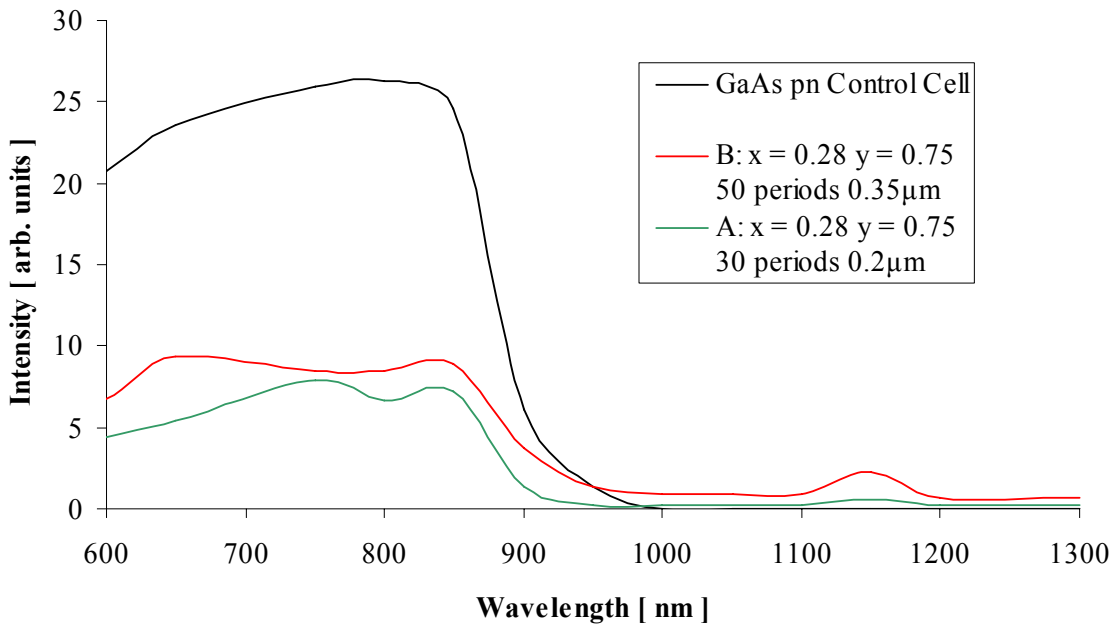


Figure 9.10 I-V of Doped SLS Devices (Dashed lines indicated reduced  $I_{SC}$  and  $V_{OC}$  typical of doped structures. The corresponding undoped sample is plotted as a solid curve with matching color.)

### 9.2.2 Spectral Response

Current-voltage measurements were repeated with a series of bandpass filters sequentially inserted in the illuminating beam of the solar simulator as described in section

6.5. All tested cells with InGaAs/GaAsP SLSs displayed extended absorption range compared to GaAs, with a cutoff around 1150nm or 1.1eV. The expected difference in the quantum size effect for 75% and 90% P compositions is about 0.005eV or 4nm. Since each optical filter covers a range of 20-30nm, resolution of this measurement is not sufficient to detect such small variations. Spectral response from samples A and B of the previous section are plotted in Figure 9.11, compared to the reference cell. Current is predominantly generated in the doped regions and there is a small contribution from the SLS. However, the contribution from the SLS in B is significantly enhanced compared to A.



**Figure 9.11** Spectral Response of Samples A(Green) and B(Red) Compared to the Reference Cell(Black)

Spectral response from samples C and D is plotted in Figure 9.12, for comparison to the reference cell. Clearly, the increased light-current can be attributed to extending the absorption edge beyond GaAs. Applying our bandgap model, the bandgap should be around

1.2eV or 1030nm, but is observed near 1.1eV or 1150nm. The additional peak near 950nm is likely due to transitions from a second bound hole state,  $E_{V,2}$ , (See Figure 4.7) and is calculated to be around 880nm. This further confirms that the model consistently overestimates quantum size effect for higher compositions and thinner layers as already indicated by PL data. (see Figure 9.6) Comparing the areas under the curve, above and below the GaAs absorption cut-off ( $\sim 870$ nm) gives an estimation of the net improvement. For sample D, the current contribution from the SLS region represents about 15% of the total current.

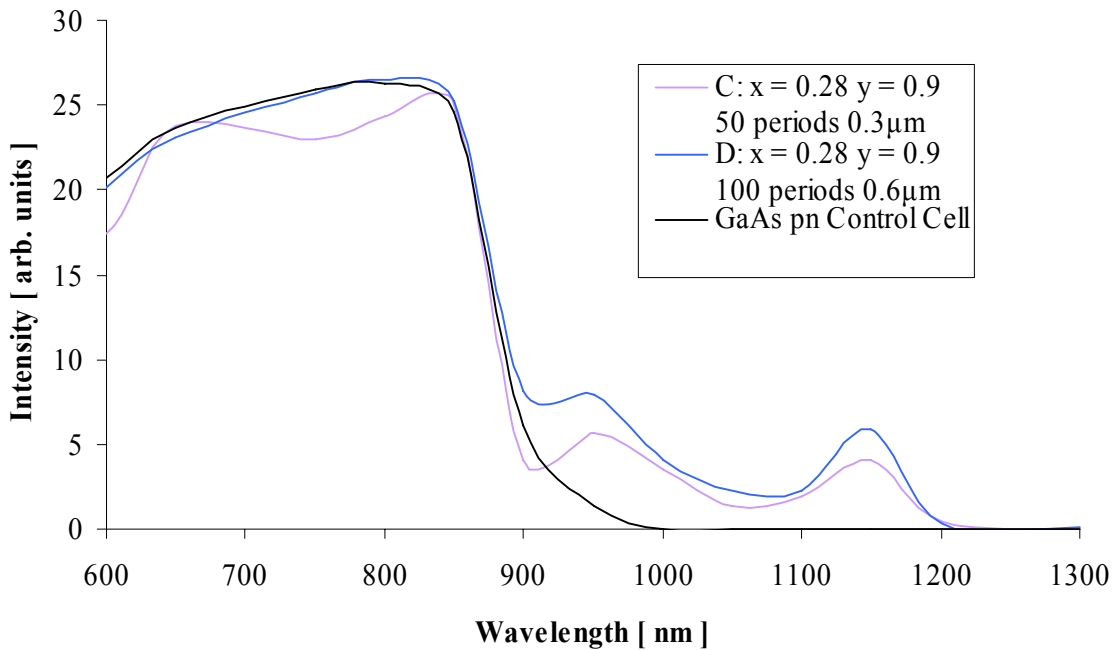


**Figure 9.12** Spectral Response of Highest Light-Current Cell and Reference GaAs Cell

### 9.2.3 Carrier Transport

The exact nature of carrier transport in the SLS region is not exactly known. (See section 4.3.4 for a general discussion of carrier transport in a SLS) However, several

estimates can be made to gain an understanding of the possible mechanisms. Preliminary calculations for InGaAs/GaAsP at relatively low In and P concentrations were made prior to successful device fabrication and a full discussion was previously published by Bedair, et al.<sup>183</sup> These results are summarized here and then refinements are presented with respect to the realized devices. Compositions of  $\text{In}_x\text{Ga}_{1-x}\text{As}/\text{GaAs}_{1-y}\text{P}_y$  considered initially were  $x = 0.1, 0.15, 0.2$  and  $y = 0.2, 0.3, 0.4$  with equal layer thickness and lattice matching at  $y = 2x$ . Internal quantum efficiency (IQE) represents the probability that photogenerated carriers are collected before recombination occurs. For a high IQE, carrier escape time from the well must be much shorter than recombination lifetime. Otherwise, carriers will simply recombine before escape can occur. From the combined work of several authors (see references in Ref. <sup>(183)</sup>) IQE can be approximated as

$$IQE = \frac{\frac{1}{\tau_e}}{\frac{1}{\tau_e} + \frac{1}{\tau_r}} \quad [ 9.1 ]$$

where  $\tau_e$  is the carrier escape lifetime and  $\tau_r$  represents recombination lifetime. To achieve IQE near 100%, the condition where  $\tau_r \gg \tau_e$  must be true. Both radiative and non-radiative recombination was assumed to be important for establishing  $\tau_r$ . Values of  $\tau_r$  reported from AlGaAs/GaAs QW's are around 1-10ns at room temperature.<sup>184</sup> Bedair assumed a conservative value of 1ns was for InGaAs/GaAsP. For the stated compositions at equal 100Å well and barrier thickness, thermionic emission was demonstrated to be the probable primary escape process with IQE approaching 100%.

Continuing this analysis in terms of the best device presented in this chapter,  $\text{In}_{0.28}\text{Ga}_{0.72}\text{As}/\text{GaAs}_{0.1}\text{P}_{0.9}$  SLS (Sample D), can reveal likely trends for carrier transport. A schematic of the band structure of the SLS is given in Figure 9.13.

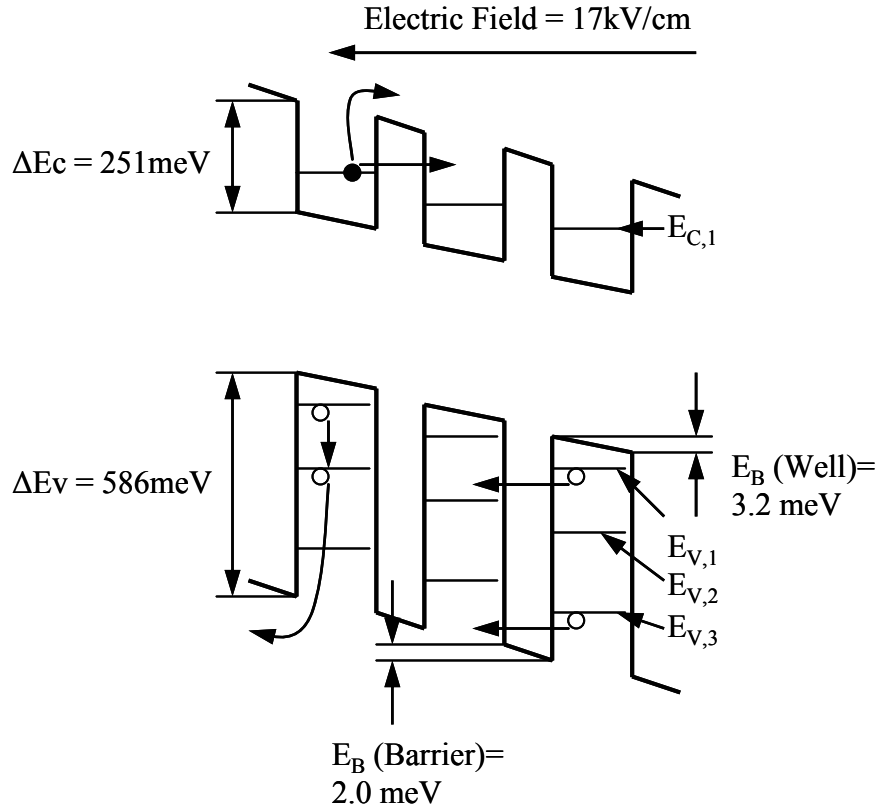


**Figure 9.13** Partial Band Diagram for  $\text{In}_{0.28}\text{Ga}_{0.72}\text{As}/\text{GaAs}_{0.25}\text{P}_{0.75}$  SLS with 38Å Wells and 23Å Barriers

For this structure thermionic emission is expected to be reduced due to deep wells and tunneling to be increased due to thin barriers, compared to the structure discussed in reference <sup>183</sup>. Thermionic emission lifetime is primarily determined by the barrier height over which the carrier must be emitted. Schneider and von Klitzing<sup>185</sup> have derived the following expression for thermionic emission lifetime,  $\tau_{TH}$ , in quantum well structures

$$\frac{1}{\tau_{TH}} = \left( \frac{k_B T}{2\pi m^* L_W^2} \right)^{1/2} \exp\left( -\frac{E_B}{k_B T} \right) \quad [9.2]$$

where  $E_B$  is the field dependent barrier height for either holes or electrons, calculated from

$$E_B = \Delta E_i - E_{i,1} - \frac{|e|FL_W}{2} \quad [9.3]$$

where  $F$  is the field and  $i$  = conduction or valence band. Applying this equation to our samples for an estimated field of 17kV/cm (see section 4.3.4),  $\tau_{TH}$  for electrons is only 22ps for electrons, but  $5 \times 10^7$ ps for holes from the first bound state in the valence band,  $E_{V,1}$ . The other two bound valence states are far enough away from the ground state that the band edge effective masses are not accurate, but the calculation is repeated for these as a rough approximation.  $\tau_{TH}$  for  $E_{V,2}$  is calculated as  $1 \times 10^5$ ps and  $E_{V,3}$  is 85ps. Carriers may be thermally excited to these levels and then emitted or they may also tunnel from these two levels. Once carriers are emitted, recapture to an adjacent well is likely. Experimental values for recapture lifetime in QW structures are less than 1ps<sup>186</sup> so this is expected to be a dominant mechanism and carriers will traverse many barriers before collection.

Tunneling lifetime for a single QW is estimated by the following equation presented by Fox, et al<sup>141</sup>

$$\frac{1}{\tau_{TN}} = \frac{n\hbar\pi}{2L_W^2 m_W} \exp\left[ -\frac{2L_B \sqrt{2m_B E_B'}}{\hbar} \right] \quad [9.4]$$

where  $L_W$  and  $L_B$  are the well and barrier widths,  $m_W$  and  $m_B$  are the effective masses in the well and barrier, and  $E_B'$  is the effective barrier height.  $\tau_{TN}$  for electrons is 0.1ps and is 8ps for holes at  $E_{V,1}$ . Estimated tunneling lifetime at  $E_{V,2}$  is 1.6ps and at  $E_{V,3}$  is 0.3ps.

From these simple calculations, electron escape from the wells is expected to be efficient by either tunneling or thermionic emission, assuming our estimate for a 1 ns recombination lifetime is valid. Considering only emission from  $E_{V,1}$ , the  $5 \times 10^7$  ps lifetime is far beyond any reasonable recombination lifetime, which means that thermionic emission can not be the primary mechanism of hole escape. Low tunneling lifetime of 8 ps for holes at  $E_{V,1}$  indicates that this is the more probable escape mechanism for holes. Setting this value equal to  $\tau_e$  in equation 9.1 and assuming a value of 1 ns for  $\tau_r$ , yields IQE = 99.2%. It should be noted that the tunneling lifetime calculations are for a single QW, and carriers in the SLS are likely to encounter many wells before collection in the bulk regions due to a very low recapture lifetime. Since IQE represents the probability of an escape event and our calculation for tunneling lifetime only accounts for a single well, the actual IQE should be proportional to the product of IQE for all wells. This can be represented by  $\text{IQE}_{\text{total}} = (\text{IQE}_{\text{single well}})^N$ , where N=number of periods in the SLS. For the case of N=100 and  $\text{IQE}_{\text{single well}} = 92.2\%$ ,  $\text{IQE}_{\text{total}} = 45\%$ . Extending this estimation to a theoretical structure of equal P and In compositions as sample D, but with well/barrier thicknesses of 25Å/15Å,  $\text{IQE}_{\text{total}}(0.99957^{100})$  is 96%, which emphasizes the critical need for thin barriers. However, all carriers are not necessarily required to traverse all barriers, and any hole escape occurring via  $E_{V,2}$  and  $E_{V,3}$  should serve to improve IQE. Larsson, et al proposes that tunneling will only occur from energy levels where the tunneling lifetime is less than the scattering time which was measured to be only a few hundred fs in AlGaAs/GaAs structures.<sup>187</sup> For the proposed InGaAs/GaAsP SLS, this would only include  $E_{C,1}$  and  $E_{V,3}$ . Larsson argues that carriers can be promoted to these bands via interaction with longitudinal polar optical phonons. If this is valid, IQE would be reduced, but even thinner barriers (~10Å) could

greatly increase tunneling efficiency since tunneling lifetime from every bound energy level could be less than expected scattering times. In our analysis of escape lifetimes, only heavy holes were considered for lifetime calculations, but light holes may play an important role. Nelson, et al argue that light hole escape is the dominant type in the reported GaAs-AlGaAs p-i-n MQW diodes due to very fast escape times.<sup>142</sup> Experimental data is necessary to determine which of these mechanisms is dominant, and is the sort of future work that is necessary to advance and understand this device structure.

More information may be gained by calculating escape lifetimes for sample B:  $\text{In}_{0.28}\text{Ga}_{0.72}\text{As}/\text{GaAs}_{0.25}\text{P}_{0.75}$  SLS with 50 periods with 40Å wells and 30Å barriers for a total 0.35μm i-layer. A field of 30kV/cm is used for calculation. Values are summarized in Table 9.2 for samples B and D.

**Table 9.2** Calculated Thermionic Emission & Tunneling Lifetimes(Samples B&D[ps])

Sample ( $t_{\text{well}}/t_{\text{barrier}}$ )	$\tau_{\text{TH-EC},1}$	$\tau_{\text{TH-EV},1}$	$\tau_{\text{TH-EV},2}$	$\tau_{\text{TH-EV},3}$	$\tau_{\text{TN-EC},1}$	$\tau_{\text{TN-EV},1}$	$\tau_{\text{TH-EV},2}$	$\tau_{\text{TH-EV},3}$
D (38/23Å)	22	$5 \times 10^7$	$1 \times 10^5$	85	0.1	8	1.6	0.3
B (40/30Å)	12	$2 \times 10^7$	$4 \times 10^4$	33	0.2	34	5.5	0.6

By comparison of sample B to sample D, thermionic emission lifetime is decreased and tunneling lifetime is increased as expected from the thicker barriers and shallower wells of B. Calculating IQE for  $\tau_e = \tau_{\text{TN-EV},1} = 34\text{ps}$  yields  $\text{IQE} = 96.4\%$  if  $\tau_r = 1\text{ns}$ . This does not fully explain the large difference in  $I_{\text{SC}}$  observed in Figure 9.8. This could be partially due to the tunneling lifetimes being effectively longer for the SLS compared to the single QW used for estimation.  $\text{IQE}_{\text{total}}$  for the 50 periods of sample B ( $0.964^{50}$ ) may only be 15%

which is considerably less than 45% calculated for sample D. Extending this estimation to a theoretical structure of equal P and In compositions as sample D, but with well/barrier thicknesses of 25Å/15Å,  $IQE_{total}(0.99957^{100})$  is 96%, which emphasizes the critical need for thin barriers. However, the difference in  $I_{SC}$  is rather large and may be explained by additional factors. Consider the field induced band bending depicted in Figure 9.13 which has been exaggerated for demonstration purposes. Note that the change in barrier and well height is  $\sim 2-3\text{meV}$  which is approximately equal to the difference between two similar energy level in adjacent, such as  $E_{C,1}$  in two different adjoining wells. Since the shift is very small, resonant tunneling may occur. Resonant tunneling can drastically reduce the tunneling lifetime, even by orders of magnitude.<sup>188</sup> For sample B with wider barriers and wells, the relative shift of adjacent energy levels is greater for the same field. Since the field is higher in sample D, the shift is even more pronounced to produce  $\sim 7\text{meV}$  shift. Resonant tunneling is strongly sensitive to alignment of the energy levels and this may help explain the large difference in  $I_{SC}$  between B and D.

For ease of calculation, a square well band profile is assumed as in Figure 9.13 with band bending accounted for by equation 9.3. The square well approximation is good for developing a physical description of the system. Due to the diffuse interfaces of the SLS, the square well approximation is not completely correct. The actual band variation across the periodic structure is more likely trapezoidal or triangular with graded rather than sharp features. This is more difficult to model mathematically, but is relevant to consider qualitatively as it will impact carrier escape. In particular, tunneling lifetime is reduced exponentially with decreasing barrier thickness. As a final consideration, the thin barriers allow wavefunction interaction between wells such that mini-bands form rather than discrete

energy levels. At  $23\text{\AA}$ , the barriers are thin enough to consider this effect which may also impact carrier transport.

## 10 CONCLUSION

The degree of success for each goal stated at the beginning of Chapter 9 will now be summarized. Investigation of the growth of GaAsN alloys produced material with poor optical and electrical properties compared to more traditional alloys. These findings along with the vast amount data now published for GaAsN led to the conclusion that this material may be unsuitable for bulk film photovoltaic applications at the compositions required for lattice matching. A new approach is proposed to take advantage of lattice matching via a strained layer superlattice of InGaAs/GaAsP. Growth conditions for each layer are competitive, but strain balanced structures with up to 28% indium and 90% phosphorous are demonstrated. Extended absorption, relative to GaAs, is demonstrated up to 1150nm, corresponding to a bandgap of 1.1eV. The overall current produced from the SLS region of the device is low due to the relatively small volume of absorbing material. However, this can be improved with various light trapping techniques such as a distributed Bragg reflector<sup>20</sup> (DBR) and with further optimization of the device. Attempts to extend the absorption range further by adding N were not conclusive. A bandgap model is presented for comparison with experimental data. The model predicts a N composition of ~1.5% may be required to reach a bandgap of 1eV which is likely to severely degrade device performance. However, the model appears to consistently over estimate the quantum size effect. Compared to the measured bandgap of 1.1eV, achieved with InGaAs/GaAsP, it is an acceptable assumption that 1eV can be achieved with less than 1% N in InGaAsN/GaAsP. While these preliminary results for this structure do not add up to a well developed, 1 eV lattice matched junction, InGaAsN/GaAsPN shows promise for use in modern high efficiency solar cells.

Since InGaAsN remains the leading candidate for a 1eV junction a comparison to the initial solar cells made with this material should be made. In 1998, Hou, et al<sup>104</sup> reported performance values for typical InGaAsN based solar cells at the time. The values are summarized in Table 10.1 and compared to the best InGaAs/GaAsP based device developed in this work. Efficiency is comparable between the two devices. However, after many years of development by several research groups, the performance of InGaAsN material remains inadequate. With comparable effort focused on the InGaAs/GaAsP SLS approach, perhaps performance could be greatly increased.

**Table 10.1** Comparison of Early InGaAsN Solar Cell Compared to InGaAs/GaAsP Cell

Cell	V <sub>oc</sub> [ V ]	J <sub>sc</sub> [mA/cm <sup>2</sup> ]	FF	η
InGaAsN <sup>104</sup>	0.47	13.0	0.6*	3.67%
D	0.84	18.0	0.31	6.01%

\*Estimated from I-V plot

## REFERENCES

- 1 Judy Trinnaman, Alan Clarke, and World Energy Council., *Survey of energy resources, 2004*, 20th ed. (Elsevier, Amsterdam ; Oxford, 2004).
- 2 Richard W. Riley and United States. Dept. of Education., *Turning the corner : from a nation at risk to a nation with a future : second annual address*. (U.S. Dept. of Education, [Washington, D.C.?, 1995).
- 3 Richard C. Neville, *Solar energy conversion : the solar cell*, 2nd ed. (Elsevier, Amsterdam ; New York, 1995).
- 4 Charles E. Brown and International Geohydroscience and Energy Research Institute., *World energy resources*. (Springer, Berlin ; New York, 2002).
- 5 Gordon J. Aubrecht, *Energy : physical, environmental, and social impact*, 3rd ed. (Pearson/Prentice Hall, 2006).
- 6 A. Bartlett, *Renewable Resources Journal* **15** (4) (1998).
- 7 D. Pimentel, *Environment, Development, and Sustainability* **1** (19) (1999).
- 8 Bjørn Lomborg, *The skeptical environmentalist : measuring the real state of the world*. (Cambridge University Press, Cambridge ; New York, 2001).
- 9 Yoshihiro Hamakawa, *Thin-film solar cells : next generation photovoltaics and its applications*. (Springer, Berlin ; New York, 2004).
- 10 <http://www.solarbuzz.com/>.
- 11 United States. Office of Energy Markets and End Use., *Annual Energy Review 2004*. (Energy Dept. Energy Information Administration, Office of Energy Markets and End Use, Washington, D.C., 2005).
- 12 Paul Maycock, in *PV News* (February & May 2003).
- 13 J. Zhao, A. Wang, and M. Green, *Applied Physics Letters* **73** (14), 1991 (1998).
- 14 D. L. King, Sandia Photovoltaic Performance Model, Module Database (2001).
- 15 G. S. Kinsey, R. A. Sherif, R. R. King, C. M. Fetzer, H. L. Cotal, and N. H. Karam (Spectrolab, Inc.), presented at the Engineers for a Sustainable World, Austin, Texas, 2005.
- 16 D. J. Friedman, S. R. Kurtz, J. F. Geisz, in *The Conference Record of the 29th Photovoltaics Specialists Conference* (New Orleans, LA, 2002), pp. 856.

- 17 R. R. King, R. A. Sherif, C. M. Fetzer, D. C. Law, S. Kurtz, P. C. Colter, K. M. Edmondson, T. D. Isshiki, H. L. Cotal, H. Yoon, G. S. Kinsey, J. H. Ermer, T. Moriarty, J. Liehl, K. Emery, W. Metzger, R. K. Ahrenkiel, and N. H. Karam, presented at the Global Climate & Energy Project Solar Energy Workshop, Stanford University, 2004.
- 18 Ed. Paul Spencer, in *Re-Focus* (2005), pp. 35.
- 19 Jenny Nelson, *The physics of solar cells*. (Imperial College Press, London, 2003).
- 20 S. M. Sze, *Semiconductor devices, physics and technology*, 2nd ed. (Wiley, New York, 2002).
- 21 ASTM E490-00a, *Standard Solar Constant and Zero Air Mass Spectral Irradiance Tables*. (ASTM International, 2000).
- 22 ASTM G173-03, *Standard Tables for References Solar Spectral Irradiances: Direct Normal and Hemispherical on 37° Tilted Surface*. (ASTM International, 2003).
- 23 ASTM E927-05, *Standard Specification for Solar Simulation for Terrestrial Photovoltaic Testing*. (ASTM International, 2005).
- 24 Rolf E. Hummel, *Electronic properties of materials*, 3rd ed. (Springer, New York, 2001).
- 25 Richard H. Bube, *Photovoltaic materials*. (Imperial College Press, London, 1998).
- 26 Ben G. Streetman and Sanjay Banerjee, *Solid state electronic devices*, 6th ed. (Pearson Prentice Hall, Upper Saddle River, N.J., 2006).
- 27 Jasprit Singh, *Semiconductor devices : basic principles*. (Wiley, New York, 2000).
- 28 Auguste Bravais and Amos J. Shaler, *On the systems formed by points regularly distributed on a plane or in space*. (Crystallographic Society of America, [n.p.], 1949).
- 29 W. H. Miller, *A treatise on crystallography*. (For J. & J. J. Deighton; [etc., Cambridge, 1839).
- 30 B. D. Cullity and Stuart R. Stock, *Elements of x-ray diffraction*, 3rd ed. (Prentice Hall, Upper Saddle River, NJ, 2001).
- 31 A. Kelly, G. W. Groves, and P. Kidd, *Crystallography and crystal defects*, Rev. ed. (John Wiley & Sons, Chichester ; New York, 2000).
- 32 Ralph W. G. Wyckoff, *Crystal structures*, 2d ed. (Interscience Publishers, New York, 1963).
- 33 W. Pauli, *Zeitschrift für Physik* **31**, 765 (1925).

- 34 E. Schrödinger, *Annalen der Physik* **81**, 109 (1926).
- 35 F. Bloch, *Zeitschrift für Physik* **52**, 555 (1928).
- 36 Charles Kittel and C. Y. Fong, *Quantum theory of solids*, 2nd rev. print. ed. (Wiley, New York, 1987).
- 37 J. M. Ziman, *Principles of the theory of solids*, 2d ed. (University Press, Cambridge [Eng.], 1972).
- 38 J. R. Chelikowski, M. L. Cohen, *Physical Review B* **14** (2), 556 (1976).
- 39 J. Cerdá, F. Soria, *Physical Review B* **61** (12), 7965 (2000).
- 40 P. A. M. Dirac, *Proceedings of the Royal Society of London. Series A, Containing Papers of a Mathematical and Physical Character* **112** (762), 661 (1926).
- 41 E. Fermi, *Zeitschrift für Physik A* **36**, 902 (1926).
- 42 W. Bludau, A. Onton, and W. Heinke, *Journal of Applied Physics* **45**, 1846 (1974).
- 43 Sadao Adachi, *GaAs and related materials : bulk semiconducting and superlattice properties*. (World Scientific, Singapore ; River Edge, N.J., 1994).
- 44 M. B. Panish, and H. C. Casey, Jr., *Journal of Applied Physics* **40**, 163 (1969).
- 45 D. Xu, H. Yang, J. B. Li, D. G. Zhao, S. F. Li, S. M. Zhuang, and R. H. Wu, *Applied Physics Letters* **76**, 3025 (2000).
- 46 H. Fujimoto, K. Nakayama, M. Tanaka, and G. Misawa, *Japanese Journal of Applied Physics* **34**, 5056 (1995).
- 47 S. Kishino, *Advanced X-Ray Analysis* **16**, 367 (1973).
- 48 G. Giesecke, *Acta Crystallography* **11**, 369 (1958).
- 49 James H. Edgar and INSPEC (Information service), *Properties of group III nitrides*. (INSPEC, Institution of Electrical Engineers, London, 1994).
- 50 N. P. Belov, V. T. Prokopenko, and A.D. Yas'kov, *Soviet Physics - Semiconductors* **23**, 1296 (1989).
- 51 T. P. E. Broekaert, and C. G. Fonstad, *Journal of Applied Physics* **68**, 4310 (1990).
- 52 F. H. Pollak, C. W. Higginbotham, and M. Cardona, *Journal of the Physical Society of Japan* **21** (Supplement), 20 (1966).
- 53 C. Constantinescu, and S. Nan, *Physica Status Solidi A* **18**, 277 (1973).

- 54 G. Theodorou, and G. Tsegas, *Physical Review B* **61**, 10782 (2000).
- 55 A. T. Meney, E. P. O'Riley, and A.R. Adams, *Semiconductor Science and Technology* **11**, 897 (1996).
- 56 C. F. Schwerdtfeger, *Solid State Communications* **11**, 779 (1972).
- 57 Sadao Adachi, *Handbook of physical properties of semiconductors*. (Kluwer Academic Publishers, Boston, 2004).
- 58 Peter Theodore Landsberg, *Recombination in semiconductors*. (Cambridge University Press, Cambridge ; New York, 1991).
- 59 W. and H. Queisser Shockley, *Journal of Applied Physics* **32** (3), 510 (1960).
- 60 M. A. Green, K. Emery, D. L. King, S. Igari and W. Warta, *Progress in Photovoltaics: Research and Applications* **11**, 347 (2003).
- 61 E. D. Jackson, in *Transactions of the Conference on the Use of Solar Energy* (University of Arizona Press, Tucson, 1955), Vol. 5, pp. 122.
- 62 Martin A. Green, *Solar cells : operating principles, technology, and system applications*. (Prentice-Hall, Englewood Cliffs, NJ, 1982).
- 63 R. L. Moon, L. W. James, H. A. VanderPlas, T. O. Yep, G. A. Antypas, and Y. Chai, in *The Conference Record of the 13th Photovoltaic Specialists Conference* (1978), pp. 859.
- 64 L. C. Dinetta, M. H. Hannon, J. R. Cummings, J. B. McNeeley, A. M. Barnett, in *Proceedings of the 25th Intersociety Energy Conversion Engineering Conference* (Reno, NV, 1990), Vol. 1, pp. 587.
- 65 R. K. Jain, D. J. Flood, in *Proceedings of the 25th Intersociety Energy Conversion Engineering Conference* (1990), Vol. 1, pp. 581.
- 66 A. W. Bett, C. Baur, R. Beckert, F. Dimroth, G. Letay, M. Hein, M. Meusel, S. van Riesen, U. Schubert, G. Siefert, O. V. Sulime, T. N. D. Tibbets, presented at the 17th European Photovoltaic Specialists, Munich, 2001.
- 67 S. M. Bedair, M. F. Lamorte, and J. R. Hauser, *Applied Physics Letters* **34** (1), 38 (1978).
- 68 S. M. Bedair, B. P. Phatak, and J. R. Hauser, *IEEE Transactions on Electron Devices* **27** (4), 822 (1980).
- 69 L. M. Fraas, and R. C. Knechtli, in *The Conference Record of the 13th Photovoltaic Specialists Conference* (IEEE, Washington, DC, 1978), pp. 886.

- 70 S. M. Bedair, R. J. Markunas, M. L. Timmons, J. A. Hutchby, J. R. Hauser, US Patent No. H667 (September 5, 1987).
- 71 J. W. Matthews, A. E. Blakeslee, *Journal of Crystal Growth* **27**, 118 (1974).
- 72 J. H. van der Merwe, *Proceedings of the Phys. Society A* **63**, 616 (1950); J. H. van der Merwe, *Journal of Applied Physics* **34**, 117 (1963); J. H. van der Merwe, *Journal of Applied Physics* **34**, 123 (1963); J. H. van der Merwe, *Surface Science* **31**, 198 (1972).
- 73 E. Kasper, and H. J. Herzog, *Thin Solid Films* **44**, 357 (1977).
- 74 S. C. Jain, J. R. Willis, R. Bullough, *Advances in Physics* **39** (2), 127 (1990).
- 75 C. C. Grosjean, A. De Vos, *Journal of Physics D: Applied Physics* **14**, 883 (1981).
- 76 J. Olson, US Patent No. 4,667,059 (May 19, 1987).
- 77 J. Olson, S. Kurtz, US Patent No. 5,223,043 (June 29, 1993).
- 78 <http://www.spectrolab.com/>.
- 79 P. K. Chiang, J. H. Elmer, W. T. Nishikawa, D. D. Krut, D. E. Joslin, J. W. Eldredge, B. T. Cavicchi, J. M. Olsen, in *The Conference Record of the 25th IEEE Photovoltaic Specialists Conference* (1996), pp. 183.
- 80 J. Olson, S. Kurtz, D. Friedman, US Patent No. 6,281,426 (August 28, 2001).
- 81 <http://www.emcore.com/>.
- 82 M. Meusel, F. Dimroth, C. Baur, G. Siefert, A. W. Bett, K. Volz-Koch, W. Stolz, G. Strobl, C. Signorini, G. Hey, presented at the 19th European Photovoltaic Solar Energy Conference, Paris, 2004.
- 83 M. F. Lamorte, and D. Abbott, *Solid State Electronics* **22**, 467 (1978).
- 84 V. Y. Davydov, A. A. Klochikhin, R. P. Seisyan, V. V. Emtsev, S. V. Ivanov, F. Bechstedt, J. Furthmüller, H. Harima, A. V. Mudryi, J. Aderhold, O. Semchinova, and J. Graul, *Physica Status Solidi B* **229** (3), R1 (2001).
- 85 V. Y. Davydov, A. A. Klochikhin, V. V. Emtsev, S. V. Ivanov, V. V. Vekshin, F. Bechstedt, J. Furthmüller, H. Harima, A. V. Mudryi, A. Hashimoto, A. Yamamoto, J. Aderhold, J. Graul, and E. E. Haller, *Physica Status Solidi B* **230** (2), R4 (2002).
- 86 J. Wu, W. Walukiewicz, K. M. Yu, J. W. Arger III, E. E. Haller, H. Lu, W. J. Schaff, Y. Saito, and Y. Nanishi, *Applied Physics Letters* **80**, 3976 (2002).
- 87 J. S. Lee, H. S. Chung, K. Nahm, and C. K. Kim, *Physical Review B* **42** (2), 1452 (1990).

- 88 S. M. Bedair, J. A. Hutchby, J. P. C. Chiang, M. Simmons, and J. R. Hauser, in *Proceedings of the 15th IEEE Photovoltaic Specialists Conference* (New York, 1981), pp. 21.
- 89 J. Olson, S. R. Kurtz, A. E. Kibbler, and P. Faine, *Applied Physics Letters* **56** (7), 623 (1990).
- 90 M. Ohmori, T. Takamoto, E. Ikeda, H. Kurita, in *Technical Digest, International PVSEC-9* (Miyasaki, 1996), pp. 525.
- 91 Jeffrey A. Mazer, *Solar cells : an introduction to crystalline photovoltaic technology*. (Kluwer Academic Publishers, Boston, 1997).
- 92 E. B. Linder, J. P. Hanley, in *Conference Record of the 25th IEEE Photovoltaic Specialists Conference* (Washington, DC, 1996), pp. 1413.
- 93 B. R. Spence, and G. W. Marks, presented at the 13th Space Photovoltaic Research and Technology Conference, NASA Conf. Series 3278, 1994.
- 94 <http://www.nrel.gov/news/press/>.
- 95 H.L. Cotal, D. R. Lillington, J. H. Ermer, R. R. King, N. H. Karam, S. R. Kurtz, D. J. Friedman, J. M. Olson, J. S. Ward, A. Duda, K. A. Emery, T. Moriarty, in *Conference Record of the 28th IEEE Photovoltaic Specialists Conference* (2000), pp. 955.
- 96 S. R. Kurtz, D. Myers, J. M. Olson, in *Conference Record of the 26th IEEE Photovoltaic Specialists Conference* (Anaheim, CA, 1997), pp. 875.
- 97 M. Weyers, M. Sato, and H. Ando, *Japanese Journal of Applied Physics Part 2* **31** (7A), L853 (1992).
- 98 M. M. E. Fahmi, A. Khan, J. A. Griffin, G. L. Harris, L. H. Robins, A. G. Birdwell, Y. S. Kang, D. J. Smith, T. Steiner, S. N. Mohammad, *Journal of Applied Physics* **94** (12), 7576 (2003).
- 99 M. Kondow, K. Uomi, K. Hosomi, and T. Mozume, *Japanese Journal of Applied Physics Part 2* **33** (8A), L1056 (1994).
- 100 M. Kondow, K. Uomi, A. Niwa, T. Kitatani, S. Watahiki, Y. Yazawa, *Japanese Journal of Applied Physics Part 1* **35** (2B), 1273 (1996).
- 101 Mohamed Henini, *Dilute nitride semiconductors*, 1st ed. (Elsevier, San Diego, Calif., 2005).
- 102 J. F. Geisz, D. J. Friedman, J. M. Olson, S. R. Kurtz, B. M. Keyes, *Journal of Crystal Growth* **195**, 401 (1998).

- 103 D. J. Friedman, J. F. Geisz, S. R. Kurtz, J. M. Olson, *Journal of Crystal Growth* **195**, 409 (1998).
- 104 H. Q. Hou, K. C. Reinhardt, S. R. Kurtz, J. M. Gee, P. C. Chang, B. E. Hammons, in *2nd World Conference on Photovoltaic Energy Conversion* (1998), pp. 3600.
- 105 S. R. Kurtz, A. A. Allerman, E. D. Jones, J. M. Gee, J. J. Banas, and B. E. Hammons, *Applied Physics Letters* **74** (5), 729 (1999).
- 106 D. J. Friedman, J. F. Geisz, S. R. Kurtz, J. M. Olson, presented at the Second World Conference on Photovoltaic Energy Conversion, New York, 1998.
- 107 A. J. Ptak, S. Kurtz, S. W. Johnson, D. J. Friedman, J. F. Geisz, J. M. Olson, W. E. McMahon, A. E. Kibbler, C. Kramer, M. Young, S.H. Wei, S. B. Zhang, A. Janotti, P. Carrier, R. S. Crandall, B. M. Keyes, P. Dippo, A. G. Norman, W. K. Metzger, R. K. Ahrenkiel, R.C. Reedy, L Gedvilas, B. To, M. H. Weber, K. G. Lynn, in *NCPV and Solar Program Review Meeting 2003* (NREL, CD-520-33586, 2003), pp. 202.
- 108 S. W. Johnson, S. Kurtz, D. J. Friedman, A. J., Ptak, R. K. Ahrenliel, and R. S. Crandall, *Applied Physics Letters* **86**, 075109 (2005).
- 109 D. J. Friedman, A. J. Ptak, S. R. Kurtz, J. F. Geisz, and J. Kiehl, presented at the International Conference on Solar Concentrators for the Generation of Electricity or Hydrogen, Scottsdale, AZ, 2005.
- 110 S. Kurtz, R. R. King, K. M. Edmonson, D. J. Friedman, and N. H. Karam, in *Conference Record of the Twenty-Ninth IEEE Photovoltaic Specialists Conference* (New Orleans, 2002), pp. 1006.
- 111 J. J. M. Binsma, M. van Geemert, R. G. Broek, E. A. J. M. Bente, and M. K. Smit, presented at the IEEE/LEOS Annual Symposium, Brussel, 2001.
- 112 G. Ribordy, N. Gisin, O. Guinard, D. Stucki, M. Wegmuller, H. Zbinden, *Journal of Modern Optics* **51**, 1381 (2004).
- 113 R. N. Nottenburg, Y. K. Chen, M. B. Panish, D. A. Humphrey, R. Hamm, *Electron Device Letters* **10** (1), 30 (1989).
- 114 K. W. Kobayashi, A. K. Oki, L. T. Tran, J. C. Cowles, A. Gutierrez-Aitken, F. Yamada, T. R. Block, D. C. Street, *IEEE Journal of Solid-State Circuits* **34** (9), 1225 (1999).
- 115 J. W. Matthews, A. E. Blakeslee, *Journal of Crystal Growth* **29**, 273 (1975).
- 116 A. P. Roth, M. Sacilotti, R. A. Masut, P. J. D'Arch, B. Watt, G. I. Sproule, and D. F. Mitchell, *Applied Physics Letters* **48**, 1452 (1986).

- 117 L. Esaki, R. Tsu, (IBM Research Center, Internal Research Report No. RC2418, 1969).
- 118 Paul N. Butcher, Norman H. March, and M. P. Tosi, *Physics of low-dimensional semiconductor structures*. (Plenum Press, New York, 1993).
- 119 G. C. Osbourn, *Journal of Applied Physics* **63** (3), 1586 (1982).
- 120 W. D. Laidig, J. W. Lee, P. K. Chiang, L. W. Simpson, and S. M. Bedair, *Journal of Applied Physics* **54**, 6382 (1983).
- 121 G. C. Osbourn, *Journal of Vacuum Science and Technology B* **2** (2), 176 (1984).
- 122 S. M. Bedair, T. Katsuyama, M. Timmons, and M. A. Tischler, *IEEE Electron Device Letters* **EDL-5** (2), 45 (1984).
- 123 T. M. A. Tischler Katsuyama, D. Moore, N. Hamaguchi, N. A. El-Masry. and S. M. Bedair, *Solar Cells* **21**, 413 (1987).
- 124 K. W. J. Barnham, D. B. Bushnell, J. P. Connolly, N. Ekins-Daukes, B. G. Klufftinger, M. Mazzer, J. Nelson, presented at the International School on Crystal Growth of Materials for Energy Production and Energy-Saving Applications, "Abdus Salam" International Centre for Theoretical Physics, Trieste, Italy, 2001.
- 125 F. H. Pollak, M. Cardona, *Physical Review* **172** (3), 816 (1968).
- 126 A. Blacha, H. Presting, M. Cardona, *Physica Status Solidi B* **126** (1), 11 (1984).
- 127 G. H. Olsen, C. J. Neuse, and R. T. Smith, *Journal of Applied Physics* **49** (11), 5523 (1978).
- 128 N. G. Anderson, W. D. Laidig, G. Lee, Y. Lo, and M. O. Ozturk, in *Proceedings of the Materials Research Society Symposium* (1985), Vol. 37, pp. 223.
- 129 Gennadiï Levikovich Bir and Grigoriï Ezekievich Pikus, *Symmetry and strain-induced effects in semiconductors*. (Wiley, New York., 1974).
- 130 H. Asai, and K. Oe, *Journal of Applied Physics* **54** (4), 2052 (1983).
- 131 Y. P. Varshni, *Physica (Utrecht)* **34**, 194 (1967).
- 132 J-Y Marzin, M. N. Charasse, and B. Sermage, *Physical Review B* **31**, 8298 (1985).
- 133 H. C. Casey, and M. B. Panish, *Heterostructure Lasers, Part B: Materials and Operating Characteristics*. (Academic, New York, 1978).
- 134 N. M. Froberg, A. M. Johnson, K. W. Goosen, J. E. Cunningham, M. B. Santos, W. Y. Jan, T. H. Wood, and C. A. Burns, *Applied Physics Letters* **64** (13), 1705 (1994).

- 135 R. de L. Kronig, and W. G. Penney, Proceedings of the Royal Society of London. Series A, Containing Papers of a Mathematical and Physical Character **130** (814), 499 (1931).
- 136 Gerald Bastard, *Wave mechanics applied to semiconductor heterostructures*. (Les Editions de Physique, Halsted Press, Les Ulis Cedex, France, New York, N.Y., 1988).
- 137 F. Szmulowicz, European Journal of Physics **18**, 392 (1997).
- 138 L. J. Sham, M. Nakayama, Physical Review B **20** (2), 734 (1979).
- 139 S. Sakai, and T. Abe, in *57th Fall Meeting of the Japanese Society of Applied Physics* (Fukuoka, Japan, 1994), pp. 951.
- 140 M. Kondow, T. Kitatani, S. Shin'ichi, M. Larson, K. Nakahara, Y. Yazawa, M. Okai, K. Uomi, IEEE Journal of Selected Topics in Quantum Electronics **3** (3), 719 (1997).
- 141 A. M. Fox, D. A. B. Miller, G. Livescu, J. E. Cunningham, W. Y. Jan, IEEE Journal of Quantum Electronics **27** (10), 2281 (1991).
- 142 J. Nelson, M. Paxman, K. W. J. Barnham, J. S. Roberts, and C. Button, IEEE Journal of Quantum Electronics **29** (6), 1460 (1993).
- 143 W. Kossel, Nachrichten von der Königl. Gesellschaft der Wissenschaften zu Göttingen, 135 (1927).
- 144 I. N. Stranski, Zeitschrift für Physikalische Chemie **136**, 259 (1928).
- 145 G. B. Stringfellow, *Organometallic vapor-phase epitaxy : theory and practice*, 2nd ed. (Academic Press, San Diego, 1999).
- 146 <http://www.thomas-swan.co.uk/>.
- 147 <http://www.eurotherm.com/>.
- 148 <http://www.mksinst.com/>.
- 149 <http://www.wafertech.co.uk/>.
- 150 C. A. Larson, Ph.D. dissertation, University of Utah, 1988.
- 151 C. A. Larson, N. I. Buchan, and G. B. Stringfellow, Journal of Crystal Growth **85**, 148 (1987).
- 152 B. F. Moody, P. T. Barletta, N. A. El-Masry, J. C. Roberts, M. E. Aumer, S. F. LeBoeuf, and S. M. Bedair, Applied Physics Letters **80** (14), 2475 (2002).

- 153 C. H. Chen, C. A. Larson, and G. B. Stringfellow, *Applied Physics Letters* **50** (4), 218 (1986).
- 154 W. Stolz, *Journal of Crystal Growth* **209**, 272 (2000).
- 155 S. Liu, and D. A. Stevenson, *Journal of the Electrochemical Society* **125**, 1161 (1978).
- 156 A. Ougazzadea, Y. LeBellego, E. V. K. Rao, M. Juhel, L. Leprince, and G. Patriarche, *Applied Physics Letters* **68**, 3617 (1997).
- 157 A. Ougazzadea, E. V. K. Rao, B. Sermage, L. Leprince, and M. Gauneau, *Japanese Journal of Applied Physics* **38**, 1019 (1999).
- 158 S. Okumura, S. Yoshida, S. Misawa, and E. Sakuma, *Surface Science* **267**, 50 (1992).
- 159 T. F. Kuech, B. S. Meyerson, and E. Veuhoff, *Applied Physics Letters* **44** (10), 986 (1984).
- 160 W. R. Runyan and T. J. Shaffner, *Semiconductor measurements and instrumentation*, 2nd ed. (McGraw-Hill, New York, 1998).
- 161 O. Yastrubchak, T. Wosinski, J. Z. Domagala, E. Lusakowska, T. Figielski, B. Pecz, and A. L. Toth, *Journal of Physics: Condensed Matter* **16**, S1 (2004).
- 162 M. S. Abrahams, and C. J. Buiocchi, *Journal of Applied Physics* **36** (9), 2855 (1965).
- 163 F1404-92, *Test Method for Crystallographic Perfection of Gallium Arsenide by Molten Potassium Hydroxide (KOH) Etch Technique*. (ASTM International, 1992).
- 164 A. Segmuller, and A. E. Blakeslee, *Journal of Applied Crystallography* **6**, 19 (1973).
- 165 L. J. van der Pauw, *Philips Research Reports* **13**, 1 (1958).
- 166 Stanley L. Flegler, John William Heckman, and Karen L. Klomparens, *Scanning and transmission electron microscopy : an introduction*. (Oxford University Press, New York, 1995).
- 167 Ludwig Reimer, *Transmission electron microscopy : physics of image formation and microanalysis*, 4th ed. (Springer, Berlin ; New York, 1997).
- 168 S. Horiuchi, *Fundamentals of high-resolution transmission electron microscopy*. (North-Holland, Amsterdam ; New York, 1994).
- 169 Ralph Williams, *Modern GaAs processing methods*. (Artech House, Boston, 1990).
- 170 J. Toivonen, T. Hakkarainen, M. Sopahen, and H. Lipsanen, *Journal of Crystal Growth* **221**, 456 (2000).

- 171 E. L. Piner, F.G. McIntosh, J. C. Roberts, M. K. Behbehani, K. S. Boutros, N. A. El-Masry, and S. M. Bedair, *Applied Physics Letters* **70**, 461 (1997).
- 172 M. Kondow, T. Kitatani, S. Shirakata, *Journal of Physics: Condensed Matter* **16**, S3229 (2004).
- 173 A. Polimeni, G. Baldassarri Hoyer von Hoyersthal, M. Bissiri, M. Capizzi, A. Frova, M. Fischer, M. Reinhardt, and A. Forchel, *Semiconductor Science and Technology* **17**, 797 (2002).
- 174 I. A. Buyanova, W. M. Chen, C. W. Tu, *Journal of Physics: Condensed Matter* **16**, S3027 (2004).
- 175 J. F. Geisz, D. J. Friedman, *Semiconductor Science and Technology* **17**, 769 (2002).
- 176 C. Giannini, T. Baumbach, D. Lubbert, R. Felici, L. Tapfer, T. Marschner, W. Stolz, N. Y. Jin-Phillipp, and F. Phillipp, *Physical Review B* **61** (3), 2173 (2000).
- 177 F. Liu, J. Tersoff, and M. G. Lagally, *Physical Review Letters* **80** (6), 1268 (1998).
- 178 R. N. Hall, *Physical Review* **87** (2), 387 (1952).
- 179 W. and W. T. Read Shockley, Jr., *Physical Review* **87** (5), 835 (1952).
- 180 F. W. Ragay, E. W. M. Ruigrok, and J. H. Wolter, in *Proceedings of the 1st World Conference and Exhibition on Photovoltaic Solar Energy Conversion* (IEEE, 1994), pp. 1934.
- 181 J. P. Connolly, J. Nelson, K. W. J., Barnham, I. Ballard, C. Roberts, J. S. Roberts, C. T. Foxon, in *The Conference Record of the 28th IEEE Photovoltaic Specialists Conference* (Anchorage, AK, 2000), pp. 1234.
- 182 N. J. Ekins-Daukes, D. B. Bushnell, K. W. J. Barnham, J. P. Connolly, J. Nelson, M. Mazzer, J. S. Roberts, G. Hill, and R. Airey, in *Proceedings of the 17th European Photovoltaic Solar Energy Conference* (Munich, Germany, 2001), pp. 196.
- 183 S. M. Bedair, J. C. Roberts, D. Jung, B. F. Moody, N. A. El-Masry, T. Katsuyama, in *Conference Record of the 28th IEEE Photovoltaic Specialists Conference* (Anchorage, AK, 2000), pp. 1154.
- 184 T. Matsusue, and H. Sakaki, *Applied Physics Letters* **50**, 1429 (1987).
- 185 H. Schneider, and K. von Klitzing, *Physical Review B* **38** (9), 6160 (1988).
- 186 B. Deveaud, J. Shah, T. C. Damen, and W. T. Tsang, *Applied Physics Letters* **52**, 1886 (1988).
- 187 A. Larsson, P. Andrekson, S. T. Eng, A. Yariv, *IEEE Journal of Quantum Electronics* **24** (5), 787 (1988).

- 188 H. Schneider, K. von Klitzing, and K. Ploog, *Superlattices and Microstructures* **5**, 383 (1989).
- 189 Ralph Raymond Hultgren and American Society for Metals., *Selected values of the thermodynamic properties of the elements*. (American Society for Metals, Metals Park, Ohio., 1973).
- 190 W. Kischio, *Zeitschrift fuer Anorganische und Allgemeine Chemie* **328**, 187 (1964).
- 191 M. Tmar, A. Gabriel, C. Chatillon, and I. Ansara, *Journal of Crystal Growth* **68**, 557 (1984).
- 192 M. R. Brozel, G. E. Stillman, and INSPEC (Information service), *Properties of gallium arsenide*, 3rd ed. (INSPEC, London, 1996).
- 193 K. Yamaguchi, K. Itagaki, and A. Yazawa, *Journal of the Japan Institute of Metals* **53**, 764 (1989).
- 194 R. A. Logan, and A. J. Peters, *Journal of Applied Physics* **31**, 122 (1960).
- 195 A. G. Sigai, M. S. Abrahams, and J. Blanc, *Journal of the Electrochemical Society* **119**, 952 (1972).
- 196 M. G. Craford, W. O. Groves, A. H. Herzog, and D. E. Hill, *Journal of Applied Physics* **42**, 2751 (1971).
- 197 Lin Lan-Ying, Lin Yao-Wang, Zhong Zing-Ru, Zhang Yan-Yun, and Li Hsui-Lan, *Journal of Crystal Growth* **56**, 344 (1982).
- 198 T. C. Harman, H. L. Goering, and A. C. Beer, *Physical Review* **104**, 1562 (1956).
- 199 J. G. Kim, A. C. Frenkel, H. Liu, and R. M. Park, *Applied Physics Letters* **65**, 91 (1994).
- 200 G. Ottaviani, L. Reggiani, C. Canali, F. Nava, and A. Alberigi-Quaranta, *Physical Review B* **12**, 3318 (1975).
- 201 D. C. Look, D. K. Lorance, J. R. Sizelove, C. E. Stutz, K. R. Evans, and D. W. Whitson, *Journal of Applied Physics* **71**, 260 (1992).
- 202 D. P. Bortfeld, B. J. Curtis, and H. Meier, *Journal of Applied Physics* **43**, 1293 (1972).
- 203 M. H. Kim, S. S. Bose, B. J. Skromme, B. Lee, and G. E. Stillman, *Journal of Electronic Materials* **20**, 671 (1991).
- 204 M. E. Levinshhteain, S. L. Rumyantsev, and Michael Shur, *Handbook series on semiconductor parameters*. (World Scientific, Singapore ; New Jersey, 1996).

- 205 Fernando A. Ponce, *III-V nitrides : symposium held December 2-6, 1996, Boston, Massachusetts, U.S.A.* (Materials Research Society, Pittsburgh, Pa., 1997).
- 206 Robert Hull and INSPEC (Information service), *Properties of crystalline silicon.* (INSPEC, the Institution of Electrical Engineers, London, 1999).
- 207 M. Leszczynski, *Crystal Research and Technology* **25**, 721 (1990).
- 208 K. Haruna, H. Maeta, K. Ohashi, and T. Koike, *Journal of Physics C: Solid State Physics* **19**, 5149 (1986).
- 209 INSPEC (Information service) and Institution of Electrical Engineers., *Properties of gallium arsenide*, 2nd ed. (INSPEC, London ; New York, 1990).
- 210 A. N. N. Sirota, A. M. Antyukhov, and A. A. Sidorov, *Soviet Physics - Doklady* **29**, 662 (1984).
- 211 J. J. Hall, *Physical Review* **161**, 756 (1967).
- 212 H. Gehrsitz, H. Sigg, N. Herres, K. Bachem, K. Köhler, and F. K. Reinhart, *Physical Review B* **60**, 11601 (1999).
- 213 R. and W. O. Groves Weil, *Journal of Applied Physics* **39**, 4049 (1968).
- 214 S. Adachi, *Journal of Applied Physics* **58**, R1 (1985).
- 215 D. Gerlich, *Journal of Applied Physics* **34**, 2915 (1963).
- 216 K. Kim, W. R. L. Lambrecht, and B. Segall, *Physical Review B* **53**, 16310 (1996).
- 217 M. van Schifgaard, A. Sher, and A. B. Chen, *Journal of Crystal Growth* **178**, 8 (1997).
- 218 A. R. Goni, K. Syassen, K. Strossner, and M. Cardona, *Semiconductor Science and Technology* **4**, 246 (1989).
- 219 P. Kraisingdecha, and M. Gal, *Applied Physics Letters* **69**, 1355 (1996).
- 220 M. A. Marciniak, R. L. Hengehold, and Y. K. Yeo, *Journal of Applied Physics* **84**, 480 (1998).
- 221 G. Ramirez-Flores, et. al., *Physical Review B* **52**, 8082 (1995).
- 222 M. Mishima, M. Miura, S. Ozaki, and S. Adachi, *Journal of Applied Physics* **91**, 4904 (2002).
- 223 P. Lautenschlager, M. Garriga, S. Logothetidis, and M. Cordona, *Physical Review B* **35**, 9174 (1987).

<sup>224</sup> C. H. Liu, K. E. Singer, J. H. Evans-Freeman, K. Heath, and M. Missous, *Semiconductor Science and Technology* **12**, 1619 (1997).

## APPENDIX

## APPENDIX A

Table of Semiconductor Values Used for Various Calculations at Around 300K (After Adachi<sup>57</sup> unless otherwise noted)

	Si	AlAs	GaP	GaAs	InAs	c-GaN
Bandgap (eV)	1.1242 <sup>42</sup>	2.168 <sup>43</sup>	2.261 <sup>44</sup>	1.430 <sup>43</sup>	0.361	3.216 <sup>45</sup>
Transition	Indirect	Indirect	Indirect	Direct	Direct	Direct
Lattice	DC	ZB	ZB	ZB	ZB	ZB
Lattice Constant(Å)	5.431 <sup>46</sup>	5.661 <sup>43</sup>	5.451 <sup>47</sup>	5.6533 <sup>43</sup>	6.0584 <sup>48</sup>	4.52 <sup>49</sup>
Density(g/cm <sup>3</sup> )	2.3291	3.7302	4.1299	5.3175 <sup>43</sup>	5.6678	6.02
Melting Point (K)	1687 <sup>189</sup>	1740 <sup>190</sup>	1730 <sup>191</sup>	1513 <sup>192</sup>	1221 <sup>193</sup>	-
Electron Mobility(cm <sup>2</sup> /V s)	1750 <sup>194</sup>	294 <sup>195</sup>	189 <sup>196</sup>	9340 <sup>197</sup>	30000 <sup>198</sup>	760 <sup>199</sup>
Hole Mobility (cm <sup>2</sup> /V s)	450 <sup>200</sup>	105 <sup>201</sup>	140 <sup>202</sup>	450 <sup>203</sup>	450 <sup>204</sup>	350 <sup>205</sup>
Electron Effective Mass, $\Gamma$	0.188 <sup>50</sup>	0.059 <sup>51</sup>	0.135 <sup>52</sup>	0.064 <sup>53</sup>	0.025 <sup>54</sup>	0.15 <sup>55</sup>
Hole Effective Mass, $\Gamma$						
Heavy Holes	0.439	0.75 <sup>43</sup>	0.67 <sup>56</sup>	0.55 <sup>43</sup>	0.36	1.19
Light Holes	0.159	0.16 <sup>43</sup>	0.17 <sup>56</sup>	0.083 <sup>43</sup>	0.026	0.20
Thermal Expansion Coefficient(10 <sup>-6</sup> K <sup>-1</sup> )	2.616 <sup>206</sup>	4.1 <sup>207</sup>	4.89 <sup>208</sup>	6.03 <sup>209</sup>	4.95 <sup>210</sup>	-
Elastic Constants (10 <sup>11</sup> dyn/cm <sup>2</sup> )						
C <sub>11</sub>	16.564 <sup>211</sup>	11.93 <sup>212</sup>	14.12 <sup>213</sup>	11.88 <sup>214</sup>	8.329 <sup>215</sup>	29.6 <sup>216,217</sup>
C <sub>12</sub>	6.394 <sup>211</sup>	5.72 <sup>212</sup>	6.253 <sup>213</sup>	5.38 <sup>214</sup>	4.526 <sup>215</sup>	15.4 <sup>216,217</sup>
C <sub>44</sub>	7.951 <sup>211</sup>	5.72 <sup>212</sup>	7.047 <sup>213</sup>	5.94 <sup>214</sup>	3.959 <sup>215</sup>	20.6 <sup>216,217</sup>
Shear Deformation Potential, b ( eV )			-1.3 <sup>130</sup>	-1.7 <sup>218</sup>	-1.8 <sup>215</sup>	-1.9 <sup>216</sup>
Hydrostatic Pressure Coefficient, $\partial E_0/\partial P$ (10 <sup>-12</sup> eV/dyn cm <sup>-2</sup> )			10.7 <sup>130</sup>	10.8 <sup>218</sup>	9.6 <sup>215</sup>	3.0 <sup>216</sup>
Young's Modulus(100)						
[001](10 <sup>11</sup> dyn/cm <sup>2</sup> )	13.00	08.22	10.3	8.53 <sup>43</sup>	5.14	1.91
[011] (10 <sup>11</sup> dyn/cm <sup>2</sup> )	16.90	11.79	14.4	12.13 <sup>43</sup>	7.93	3.01

	Si	AlAs	GaP	GaAs	InAs	c-GaN
Poisson's Ratio (100)						
[010], [001]	0.279	0.324	0.306	0.312 <sup>43</sup>	0.352	0.337
[011], [0 $\bar{1}$ 1]	0.062	0.031	0.025	0.021 <sup>43</sup>	0.222	-0.046
Varshni Fitting Parameter, $\alpha$ ( $10^{-4}$ eV/K) for $E_g(T)$			5.8(X)/ 6.2( $\Gamma$ )	5.5 <sup>219</sup>	3.8 <sup>220</sup>	6.7 <sup>221</sup>
Varshni Fitting Parameter, $\beta$ (K) for $E_g(T)$			387(X)/ 190( $\Gamma$ )	255 <sup>219</sup>	215 <sup>220</sup>	600 <sup>221</sup>
Bandgap at 0K, $E_g(0)$ (eV)			2.32(X)/ 2.86( $\Gamma$ )	1.515 <sup>219</sup>	0.414 <sup>220</sup>	3.302 <sup>221</sup>
Varshni Fitting Parameter, $\alpha$ ( $10^{-4}$ eV/K) for $E_0(T)+\Delta_0(T)$			7.00 <sup>222</sup>	3.50 <sup>223</sup>	3.07 <sup>224</sup>	
Varshni Fitting Parameter, $\beta$ (K) for $E_0(T)+\Delta_0(T)$			250 <sup>222</sup>	225 <sup>223</sup>	191 <sup>224</sup>	

## APPENDIX B

Detailed specifications for 2" GaAs substrates from Wafer Technology Ltd.

All wafers are produced with the vertical gradient freeze method (VGF) which results in lower dislocation density than any other method.

### Electronic Specifications

Dopant	Type	Resistivity [ $\Omega$ ]	Carrier Concentration [ $\text{cm}^{-3}$ ]	Mobility [ $\text{cm}^2\text{V}^{-1}\text{s}^{-1}$ ]	Etch Pit Density [ $\text{cm}^{-2}$ ]
Silicon	n	Not Specified	$(1-5) \times 10^{18}$	Not specified	<100
Undoped	Semi- Insulating	$>10^{17}$	Not Specified	>5000	<2000
Zinc	p	Not Specified	$5 \times 10^{18}$ – $5 \times 10^{19}$	Not Specified	<300

### General Mechanical Specifications

Parameter	Standard Value
Orientation	(001) $\pm 0.1^\circ$
Diameter	$50.5 \pm 0.5\text{mm}$
Flats	EJ
Major flat length	$16 \pm 2\text{mm}$
Minor flat length	$8 \pm 1\text{mm}$
Thickness	$500\mu\text{m} \pm 25\mu\text{m}$
Lasermark	Back surface, parallel to major flat